

# Enhanced absorption in thin and ultrathin silicon films by 3D photonic band gap back reflectors

Devashish Sharma,<sup>1,2,3</sup> Shakeeb Bin Hasan,<sup>1,3</sup> Rebecca Saive,<sup>4</sup> Jaap J. W. van der Vegt,<sup>2</sup> and Willem L. Vos<sup>1,\*</sup>

<sup>1</sup>*Complex Photonic Systems (COPS), MESA+ Institute for Nanotechnology, University of Twente, P.O. Box 217, 7500 AE Enschede, The Netherlands*

<sup>2</sup>*Mathematics of Computational Science (MACS), MESA+ Institute for Nanotechnology, University of Twente, P.O. Box 217, 7500 AE, Enschede, The Netherlands*

<sup>3</sup>*Present address: ASML Netherlands B.V., 5504 DR Veldhoven, The Netherlands*

<sup>4</sup>*Inorganic Materials Science (IMS), MESA+ Institute for Nanotechnology, University of Twente, P.O. Box 217, 7500 AE, Enschede, The Netherlands*

Since thin and ultrathin silicon films have limited optical absorption, we explore the effect of a nanostructured back reflector to recycle the unabsorbed light. As a back reflector, we investigate a three-dimensional (3D) photonic band gap crystal made from silicon that is readily integrated with the thin silicon films. We numerically obtain the optical properties by solving the 3D time-harmonic Maxwell equations using the finite-element method, and model silicon with experimentally determined optical constants. The absorption enhancement spectra and the photonic band gap generated current density are obtained by weighting the absorption spectra with the AM 1.5 standard solar spectrum. We study thin films in two different regimes, much thicker ( $L_{Si} = 2400$  nm) or much thinner ( $L_{Si} = 80$  nm) than the wavelength of light. At  $L_{Si} = 2400$  nm thin film, the 3D photonic band gap crystal enhances the spectrally averaged ( $\lambda = 680$  nm to 880 nm) silicon absorption by  $2.22\times$  ( $s$ -pol.) to  $2.45\times$  ( $p$ -pol.), which exceeds the enhancement of a perfect metal back reflector (1.47 to  $1.56\times$ ). The absorption is considerably enhanced by the (i) broadband angle and polarization-independent reflectivity in the 3D photonic band gap, and (ii) the excitation of many guided modes in the film by the crystal's surface diffraction leading to greatly enhanced path lengths. At  $L_{Si} = 80$  nm ultrathin film, the photonic crystal back reflector yields a striking average absorption enhancement of  $9.15\times$ , much more than  $0.83\times$  for a perfect metal. This enhancement is due to a remarkable guided mode that is confined within the *combined* thickness of the ultrathin film and the photonic crystal's Bragg attenuation length. An important feature of the 3D photonic band gap is to have a broad bandwidth, which leads to the back reflector's Bragg attenuation length being much shorter than the silicon absorption length. Consequently, light is confined inside the thin film and the remarkable absorption enhancements are not due to the additional thickness of the photonic crystal back reflector. We briefly discuss a number of high-tech devices that could profit from our results, including thin film solar cells.

arXiv:2106.15851v2 [physics.optics] 29 Oct 2021

---

\* w.l.vos@utwente.nl, URL: [www.photonicbandgaps.com](http://www.photonicbandgaps.com)

## I. INTRODUCTION

Being a highly abundant and non-toxic material available in the earth's crust, silicon is an ideal choice to fabricate many high-tech devices with vast societal impact that employ the absorption of incident light. These devices include compact on-chip sensors, diodes and avalanche photodiodes, and charge-coupled devices (CCD) for cameras [1–6]. Moreover, to address the ongoing worldwide climate crisis [7], and provide solar energy for the entire world's population [8, 9], there is a pressing need to harvest the sun's energy with sustainable solar cells. All devices above employ the photovoltaic effect to absorb light and convert the absorbed energy into electricity using semiconductor materials [10, 11]. While thick silicon devices are widely used, thin silicon films are enjoying a rising popularity on account of their obvious sustainability [12], since they require less material and hence less resources and costs [13]. Moreover, they are mechanically flexible so they can be deployed on many different platforms, including freely shaped ones.

Since crystalline silicon (c-Si) has an indirect band gap at 1.1 eV, the absorption of light is low in the near infrared range that notably contains 36% of all solar photons [14]. Conversely, the absorption length is long, namely  $l_a = 1$  mm just above the gap at  $\lambda = 1100$  nm (1.12 eV) and still only  $l_a = 10$   $\mu\text{m}$  at  $\lambda = 800$  nm (1.55 eV) [15]. Since the thickness of thin silicon film devices and solar cells is much less than the absorption lengths, the absorption of incident (solar) light is low [16–19], which adversely affects the cost and the flexibility advantages [20–23].

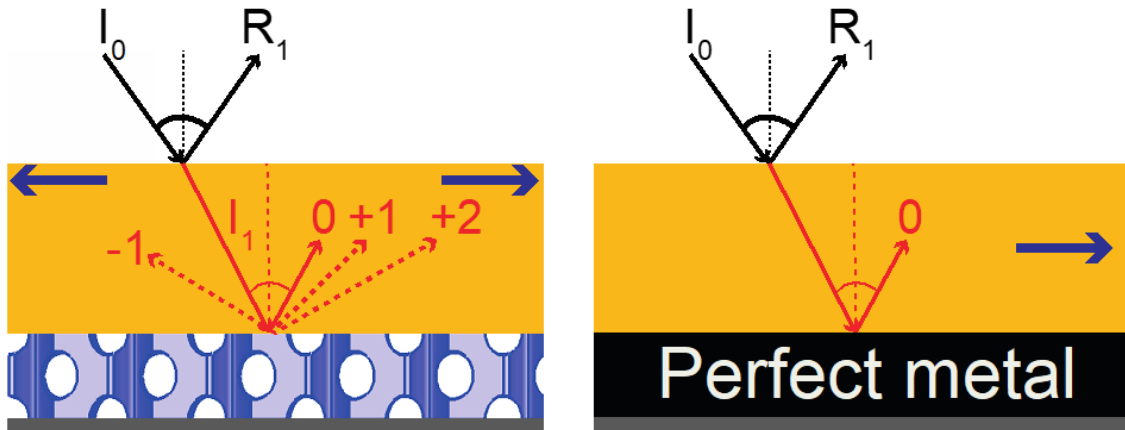


FIG. 1: Design of a thin silicon film (orange) with a 3D photonic band gap crystal (purple, left) and a perfect metal (black, right) as back reflectors. Here, 0 indicates the 0<sup>th</sup> diffraction order that corresponds to specular reflected light by the photonic crystal or the perfect metal.  $I_0$  and  $R_1$  represent the light incident and the first reflection at the front surface of the thin film, respectively.  $I_1$  represents the light refracted into the thin film medium and incident on the photonic crystal.  $-1$ ,  $1$ , and  $2$  are nonzero diffraction orders. Blue arrows represent the propagation of guided modes in the thin silicon film. For potential application in light-absorbing high-tech devices (including photovoltaics), thin metallic rear contacts (grey) are sketched, but are not considered in our nanophotonic simulations.

Efficient light trapping enhances the absorption efficiency of silicon films while sustaining their advantages [16, 23–25]. In traditional light trapping approaches as in solar cells, one increases the light paths using random texturing [26, 27] to scatter incident light into long oblique light paths and uses a back reflector to reflect unabsorbed light back into the thin film. In practice, perfect scattering is impossible to achieve, which limits the attainable efficiency [28]. An ideal back reflector reflects light incident from any angle, also referred to as omnidirectional reflectivity [29], and ideally for all wavelengths and all polarizations of light. As illustrated in Fig. 1(right), a perfect metal with 100% reflectivity at all wavelengths and all polarizations would thus seem to be an ideal back reflector. In practice, no metal has 100% reflectivity at all wavelengths due to Ohmic losses [30]. Moreover, light that is not reflected by a real metal gets absorbed, which produces heat and further limits the absorption efficiency of a thin film device.

Notably, much work has been devoted to light trapping strategies based on wave optics [31–35]. These strategies outperform random scattering optics approaches, typically over broad wavelength ranges, where one takes advantage of enhancements caused by constructive interference. To manipulate the interference, specially designed nano-structures are pursued, including 1D (“Bragg stack”), 2D, and 3D photonic crystals [36–48].

In this paper, we focus on photonic crystal back reflectors with a *complete 3D photonic band gap* [49, 50], a frequency range for which the propagation of light is rigorously forbidden for all incident angles and all polarizations

simultaneously, as recently demonstrated in experiments and calculations [51–58]. To illustrate this concept, Fig. 1 shows a schematic design of a thin silicon film (orange) with a 3D photonic band gap crystal back reflector (purple). Incident light with intensity  $I_0$  is Fresnel diffracted to intensity  $I_1$  within the thin film. When the incident light  $I_1$  has a frequency in the photonic band gap, it is reflected by the photonic crystal [49] back into the film. The specular reflected beam corresponds to the 0<sup>th</sup> diffraction order. Figure 1 illustrates non-zeroth order diffraction modes, *e.g.*,  $-1$ ,  $1$ , and  $2$ , that are generated at the periodic interface between the thin film and the photonic crystal. These diffraction modes couple light into guided modes that are confined inside the thin silicon film via total internal reflection. Consequently, guided photons obtain a long path length inside the thin film and have thus an enhanced probability for absorption. Hence, different from a perfect metal, a 3D photonic crystal enhances the absorption of a thin silicon film by (i) profiting from perfect reflectivity inside the band gap for all incident angles and polarizations, and (ii) by generating guided modes [42, 45].

Recently, we reported a numerical study on the enhanced energy density and optical absorption for realistic and finite 3D silicon photonic band gap crystals with an embedded resonant cavity [59, 60]. The absorption was found to be substantially enhanced, but only within the tiny cavity volume, as opposed to the present case where the absorption occurs throughout the whole film volume, which avoids local heating and non-linear or many-body effects that adversely affect the absorption efficiency [11]. While a structure with a 3D photonic band gap is from the outset relevant as an omnidirectional, broadband, and polarization-robust back reflector for ultrathin silicon films (including solar cells), they have been hardly studied before. Therefore, we investigate nanostructured back reflectors with a 3D photonic band gap that is tailored to have a broad photonic band gap in the visible regime. Using numerical finite-element solutions of the 3D time-harmonic Maxwell equations, we calculate the absorption of light in a thin silicon film with a 3D inverse woodpile photonic crystal as a back reflector. To make our calculations relevant to experimental studies, we employ a dispersive and complex refractive index obtained from experiments [61] and compare the photonic crystal back reflector to a perfect metallic back reflector. We verify that the absorption is not enhanced by the extra material volume. Ultimately, we aim to understand the physics behind large enhancements by identifying the relevant physical mechanisms compared to a standard back reflector.

## II. METHODS

### A. Structure

For the photonic band gap back reflector we have chosen the cubic inverse woodpile crystal structure [62], on account of its broad band gap that is robust to disorder [63, 64], and since this structure is readily fabricated from silicon [65], and thus a suitable candidate for integration with thin silicon film devices. The crystal structure is shown in Fig. 2(a) and consists of two arrays of identical nanopores with radius  $r$  running in two orthogonal directions X and Z. Each nanopore array has a centered-rectangular lattice with lattice parameters  $c$  and  $a$ , see also Appendix A. For a ratio  $\frac{a}{c} = \sqrt{2}$ , the diamond-like structure has cubic symmetry. Cubic inverse woodpile photonic crystals have a broad maximum band gap width  $\Delta\omega/\omega_c = 25.3\%$  relative to the central band gap frequency  $\omega_c$  for pores with a relative radius  $\frac{r}{a} = 0.245$  [63, 64]. Our prior results reveal that a reflectivity in excess of  $R > 99\%$  and a transmission  $T < 1\%$  occur already for a thin inverse woodpile photonic crystal with a thickness of a few unit cells ( $L_{3DPC} \geq 3c$ ) [50, 57]. Therefore, we choose here a cubic inverse-woodpile crystal with an optimal pore radius  $\frac{r}{a} = 0.245$  and with a thickness  $L_{3DPC} = 4c = 1200$  nm as a back reflector for the calculation of the absorption of light by the thin silicon film.

### B. Computations

To calculate the optical absorption in a thin silicon film, we employ the commercial COMSOL Multiphysics finite-element (FEM) software to solve the time-harmonic Maxwell equations [66]. Figure 2 (b) illustrates the computational cell viewed in the  $YZ$  plane. The incident fields start from a plane at the left that is separated from the silicon layer by an air layer. Since the plane also absorbs the reflected waves [67], it represents a boundary condition rather than a true current source. The incident plane waves have either  $s$  polarization (electric field normal to the plane of incidence) or  $p$  polarization (magnetic field normal to the plane of incidence), and have an angle of incidence between  $\theta = 0^\circ$  and  $80^\circ$ . We employ Bloch-Floquet periodic boundaries in the  $\pm X$  and the  $\pm Y$  directions to describe the infinitely extended thin silicon film [49]. To describe a thin film with finite support, absorbing boundaries are employed in the  $-Z$  and  $+Z$  directions. We calculate reflectivity and transmission of the thin film at the absorbing boundaries in the  $-Z$  and  $+Z$  directions, respectively. The light with a given wavelength  $\lambda$  incident at an angle  $\theta$  with respect to the surface normal is either reflected or transmitted, or absorbed by the thin film [30]. To calculate the absorption

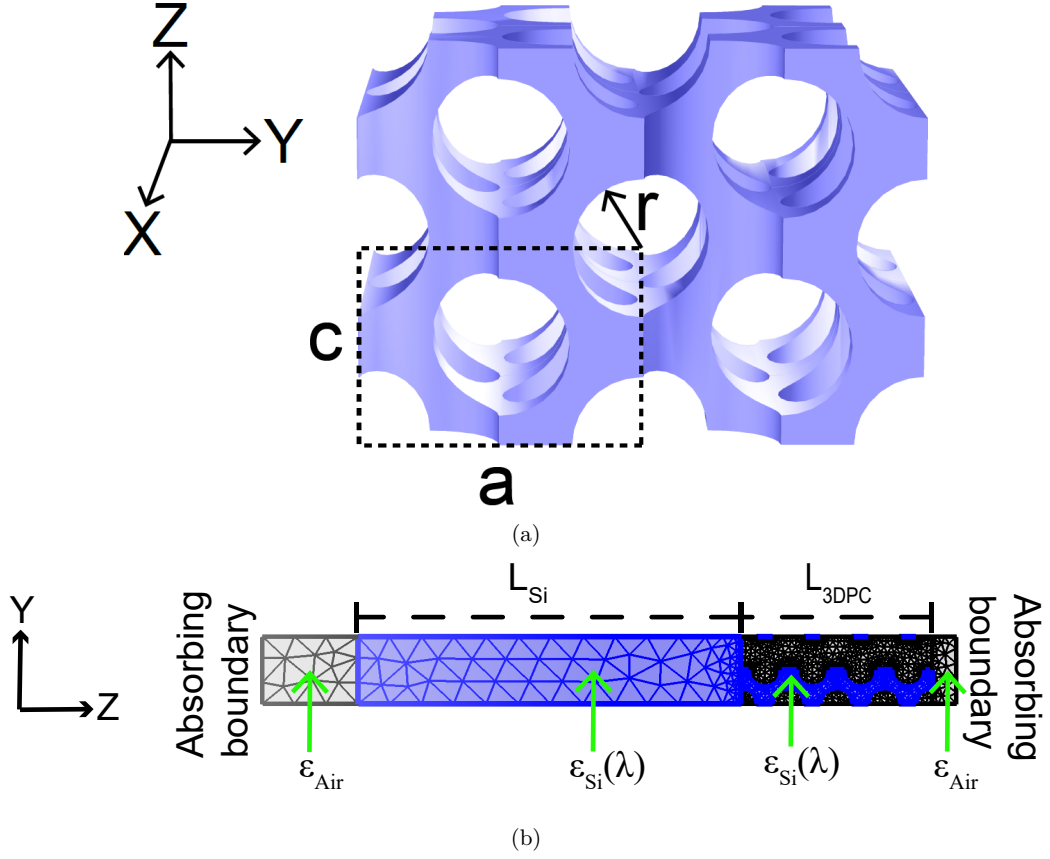


FIG. 2: (a) Schematic of the 3D inverse woodpile photonic crystal structure with the XYZ coordinate axes. We show a  $2 \times 2 \times 2$  supercell, with two arrays of identical nanopores with radius  $r$  parallel to the X and Z axes. The lattice parameters of the tetragonal unit cell are  $c$  and  $a$ , in a ratio  $\frac{a}{c} = \sqrt{2}$  for cubic symmetry. The blue color represents the high-index material with a dielectric function similar to silicon. (b) Computational cell bounded by absorbing boundaries at  $-Z$  and  $+Z$ , and by periodic boundary conditions at  $\pm X$  and  $\pm Y$ . The thin silicon film with thickness  $L_{Si} = 2400$  nm is the absorbing layer and a 3D inverse woodpile photonic crystal with thickness  $L_{3DPC} = 4c = 1200$  nm is the back reflector.

$A_{Si}(\lambda, \theta)$  of a thin silicon film, we employ the relation

$$A_{Si}(\lambda, \theta) = 1 - R_{Si}(\lambda, \theta) - T_{Si}(\lambda, \theta), \quad (1)$$

with  $R_{Si}(\lambda, \theta)$  the reflectivity and  $T_{Si}(\lambda, \theta)$  the transmission spectra that are normalized to the incident light intensity  $I_0$ .

To gauge the performance of a 3D photonic band gap back reflector, we define the wavelength and angle-dependent absorption enhancement  $\eta_{abs}(\lambda, \theta)$  of the thin silicon film in Fig. 2 as

$$\eta_{abs}(\lambda, \theta) \equiv \frac{\int_{\lambda-\Delta\lambda}^{\lambda+\Delta\lambda} P_{AM1.5}(\lambda) A_{(Si+3DPC)}(\lambda, \theta) d\lambda}{\int_{\lambda-\Delta\lambda}^{\lambda+\Delta\lambda} P_{AM1.5}(\lambda) A_{Si}(\lambda, \theta) d\lambda}, \quad (2)$$

where the absorption is weighted with the solar spectrum using the air mass coefficient  $P_{AM1.5}(\lambda)$  [14]. In Eq. 2,  $A_{(Si+3DPC)}$  represents the absorption in a thin silicon film with a 3D photonic crystal back reflector and  $A_{Si}$  the absorption in a thin silicon film with the same thickness, yet no back reflector. Using Eq. 2, the enhancement is averaged over a bandwidth ( $2\Delta\lambda$ ) at every discrete wavelength  $\lambda$ .

At normal incidence ( $\theta = 0^\circ$ ) the absorption enhancement  $\eta'_{abs}(\lambda)$  is deduced from Eq. 2 to

$$\eta'_{abs}(\lambda) \equiv \frac{\int_{\lambda-\Delta\lambda}^{\lambda+\Delta\lambda} P_{AM1.5}(\lambda) A_{(Si+3DPC)}(\lambda) d\lambda}{\int_{\lambda-\Delta\lambda}^{\lambda+\Delta\lambda} P_{AM1.5}(\lambda) A_{Si}(\lambda) d\lambda}. \quad (3)$$

To calculate the angle-averaged absorption enhancement  $\eta''_{abs}(\lambda)$ , the enhancement  $\eta_{abs}(\lambda, \theta)$  (Eq. 2) is averaged over  $n$  incident angles  $\theta_i$  to

$$\eta''_{abs}(\lambda) \equiv \frac{1}{n} \sum_{i=1}^{i=n} \eta_{abs}(\lambda, \theta_i). \quad (4)$$

Figure 2 (b) illustrates the finite element mesh of tetrahedra that are used to subdivide the 3D computational cell into elements [68]. Since the computations are intensive due to a finite element mesh of 167000 tetrahedra, we performed the calculations on the powerful ‘‘Serendipity’’ cluster [69] at MACS in the MESA+ Institute (see also Ref. [59]).

To enhance the weak absorption of silicon above the electronic band gap at wavelengths in the range  $600 \text{ nm} < \lambda < 1100 \text{ nm}$ , we tailor the lattice parameters of the inverse woodpile photonic crystal to  $a = 425 \text{ nm}$  and  $c = 300 \text{ nm}$  such that the band gap is in the visible range. The chosen lattice parameters are 37% smaller than the ones usually taken for photonic band gap physics in the telecom range [50–52, 54–58, 70]. The nanopore radii are taken to be  $\frac{r}{a} = 0.245$ , i.e.,  $r = 104 \text{ nm}$  in order for the broadest possible band gap [63, 64]. The required dimensions are well within the feasible range of nanofabrication parameters [65, 71, 72].

To benchmark our proposition of using a 3D inverse woodpile photonic crystal as a back reflector, we compare the absorption spectra to spectra for the same thin silicon layer with a perfect and omnidirectional metallic back reflector. Therefore, in our simulations we replace the photonic crystal and the air layer on the right in Fig. 2 (b) with a homogeneous metallic plane with a large and purely imaginary refractive index  $n'' = -i \cdot 10^{20}$ .

For reference, we also show results for ideal Lambertian scattering [73], with the understanding that in our calculations we do not consider a scattering front (or back) surface. In the Lambertian case, the absorption  $A_{Si}^L(\lambda)$  of a thin silicon film with thickness  $L_{Si}$  and refractive index  $n_{Si}(\lambda) = \text{Re}(n_{Si}(\lambda)) + i\text{Im}(n_{Si}(\lambda))$  is equal to [74, 75]

$$A_{Si}^L(\lambda) = \frac{\alpha(\lambda)L_{Si}}{\alpha(\lambda)L_{Si} + \frac{1}{F(\lambda)}}, \quad (5)$$

where  $\alpha(\lambda)$  is the absorption coefficient that is equal to  $\alpha(\lambda) = \frac{4\pi\text{Im}(n_{Si}(\lambda))}{\lambda}$ , and  $F(\lambda)$  the optical path length enhancement factor equal to  $F(\lambda) = 4 \text{Re}(n_{Si}(\lambda))^2$ .

### III. RESULTS AND DISCUSSION

In the first two subsections, we show the main results, namely the absorption enhancements for silicon films thicker and thinner than the wavelength. In the subsequent subsections, we discuss detailed physical backgrounds, including film thickness, angular acceptance, and absence of photonic crystal backbone contributions to the overall absorption.

#### A. Supra-wavelength silicon film

Figure 3 shows the normal incidence absorption enhancement  $\eta'_{abs}(\lambda)$  (Eq. 3) of a supra-wavelength  $L_{Si} = 2400 \text{ nm}$  thin silicon film for both the perfect metal and the 3D photonic crystal back reflectors. For the 3D inverse woodpile back reflector, the absorption enhancement varies between  $\eta'_{abs} = 1\times$  and  $9\times$  inside the stop bands between  $\lambda = 640 \text{ nm}$  and  $900 \text{ nm}$ . The wavelength-averaged absorption enhancement is about  $\langle \eta'_{abs} \rangle = 2.22\times$  for the  $s$ -stop band and  $\langle \eta'_{abs} \rangle = 2.45\times$  for the  $p$ -stop band. In comparison, for a perfect metal back reflector the wavelength-averaged absorption enhancement is about  $\langle \eta'_{abs} \rangle = 1.47\times$  for the  $s$ -stop band and  $\langle \eta'_{abs} \rangle = 1.56\times$  for the  $p$ -stop band. Since a perfect metal back reflector has 100% specular reflectivity only in the specular 0<sup>th</sup> diffraction order, the absorption enhancement  $\eta'_{abs}$  is always less than two:  $\langle \eta'_{abs} \rangle \leq 2$ . In contrast, a photonic band gap crystal back reflector also has non-zero order diffraction modes, see Fig. 1, that scatter light into guided modes where light is confined inside the thin silicon film via total internal reflection. Since the effective optical path length travelled by a photon in a guided mode is longer than the path length travelled with only the 0<sup>th</sup> order diffraction mode, a photonic crystal back

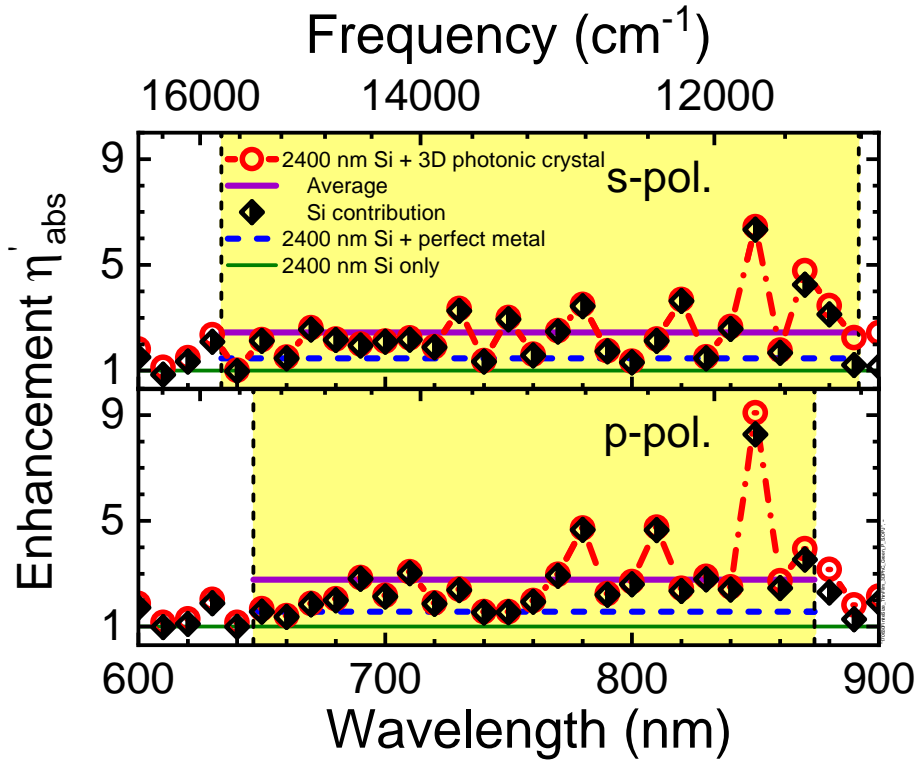


FIG. 3: Normal incidence absorption enhancement spectra  $\eta'_{abs}(\lambda)$  for a thin silicon film ( $L_{Si} = 2400$  nm) with several back reflectors computed using Eq. 3 with a bandwidth  $2\Delta\lambda = 10$  nm at each wavelength bin  $\lambda$ . The top panel is for  $s$ -polarized light and the bottom panel for  $p$ -polarized light. Red connected circles are data for a thin film with the 3D photonic crystal back reflector, the purple horizontal line is the average enhancement (using Eq. 3 with a bandwidth  $2\Delta\lambda$  equal to the  $s$ - and  $p$ -stop bands, respectively), the black diamonds are for the thin film part only, and the blue short-dashed line is for the thin film with a perfect metal back reflector. The vertical dashed lines show the edges of the  $s$ - and  $p$ -stop bands, with the stop bands shown as yellow bars.

reflector yields a greater absorption enhancement  $\langle \eta'_{abs} \rangle \geq 2$  for the diffracted wavelengths, as is apparent in Fig. 3. This observation is a first support of the notion that a 3D photonic band gap back reflector enhances the absorption of a thin silicon film by (i) behaving as a perfect reflector with nearly 100% reflectivity for both polarizations, and (ii) exciting guided modes within the thin film.

Since the high-index backbone of the 3D inverse woodpile photonic crystal consists of silicon, one might surmise that the absorption is enhanced by the addition of the photonic crystal's silicon backbone to the thin silicon film. To test this hypothesis, we calculate the absorption enhancement within the thickness  $L_{Si}$  of the thin silicon film part (see Fig. 2 (b)) using the volume integral of the total power dissipation density from Ref. [66]. Figure 3 shows that the absorption enhancement spectra for the thin film volume agree very well with the spectra of the complete device (both thin film and photonic crystal) in the stop bands between  $\lambda = 640$  nm and 900 nm. Therefore, the high-index backbone of the 3D photonic crystal contributes *negligibly* to the absorption inside the stop bands, even in the visible regime. Apparently, light that travels from the thin film into the photonic crystal is reflected back into the thin film, even before it is absorbed in the photonic crystal. To bolster this conclusion, we start with the notion that the typical length scale for reflection by a photonic crystal is the Bragg attenuation length  $\ell_{Br}$  [76] that qualitatively equals the ratio of the central stop band wavelength and the photonic interaction strength  $S$  times  $\pi$ :  $\ell_{Br} = \lambda_c / (\pi S)$  [77, 78], where the strength  $S$  is gauged by the ratio of the dominant stop band width and the central wavelength ( $S = \Delta\lambda / \lambda_c$ ). From the stop band between  $\lambda = 640$  nm and 900 nm ( $S = 260/770 = 0.34$ ) we arrive at  $\ell_{Br} = 770 / (\pi \cdot 0.34) = 725$  nm, which is much less than the absorption length of silicon:  $\ell_{Br} \ll l_a$ . Thus, the broad bandwidth of the back reflector's 3D photonic band gap is an important feature to enhance the absorption inside the thin silicon film itself, as the broad bandwidth corresponds to a short Bragg length.

## B. Sub-wavelength silicon film

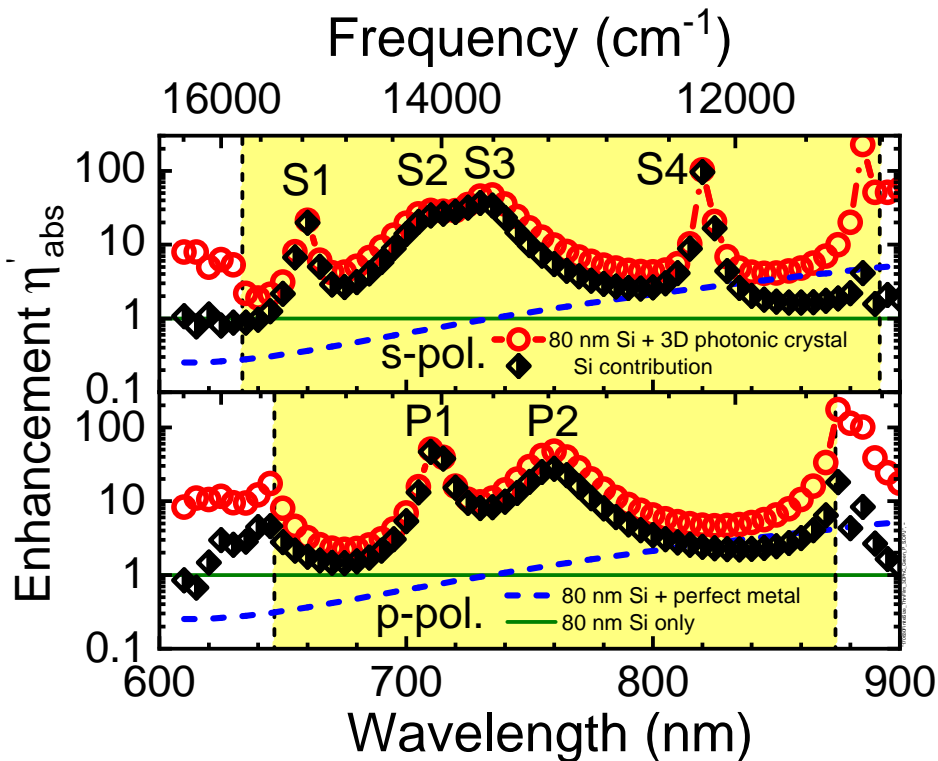


FIG. 4: Absorption enhancement spectra  $\eta'_{abs}(\lambda)$  for a sub-wavelength ultrathin silicon layer ( $L_{Si} = 80$  nm), taken as ratio of absorption  $A$  with a back reflector and absorption  $A_{Si}$  without back reflector, all at normal incidence computed using Eq. 3. Top panel:  $s$ -polarized, bottom panel:  $p$ -polarized light, with  $s$ - and  $p$ -stop bands shown as yellow highlighted regions. Red connected circles pertain to the ultrathin film with a 3D photonic crystal back reflector and the black diamonds are for the silicon part only. The blue dashed curves pertain to the ultrathin film with a perfect metal back reflector and the green lines are the reference level of the ultrathin film without a back reflector.

Figure 4 shows the normal incidence absorption enhancement  $\eta'_{abs}(\lambda)$  (Eq. 3) of a  $L_{Si} = 80$  nm ultrathin silicon film, whose thickness is much less than the wavelength in the material ( $L_{Si} \ll \lambda/n$ ), hence no guided modes are sustained in the film itself. Since the thickness is also much less than the silicon absorption length  $L_{Si} \ll l_a = 1000$  nm between  $\lambda = 600$  nm and 900 nm [61], the absorption  $A_{Si}$  of the ultrathin film itself is low, namely about 4.5% at the blue edge of the photonic stop bands) and 0.2% at the red edge of the stop band, see Fig. 5. These results agree with a Fabry-Pérot analysis of the ultrathin film, which reveals a broad first order resonance near  $\lambda = 570$  nm that explains the increased absorption towards the short wavelengths.

For the perfect metal back reflector in Fig. 4, the absorption is reduced ( $\eta'_{abs}(\lambda) < 1$ ) at wavelengths  $\lambda < 730$  nm and enhanced ( $\eta'_{abs}(\lambda) > 1$ ) at longer wavelengths. This result is understood from the Fabry-Pérot behavior of the ultrathin film in presence of the perfect metal, that induces an additional  $\pi$  phase shift (due to the exit surface reflectivity) to the round-trip phase. Consequently, a first order resonance appears near  $\lambda = 1140$  nm, and the next anti-resonance near  $\lambda = 600$  nm. Therefore, the absorption is enhanced towards  $\lambda = 1140$  nm and reduced towards  $\lambda = 600$  nm, in agreement with the results in Fig. 4. The corresponding wavelength-averaged absorption enhancements are  $\langle \eta'_{abs} \rangle = 0.8\times$  for  $s$ -polarized and  $\langle \eta'_{abs} \rangle = 0.85\times$  for the  $p$ -polarized stop band. In other words, a perfect metal back reflector hardly enhances the absorption for ultrathin films with the thickness corresponding to a Fabry-Pérot minimum for the desired wavelengths of absorption enhancement.

In presence of a photonic band gap back reflector, the wavelength-averaged absorption enhancement is surprisingly larger, see Fig. 4. The strong increase is clearly illustrated by the use of a logarithmic scale. We see several peaks

between  $\lambda = 600$  nm and 900 nm in Fig. 4, four absorption resonances (S1, S2, S3, and S4) inside the  $s$ -polarized stop band and two absorption resonances (P1 and P2) inside the  $p$ -polarized stop band with enhancements as high as  $\eta'_{abs} = 100\times$  for both polarizations. The wavelength-averaged enhancements are  $\langle\eta'_{abs}\rangle = 13.5\times$  for the  $s$ -polarized stop band and  $\langle\eta'_{abs}\rangle = 11.4\times$  for the  $p$ -polarized stop band. Since the thickness of the ultrathin silicon  $L_{Si} = 80$  nm does not sustain guided modes at the wavelengths within these stop bands, the enhanced absorption peaks must be induced by the presence of the photonic crystal back reflector, which has an effective refractive index smaller than that of silicon (see Appendix A), and hence leads to no phase shift like the metallic back reflector.

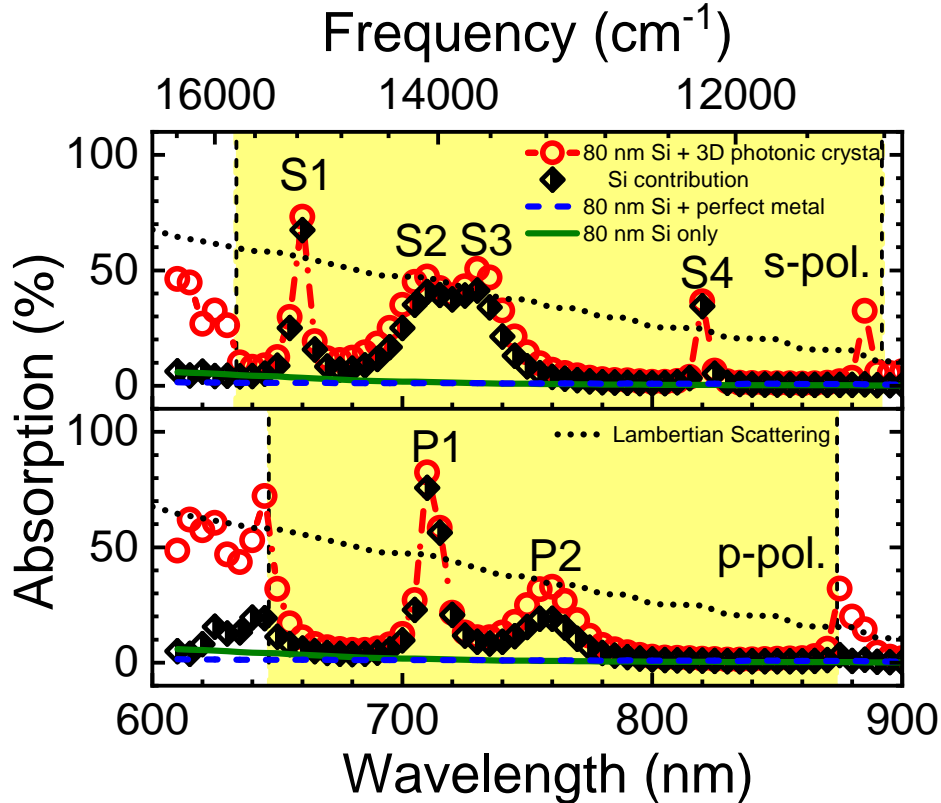


FIG. 5: Absolute absorption spectra (in %) for a sub-wavelength ultrathin silicon layer ( $L_{Si} = 80$  nm) at normal incidence. Top panel:  $s$ -polarized, bottom panel:  $p$ -polarized light, with  $s$ - and  $p$ -stop bands shown as yellow highlighted regions. Red connected circles pertain to the ultrathin film with a 3D photonic crystal back reflector, whereas the black diamonds show the contribution of the ultrathin film only. Green solid curves pertain to an ultrathin film without a back reflector, and blue dashed curves to an ultrathin film with a perfect metal back reflector. Black dotted curves represent absorption  $A_{Si}^L(\lambda)$  with Lambertian scattering, from Eq. 5.

Considering that this ultrathin silicon layer is much thinner than the one in Sec. III A, there is a likelihood that the absorption is enhanced by the extra silicon volume from the photonic crystal's backbone, whose thickness is much greater than the film thickness, namely  $L_{3DPC} = 1200$  nm versus  $L_{Si} = 80$  nm. To test this hypothesis, we calculated the absorption within the volume of the ultrathin silicon film part only ( $L_{Si} = 80$  nm), using the power per unit volume formula of Ref. [66], as shown in Fig. 5 (from which Fig. 4 is deduced) with various back reflectors for  $s$  and  $p$  polarizations. The enhanced absorption at all six resonances S1-S4, and P1-P2 occur in the ultrathin film volume only. The wavelength-averaged absorption enhancement within the ultrathin film part is  $\langle\eta'_{abs}\rangle = 10.46\times$  averaged over the  $s$ -polarized stop band and  $\langle\eta'_{abs}\rangle = 7.84\times$  for the  $p$ -polarized stop band, which are nearly the same as in the full device. Therefore, we conclude that the absorption in the photonic crystal hardly contributes to the enhanced absorption and does not induce the presence of the absorption peaks. Figure 4 reveals that the absorption within the ultrathin film and the one within the whole device (both ultrathin film and photonic crystal) match very well near the center of the  $s$ - and  $p$ -stop bands and differ at the edges. The reason is that the Bragg attenuation length  $\ell_{Br}$  is smallest near the center of the stop band, while it increases toward the band edges where it leads to more absorption



in the crystal before the light is reflected within a Bragg length.

For reference, Fig. 5 also shows the absorption limit due to Lambertian scattering (Eq. 5) for the  $L_{Si} = 80$  nm ultrathin film. We note that in between the resonances, the absorption with the 3D photonic band gap back reflector is below the Lambertian limit. In contrast, at all six  $s$ - and  $p$ -polarized resonances (S1-S4 and P1-P2) the 3D photonic band gap back reflector results exceed the Lambertian absorption, with the footnote that our calculation invokes a flat top surface and no optimized scattering surface. In the modern view, an absorption beyond Lambertian limit occurs if the local density of states (LDOS) inside the absorbing layer exceeds the LDOS outside [25]. In one view point, the combination of ultrathin film with photonic back reflector leads to new resonances (S1-S4 and P1-P2, see below) that have a higher LDOS than the vacuum before the absorbing layer (above in Fig. 1). Alternatively, since a photonic band gap blocks all incident radiation and inhibits the LDOS, a photonic band gap back reflector may be viewed as a peculiar “colored electromagnetic vacuum” [79] below the absorbing film that has a much lower LDOS than the one in the film itself.

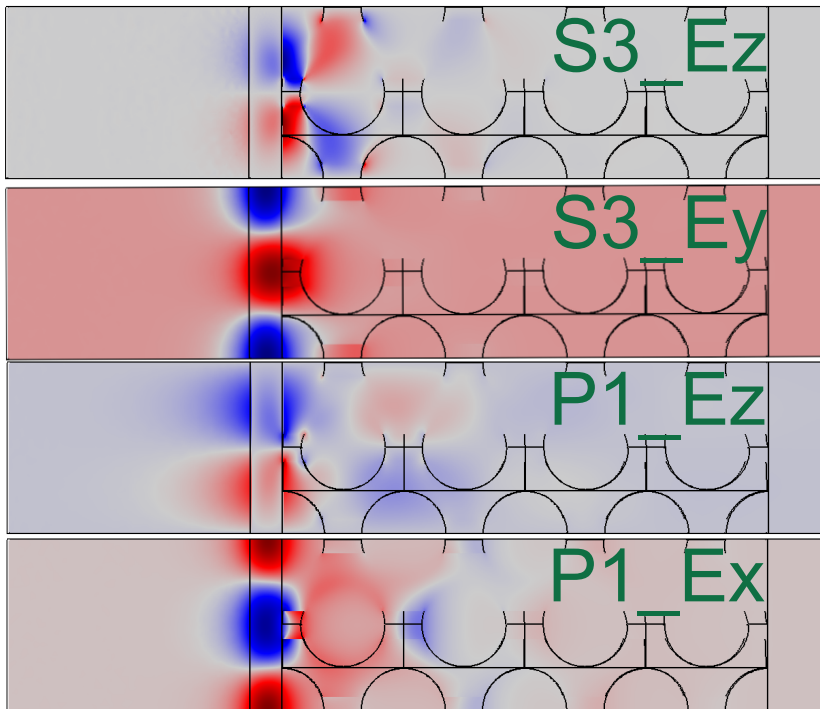


FIG. 6: Distribution of the electric field components for waves propagating in the sub-wavelength ultrathin film ( $L_{Si} = 80$  nm) with a 3D photonic band gap back reflector. S3 and P1 are absorption resonances from Fig. 4, and we show field components that are not present in the incident waves. Red and blue denote the maxima and the minima of the electric field components, respectively.

To investigate the physics behind these intriguing peaks, we discuss the electric field distributions for the exemplary resonances S3 and P1. The incident light with wavevector in the Z-direction has either  $s$  polarization ( $\mathbf{E}$ -field in the X-direction) or  $p$  polarization ( $\mathbf{E}$ -field in the Y-direction). To filter the scattered electric fields that are guided in the plane of the ultrathin layer from possibly overwhelming incident fields, we plot in Fig. 6 the field components that are *absent* in the incident light. Thus, we plot the  $E_z$  and  $E_y$  field components of the S3 resonance that is excited by  $s$ -polarized light ( $\mathbf{E}_{in,X}$ ), and the  $E_z$  and  $E_x$  components of the P1 resonance that is excited by  $p$ -polarized light ( $\mathbf{E}_{in,Y}$ ).

First, we discuss the S3  $E_y$  and P1  $E_x$  field components that are transverse to the incident direction, and perpendicular to the incident polarization. Both components are maximal inside the ultrathin silicon film, as expected for guided waves. The field distributions show periodic variations in the plane of the ultrathin film that are also characteristic of guided modes [35, 80]. The periods match with the crystal’s lattice parameter, which suggests that the fields are part of a Bloch mode. The fields extend into the photonic crystal by about one unit cell, in agreement with a Bragg attenuation length of about  $\ell_{Br} = 0.6c = 180$  nm at the  $p$ -stop band center that was computed in Ref. [50].

For the other two field components S3  $E_z$  and P1  $E_z$ , the maximum fields are located at the air-silicon and at the

silicon-photonic crystal interfaces, and the amplitudes decay away from the interfaces. The components show less conventional guiding behavior: the S3  $E_z$  component is maximal just *inside* the photonic crystal (by about a quarter unit cell), and has a nodal plane parallel to the ultrathin film. The P1  $E_z$  component has maxima on either side of the ultrathin silicon film, somewhat like the field pattern of a long-range surface plasmon polariton (LRSPP) on a thin metal film [81, 82]. This field extends about  $\Delta Z = 1$  unit cell into the crystal. These field distributions are the plausible signature of the confinement of a surface mode [49, 83]. Hence, the device can be viewed as an ultrathin absorbing dielectric film on top of a photonic crystal, which thus acts as a surface defect on the crystal and sustains a guided surface state. Consequently, the remarkable peaks observed in Fig. 4 correspond to guided modes confined in an ultrathin layer consisting of two separate contributions: (i) a non-zero thickness layer due to the Bragg attenuation length of the crystal's band gap, and (ii) a deeply sub-wavelength ultrathin silicon film.

### C. Wavelength-resolved transmission and absorption

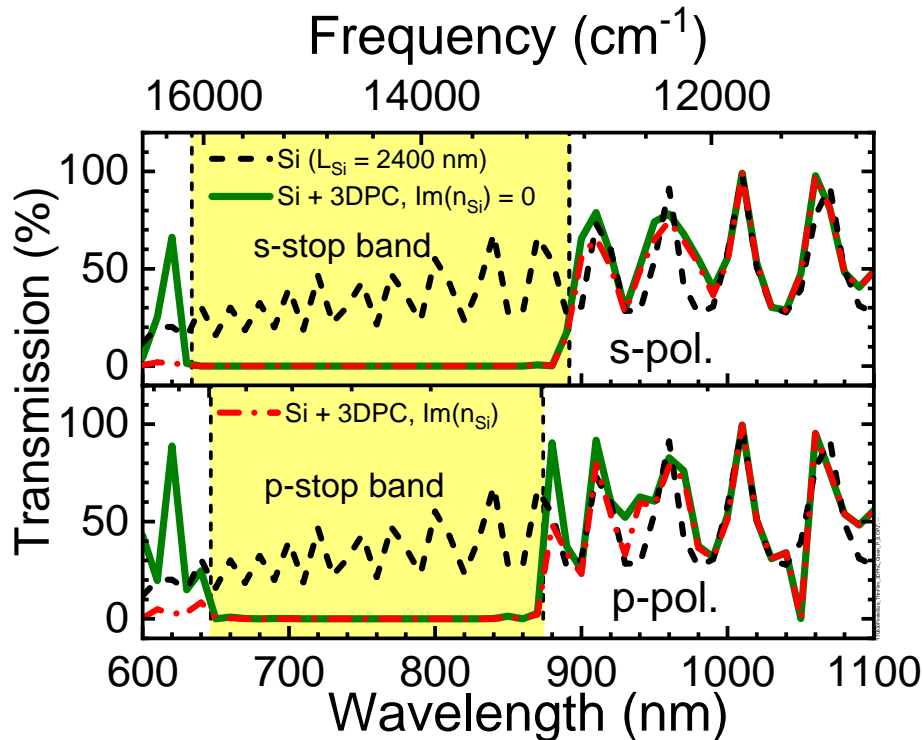


FIG. 7: Transmission spectra calculated for a thin silicon film ( $L_{Si} = 2400$  nm) at normal incidence. Top panel:  $s$  polarization, bottom panel:  $p$  polarization. Black dashed curves are the transmission spectra for a thin film. Green solid curves are results for the thin film with a 3D inverse woodpile photonic crystal back reflector, with dispersion but no silicon absorption ( $\text{Im}(n_{Si}) = 0$ ). Red dashed-dotted curves are results for the thin film with a 3D inverse woodpile photonic crystal back reflector, including silicon absorption ( $\text{Im}(n_{Si}) \neq 0$ ). The vertical dashed lines are the edges of the  $s$ - and  $p$ -stop bands that are shown as yellow bars.

To analyze the physics behind the results in Sections III A and III B, we break the problem down into several steps. Firstly, we briefly recapitulate the known situation of a thin silicon film only. Secondly, we study the thin film with a photonic crystal back reflector, where we only consider dispersion, but no absorption. This fictitious situation allows a comparison to the dispersion-free results that pertain to frequencies below the silicon band gap, see Ref. [50]. Thirdly, we study the complete device structure with the full silicon dispersion and absorption taken from Ref. [61].

Figure 7 reveals oscillations between  $\lambda = 600$  nm and  $\lambda = 1100$  nm for both polarizations in the transmission spectra for the thin silicon film ( $L_{Si} = 2400$  nm). These oscillations are Fabry-Pérot fringes [84] resulting from multiple reflections of the waves inside the film at the front and back surfaces of the thin silicon film.

In Fig. 7, we observe nearly 0% transmission between  $\lambda = 600$  nm and  $\lambda = 900$  nm for a thin film with a photonic crystal back reflector, both with and without silicon absorption. These deep transmission troughs are photonic stop bands between  $\lambda = 647$  nm to 874 nm for  $p$  polarization and  $\lambda = 634$  nm to 892 nm for  $s$  polarization. These gaps were previously identified to be the dominant stop gaps in the  $\Gamma - X$  and  $\Gamma - Z$  high-symmetry directions (see Appendix B) that encompass the 3D photonic band gap [50]. From the good agreement of the stop bands, both with and without silicon absorption, we deduce that an inverse woodpile photonic crystal behaves as a perfect reflector in the visible range, even in presence of substantial absorption. This result further supports the above observation that the absorption length of silicon is much longer than the Bragg attenuation length of the 3D inverse woodpile photonic crystal  $l_a \gg \ell_{Br}$ . Hence, waves incident on the photonic crystal are reflected before being absorbed by the high-index backbone of the photonic crystal. Thus, the Fabry-Pérot fringes in transmission between  $\lambda = 600$  nm and  $\lambda = 860$  nm are completely suppressed by strong and broadband reflection of the 3D photonic crystal back reflector [50].

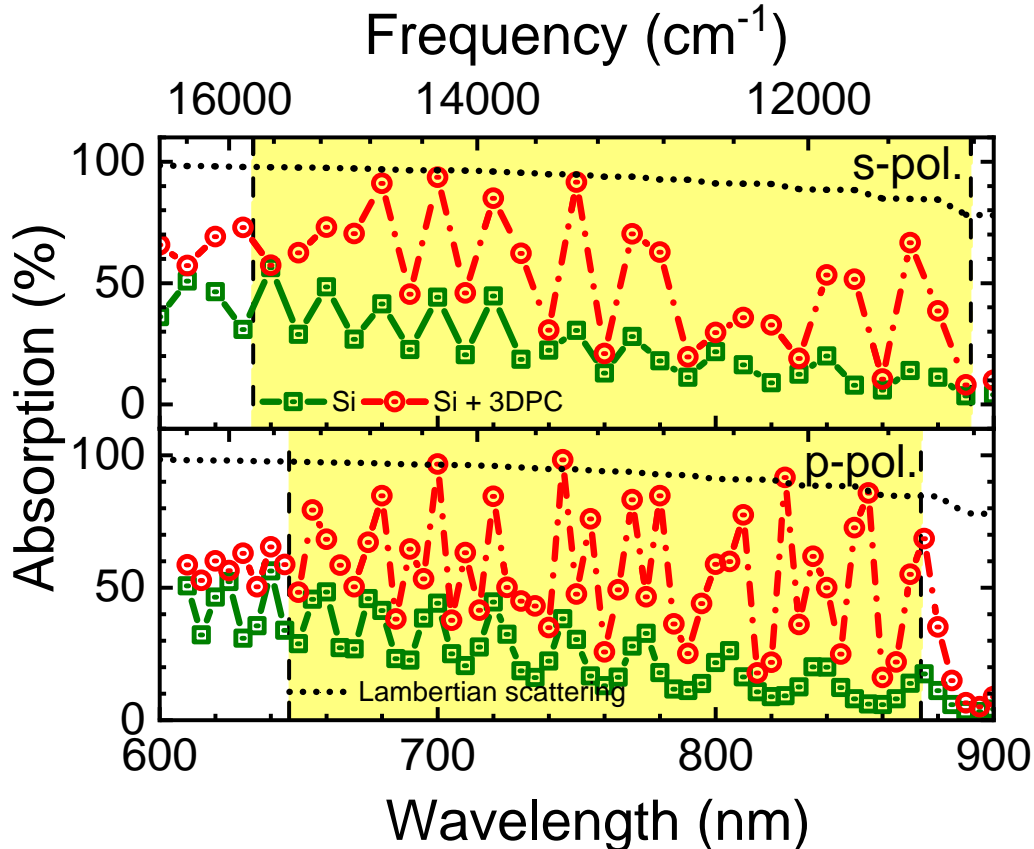


FIG. 8: Absolute absorption (in %) by a thin silicon film ( $L_{Si} = 2400$  nm) in the stop band of a 3D inverse woodpile photonic crystal. Top panel:  $s$ -polarized, bottom panel:  $p$ -polarized light. Green solid curves are absorption spectra for a thin silicon film. Red dashed-dotted curves are absorption spectra for a thin silicon film with a 3D inverse woodpile photonic crystal back reflector. The vertical dashed lines are the edges of the  $s$ - and  $p$ -stop bands. The stop bandwidths are shown as the yellow bar. Black dotted curves represent absorption  $A_{Si}^L(\lambda)$  with Lambertian scattering, from Eq. 5.

Furthermore, oscillations below  $\lambda = 600$  nm are present in the transmission spectra for the thin silicon film with a photonic crystal back reflector without absorption, but not in the system with absorption. Since the transmission spectra with realistic absorption show nearly 0% transmission below  $\lambda = 600$  nm, where silicon is strongly absorbing, all light is absorbed and the Fabry-Pérot fringes are suppressed.

Figure 8 shows the absorption spectra for a thin silicon film without and with a 3D photonic crystal back reflector. We consider the dispersive and complex refractive index for the silicon and the high-index backbone of the photonic

crystal. Fabry-Pérot fringes appear below  $\lambda = 900$  nm, corresponding to standing waves in the thin silicon film. Since the imaginary part of the silicon refractive index increases with decreasing wavelength (see Fig. 15), the absorption in silicon also increases with decreasing wavelength.

Between  $\lambda = 600$  nm and  $\lambda = 900$  nm in the top and bottom panels of Fig. 8, there are more Fabry-Pérot fringes. The fringes have a greater amplitude for a thin silicon film with photonic crystal back reflector, compared to a standalone thin silicon film. To interpret the increased number of fringes, we consider diffraction from the photonic crystal surface. In Fig. 1, light first travels through silicon before reaching the photonic crystal surface. Therefore, the incident wavelength reduces to  $\lambda/n_{Si}$  inside the silicon layer. In the entire stop bands (both  $s$  and  $p$ ) the wavelength  $\lambda/n_{Si}(\lambda)$  between  $\lambda = 600$  nm and  $\lambda = 900$  nm is smaller than the lattice parameter  $c = 300$  nm of the 3D inverse woodpile photonic crystal (along the  $\Gamma Z$  direction). In addition, a 3D inverse woodpile photonic crystal introduces a periodic refractive index contrast at the interface with a thin silicon film. Hence, nonzero diffraction modes [45, 49] are generated at the photonic crystal-thin silicon film interface at specific wavelengths inside the stop bands, resulting in additional reflected waves that are then absorbed in the film.

Between  $\lambda = 600$  nm and 900 nm, the silicon thickness  $L_{Si} = 2400$  nm is larger than half the wavelength  $\lambda/n_{Si}$  in the absorbing layer. This is the condition for a photonic crystal-thin silicon film interface to couple the reflected waves into the guided modes [30, 42] that propagate inside the silicon. Hence, the physical mechanism responsible for the additional number of fringes is the occurrence of non-zero diffraction modes coupled into guided modes due to the photonic crystal back reflector. The absorption in guided modes can sometimes approach 100% [42], *e.g.*, at  $\lambda = 700$  nm and 720 nm in Fig. 8 (bottom). We note that the perfect reflectivity of a 3D inverse woodpile photonic crystal extends over the entire stop bands, whereas nonzero order diffraction modes and guided modes are limited to specific wavelengths. This is in contrast to Section III B, where we studied a reduced thickness such that no guided modes are allowed.

For reference, Fig. 8 also shows the absorption limit due to Lambertian scattering (Eq. 5). In most of the spectral range, the absorption with the 3D photonic band gap back reflector is below the Lambertian limit. At several resonances, the photonic band gap back reflector results match or even slightly exceed the Lambertian limit, again with the note that our calculation does not invoke an optimized scattering surface. The fact that at this thickness the results exceed the Lambertian limit less than in the earlier ultrathin case makes intuitive sense; if we consider the silicon film as a Fabry-Pérot resonator, and we consider a certain constant wavelength, then a thicker resonator corresponds to a greater reduced frequency ( $L_{Si}/\lambda$ ) and will show less LDOS modulation than a thin low ( $L_{Si}/\lambda$ ) resonator. Therefore [25], the thick resonator is less likely to reveal beyond-Lambertian absorption, in agreement with our results.

#### D. Negligible absorption inside the photonic crystal backbone

Since we propose the back reflector to be a photonic crystal that is also made of silicon, one might rightfully hypothesize that the mere presence of extra material in the photonic crystal simply increases the total length of silicon, which thus *sneakily* enhances the absorption. To evaluate this hypothesis, we compute and compare the absorption for three different devices. We first study a thin silicon film of thickness  $L_{Si} = 2400$  nm without back reflector, neither perfect metal nor photonic band gap (device #1). Secondly, we consider a silicon film ( $L_{Si} = 2400$  nm) with a photonic crystal back reflector with a thickness  $L_{Si} = 1200$  nm; this device #2 has a total thickness of 3600 nm. Thirdly, we study a structure with the same total thickness as the second one, namely a silicon layer with a thickness  $L_{Si} = 3600$  nm, but without back reflector (device #3).

To investigate the effect of the band gap on the absorption in the thin film, we zoom in on the absorption spectra inside the stop bands in Fig. 9. We observe that the absorption spectra are closely the same for both thin films (devices #1 and #3), including the Fabry-Pérot fringes. Since film #3 is considerably thicker than #1, the similarity strongly suggests that the silicon absorption within the stop band wavelength range is saturated for the thinner layer.

In contrast, device #2 with a photonic crystal back reflector reveals significantly higher absorption, including a larger amplitude of the Fabry-Pérot fringes than the films #1 and #3. Since the total thickness of device #2 is the same as for film #3, we conclude that the enhanced absorption of the film with the photonic band gap back reflector is *not* caused by the additional thickness of the back reflector itself, hence the *sneaky* effect does not exist. The conclusion that the back reflector does not absorb is also reasonable, since we have seen above that the absorption of the light mostly occurs within the films themselves. Using Eq. 2, we find that the wavelength-averaged absorption enhancement due to a photonic crystal back reflector is nearly  $\langle \eta'_{abs} \rangle = 1.8\times$  for the  $s$ -stop band and nearly  $\langle \eta'_{abs} \rangle = 1.9\times$  for the  $p$ -stop band compared to a thin film with thickness  $L_{Si} = 3600$  nm.

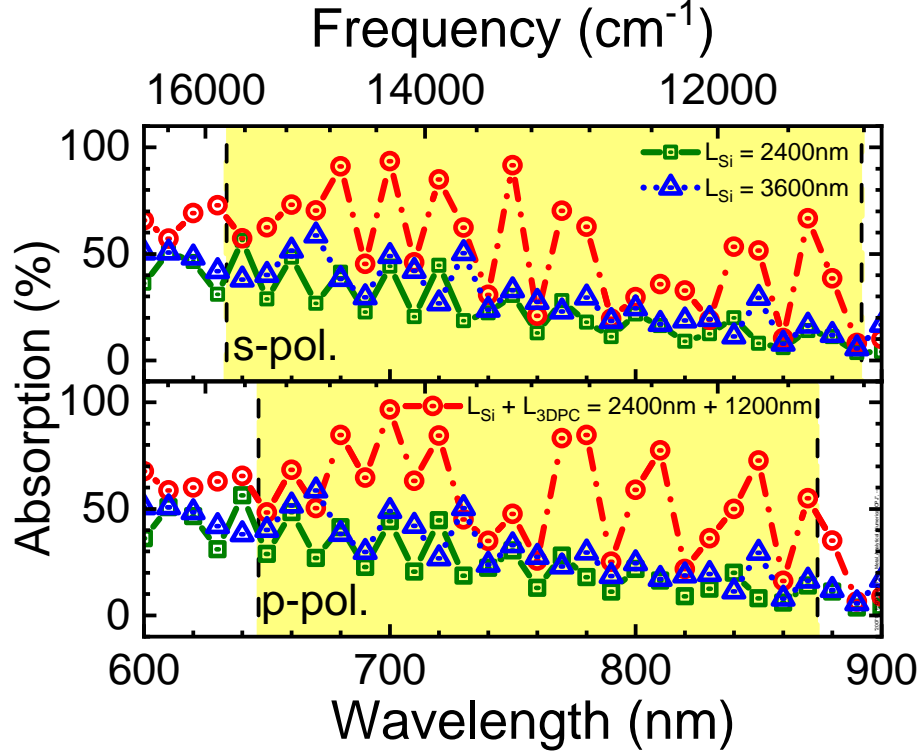


FIG. 9: Verification of the absence of absorption inside the photonic crystal backbone. Top panel:  $s$ -polarized, bottom panel:  $p$ -polarized light, with  $s$ - and  $p$ -stop bands shown as yellow highlighted regions. Green solid curves pertain to a thin film only with the silicon thickness  $L_{Si} = 2400$  nm. Red dashed-dotted curves pertain to a thin silicon film (thickness  $L_{Si} = 2400$  nm) with a 3D photonic crystal back reflector (thickness  $L_{3DPC} = 1200$  nm). Blue dotted curves pertain to a thin film only with the same overall thickness  $L_{Si} = 3600$  nm.

#### IV. PRACTICAL CONSIDERATIONS FOR DEVICES

##### A. Angular acceptance

In order to optimize the absorption of a thin silicon film, we first investigate the impact of a 3D photonic crystal back reflector on the angular acceptance. Figures 10 (a, b) show transmission maps versus angle of incidence and wavelength. The angle of incidence is varied up to  $\theta = 80^\circ$  off the normal. For both polarizations *simultaneously* we observe a broad angle-independent stop band that is characterized by near 0% transmission. The broad stop band extends all the way from  $\lambda = 680$  nm to  $\lambda = 880$  nm. This shows that the Bragg attenuation length for the 3D inverse woodpile photonic crystal is smaller than the absorption length of silicon for all incident angles for the omnidirectional stop band. Thus, a 3D photonic band gap crystal acts as a perfect reflector in the omnidirectional stop band for all incident angles and for all polarizations, even with full absorption in the refractive index - in other words, an *omnidirectional stop band*.

Figure 11 shows the absorption enhancement  $\eta_{abs}(\lambda, \theta)$  versus incident angle for five representative wavelengths throughout the band gap of a 3D inverse woodpile back reflector. For all incident angles up to  $80^\circ$ , we observe that the absorption enhancement stays above 1, which corresponds a standalone thin film. Furthermore, at certain incident angles, the absorption enhancement is as high as 7 or 9. For both polarizations, Fig. 11 also reveals oscillatory absorption enhancement with increasing incident angles, which are signature of the Fabry-Pérot fringes [84]. Hence, a 3D inverse woodpile crystal widens the angular acceptance of a thin silicon film by creating an omnidirectional absorption enhancement regime.

To calculate the angle-averaged and wavelength-averaged absorption enhancement  $\langle \eta''_{abs} \rangle$  in the *omnidirectional stop band*, we employ Eq. 4. Consequently, the angle- and wavelength-averaged absorption enhancement for  $s$  polarization

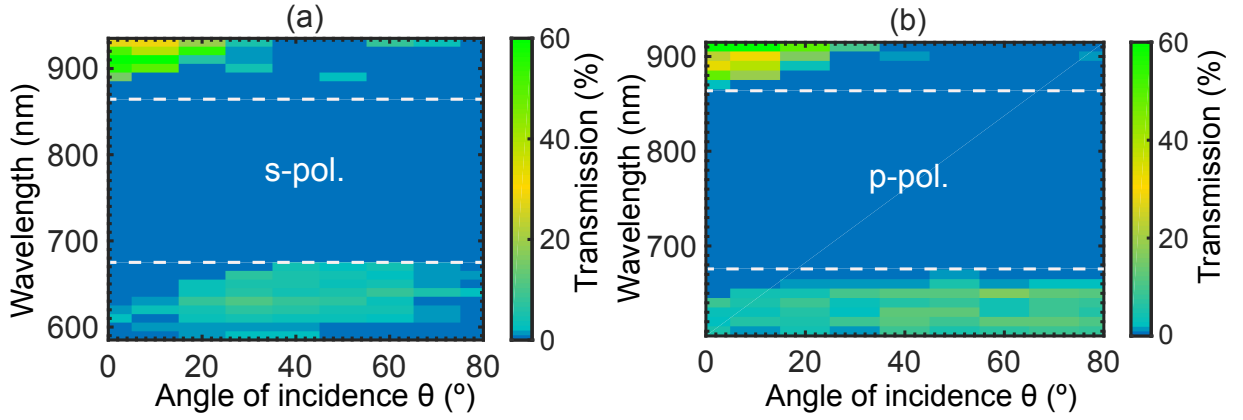


FIG. 10: Angle- and wavelength-resolved transmission spectra calculated for a thin silicon film ( $L_{Si} = 2400$  nm) with a 3D inverse woodpile photonic crystal back reflector for (a)  $s$  polarization and (b)  $p$  polarization. The dark blue color represents nearly 0% transmission that occurs in the stop band at all incident angles. The white dashed box indicates an angle- and polarization-independent range with nearly 0% transmission.

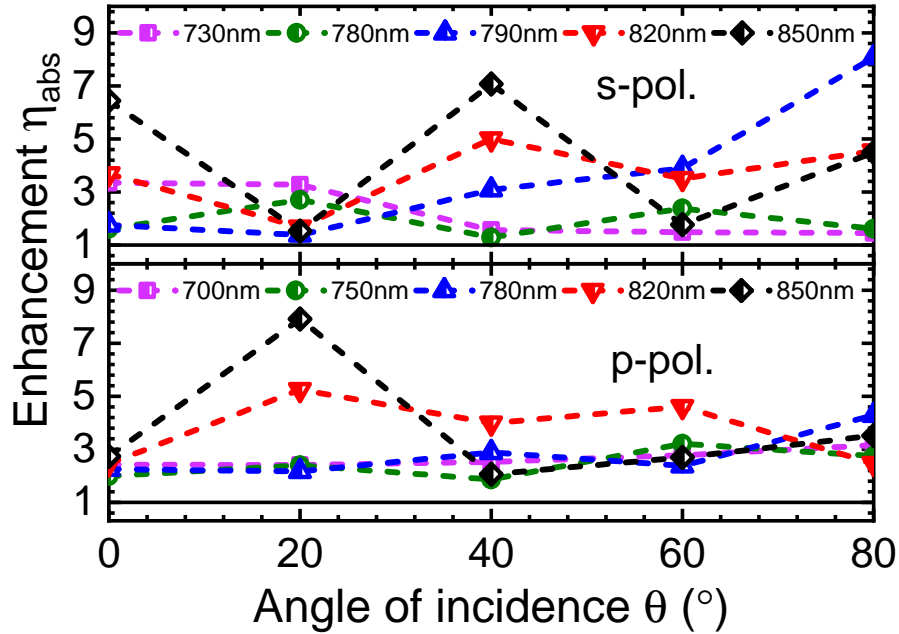


FIG. 11: Absorption enhancement  $\eta_{abs}(\lambda, \theta)$  versus incidence angle  $\theta$  off the surface normal to characterize the angular acceptance of a thin silicon film ( $L_{Si} = 2400$  nm) with a 3D inverse woodpile back reflector, for 5 wavelengths throughout the band gap (850 nm, 820 nm, 790 nm, 760 nm, and 730 nm) with connected symbols and colors as shown in the legend. The top panel is for  $s$ -polarized light, and the bottom panel for  $p$ -polarized light.

is  $\langle \eta_{abs}'' \rangle = 2.11 \times$  and for  $p$  polarization is  $\langle \eta_{abs}'' \rangle = 2.68 \times$ , which exceeds the maximum absorption enhancement feasible for a perfect metallic reflector. These enhancements are possible only if a photonic crystal back reflector generates non-zeroth order diffraction modes at certain discrete wavelengths for all incident angles [85]. Once these non-zero diffraction modes couple into guided modes and are confined inside the thin film via total internal reflection, the effective optical path length travelled is longer than the one travelled by a zero order diffraction mode. Therefore, a 3D inverse woodpile crystal enhances the absorption of a thin silicon film for all incident angles and polarizations by (i) revealing perfect reflectivity inside the omnidirectional stop band and (ii) generating guided modes for specific

wavelengths.

### B. Optimal thickness of the absorbing thin film

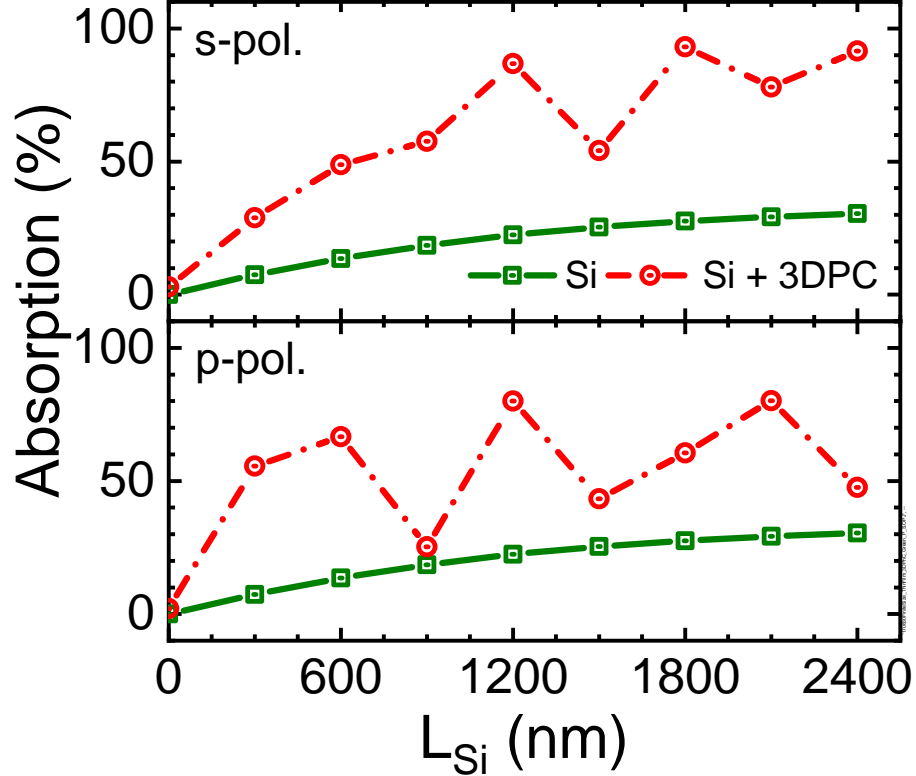


FIG. 12: Absorption versus thickness  $L_{Si}$  of a thin silicon film in presence (connected red circles) of a 3D photonic crystal back reflector, and without back reflector (green squares). The data pertain to a wavelength  $\lambda = 760$  nm, the 3D photonic band gap center of the back reflector. Top panel:  $s$ -polarized, bottom panel:  $p$ -polarized light.

To investigate the effect of the thickness  $L_{Si}$  of the thin silicon film on its absorption, we plot in Fig. 12 the absorption for light at normal incidence for film thicknesses between  $L_{Si} = 300$  nm and  $L_{Si} = 2400$  nm in presence of a 3D inverse woodpile photonic crystal back reflector with a constant thickness  $L_{3DPC} = 1200$  nm. While the absorption for a thin film shows a monotonic increase with increasing silicon thickness for both polarizations, Fig. 12 reveals that the absorption for a thin film with a photonic crystal back reflector is always higher than the corresponding standalone thin film. Furthermore, absorption spectra of a thin film with a photonic crystal back reflector reveals oscillations with increasing film thicknesses for both polarizations, showing saturation towards higher wavelength. We surmise that in order to maximize absorption enhancement for a given wavelength, the thickness of a thin silicon film had better be chosen to the maxima of the oscillations in Fig. 12. Therefore based on this normal incidence analysis, when designing a device the thickness of the silicon film had better be tweaked from  $L_{Si} = 2400$  nm to one of the fringe maxima in Fig. 12, such as  $L_{Si} = 1200$  nm or the range  $1800 - 2100$  nm.

### C. Other experimental considerations

To enhance the absorption of light over an even broader wavelength range than reported here, it is relevant to consider different orientations of the 3D photonic crystal back reflector. In case of both direct and inverse woodpile structures, it is interesting to consider light incident in the  $\Gamma Y$  direction, since the  $\Gamma Y$  stop gap with a relative

bandwidth 39.1 % (see Fig. 2 of Ref. [50]) is about  $1.3\times$  broader than the  $\Gamma Z$  or  $\Gamma X$  stop gaps whose relative bandwidth is 30.4 % [50, 51, 63, 64].

To improve the likelihood that photonic band gap back reflectors gain real traction, it is obviously relevant to consider strategies whereby such a back reflector can be realized over as large as possible (X,Y) areas. In the current nanofabrication of silicon inverse woodpiles, an important limitation is the depth of the nanopores that are fabricated by deep reactive-ion etching [55, 65], which limits the X- or Z-extent of the nanostructures, whereas the Y-extent has no fundamental limit. Therefore, with the design shown in Fig. 2, the back reflector would have sufficient Z-extent (thickness) and a large Y-extent, but limited X-extent, and thus limited area. A remedy consists of etching the nanopores at  $45^\circ$  to the back surface, as demonstrated by Takahashi *et al.* [86]. Then, the areal (X,Y)-extent of the photonic crystal equals the areal extent of the pore array, which can be defined by standard optical lithography or by self-assembly. In such a design, light at normal incidence to the thin silicon film arrives at  $45^\circ$  with respect to the inverse woodpile structure, parallel to the  $\Gamma U$  high-symmetry direction. The stop gap for this high-symmetry direction has properties that are fairly similar to the  $\Gamma Z$  or  $\Gamma X$  stop gaps considered here [50, 51, 63, 64]. Therefore, the present analysis also pertains to this design.

Having a 3D silicon photonic crystal as a back reflector provides an all-silicon integration with the absorbing thin silicon film. Moreover, this approach makes the thin film device lighter, since the 3D inverse woodpile photonic crystal structure is highly porous, consisting of nearly 80% volume fraction air (see Appendix A). Simultaneously, our design remarkably enhances the overall absorption in comparison to a standalone thin silicon film with the same overall thickness, as illustrated by our results.

If one wishes to shift the absorption enhancements discussed here to shorter wavelengths, it is relevant to consider replacing silicon by wider band gap semiconductors such as GaAs, GaP, or GaN. In such a case, an important practical consideration is whether to realize the photonic band gap back reflector from the same semiconductor for convenient integration, or whether to perform heterogeneous integration of silicon photonic band gap crystals, since the latter are readily realizable, see Refs. [55, 65, 71, 72].

Since GaAs has a similar real refractive index as silicon, many of the results presented here can be exploited to make predictions for GaAs absorption in presence of a photonic band gap back reflector. For the other semiconductors, this calls for additional detailed calculations, since most semiconductors have different (complex) refractive indices than silicon, with different dispersion. Nevertheless, the computational concepts and strategies presented in our study remain relevant to address the pertinent questions.

To obtain an interpretation of Fig. 3 and Fig. 4 for photovoltaics where incident light is unpolarized, one can take the mean absorption enhancements  $\eta'_{abs}(\lambda)$  for  $s$  polarization and  $p$  polarization. As mentioned earlier, for the sake of physical understanding our computations pertain to a flat top surface of the thin silicon film without anti-reflection coating. On the other hand, it is well known that a substantial improvement in light harvesting is obtained by applying anti-reflection coatings and by tailoring the shape of top surface, for instance, a random Lambertian-like surface. Therefore, a logical research step is to combine a photonic band gap back reflector with suitable top-surface engineering, even though it is likely that this situation substantially complicates both the numerical setup and the numerical convergence.

## V. CONCLUSION

We investigated a thin 3D photonic band gap crystal as a back reflector in the visible regime, which reflects light within the band gap for all directions and for all polarizations. The absorption spectra of a thin silicon film with a 3D inverse woodpile photonic crystal back reflector were calculated using finite-element computations of the 3D time-harmonic Maxwell equations. We tailored the finite-sized inverse woodpile crystal design to have a broad photonic band gap in the visible range and have used the refractive index of the real silicon, including dispersion and absorption, in order to make our calculations relevant to experiments. From the comparison of the photonic crystal back reflector to a perfect metallic back reflector, we infer that a photonic crystal back reflector increases the number of Fabry-Pérot fringes for a thin silicon film. Therefore, we observe that a 3D inverse woodpile photonic crystal enhances the absorption of a thin silicon film by (i) behaving as a perfect reflector, exhibiting nearly 100% reflectivity in the stop bands, as well as (ii) generating guided modes at many discrete wavelengths. Our absorption results show nearly  $2.39\times$  enhanced wavelength-, angle-, polarization-averaged absorption between  $\lambda = 680$  nm and  $\lambda = 880$  nm compared to a 2400 nm thin silicon film. We find that the absorption enhancement is enhanced by positioning an inverse woodpile back reflector at the back end of a thin silicon film, which will keep the length of the thin film device unchanged as well as make it lighter. In order to maximize the efficiency for a given wavelength, we show that the thickness of a thin silicon film had better be chosen to the maxima of the Fabry-Pérot fringes. For a sub-wavelength ultrathin 80 nm absorbing layer with a photonic crystal back reflector, we identify and demonstrate two physical mechanisms causing the giant average absorption enhancement of  $9.15\times$  : (i) guided modes due to the



Bragg attenuation length and (ii) confinement due to a surface defect.

## VI. FUNDING

This research is supported by the Shell-NWO/FOM programme “Computational Sciences for Energy Research” (CSER), NWO-FOM program nr. 138 “Stirring of light!,” NWO-TTW Perspectief program P15-36 “Free-form scattering optics” (FFSO), NWO ENW-GROOT program (OCENW.GROOT.2019.071) ”Self-assembled icosahedral photonic quasicrystals with a band gap for visible light”, the “Descartes-Huygens” prize of the French Academy of Sciences (with support from JMG), and the MESA<sup>+</sup> Institute section Applied Nanophotonics (ANP).

## VII. ACKNOWLEDGMENTS

It is a great pleasure to thank Bill Barnes (Exeter and Twente), Ad Lagendijk, Allard Mosk (Utrecht University), Oluwafemi Ojambati, Pepijn Pinkse, and Ravitej Uppu (now at University of Iowa) for stimulating discussions, Diana Grishina for logistic support, and Femius Koenderink (now at AMOLF, Amsterdam) for the analytical expression of the volume fraction in the early days when we had just started developing silicon inverse woodpile photonic band gap crystals. We thank two anonymous reviewers for their very helpful suggestions.

## VIII. DISCLOSURES

The authors declare no conflicts of interest.

## IX. DATA AVAILABILITY

Data underlying the results presented in this paper are not publicly available at this time but may be obtained from the authors upon reasonable request.

### Appendix A: Primitive unit cell of the 3D inverse woodpile photonic crystal structure

For a cubic inverse woodpile with lattice parameters  $c$  and  $a$ , Fig. 13 (i) shows the tetragonal primitive unit cell for reduced nanopore radii  $\frac{r_1}{a} = 0.245$ . This unit cell is periodic in all three directions X, Y, Z. If the air volume fraction is further increased by increasing the nanopore radii, Fig. 13 (ii) reveals remarkable crescent-like shapes appearing at the front and the back interfaces in the XY view of the unit cell, here for reduced pore radii  $\frac{r_1}{a} = 0.275$ . Once the pore radii exceed  $\frac{r_1}{a} \geq 0.245$ , the adjacent pores intersect with each other and hence these crescent-like shapes occur as they preserve the periodicity of the unit cell.

Figure 13 (bottom) shows the calculated volume fraction of air and silicon in the inverse woodpile crystal structure versus the reduced nanopore radius  $\frac{r_1}{a}$  by employing a volume integration routine of the finite element method [66]. To preserve periodicity of the numerically approximated unit cell, we consider the primitive unit cell in (i) for a pore radius between  $\frac{r_1}{a} = 0$  and  $\frac{r_1}{a} = 0.245$  and the modified unit cell in (ii) for a pore radius between  $\frac{r_1}{a} = 0.245$  and  $\frac{r_1}{a} = 0.30$ . Our numerical calculation agrees to great precision (within about 10<sup>-6</sup>%) with the analytical results for all pore radii. Since an inverse woodpile crystal consists of nearly 80% air by volume fraction at the optimal pore radius  $\frac{r_1}{a} = 0.245$ , it is a very lightweight component for light-absorbing high-tech devices (including photovoltaics), in comparison to bulk silicon with the same thickness.

### Appendix B: Brillouin zone of the 3D inverse woodpile photonic crystal structure

Figure 14 shows the first Brillouin zone of the inverse-woodpile crystal structure in the representation with a tetragonal unit cell, with real space lattice parameters  $(a, c, a)$ , and reciprocal space lattice parameters  $(2\pi/a, 2\pi/c, 2\pi/a)$ . Eight high symmetry points are shown, where  $\Gamma$  corresponds to coordinates  $(0,0,0)$ , X to  $(1/2, 0, 0)$ , Y to  $(0, 1/2, 0)$ , and Z to  $(0, 0, 1/2)$ . The X and Z directions correspond to the directions parallel to the two sets of nanopores in the crystal structure, that turn out to be symmetry equivalent, see Refs. [50, 51].

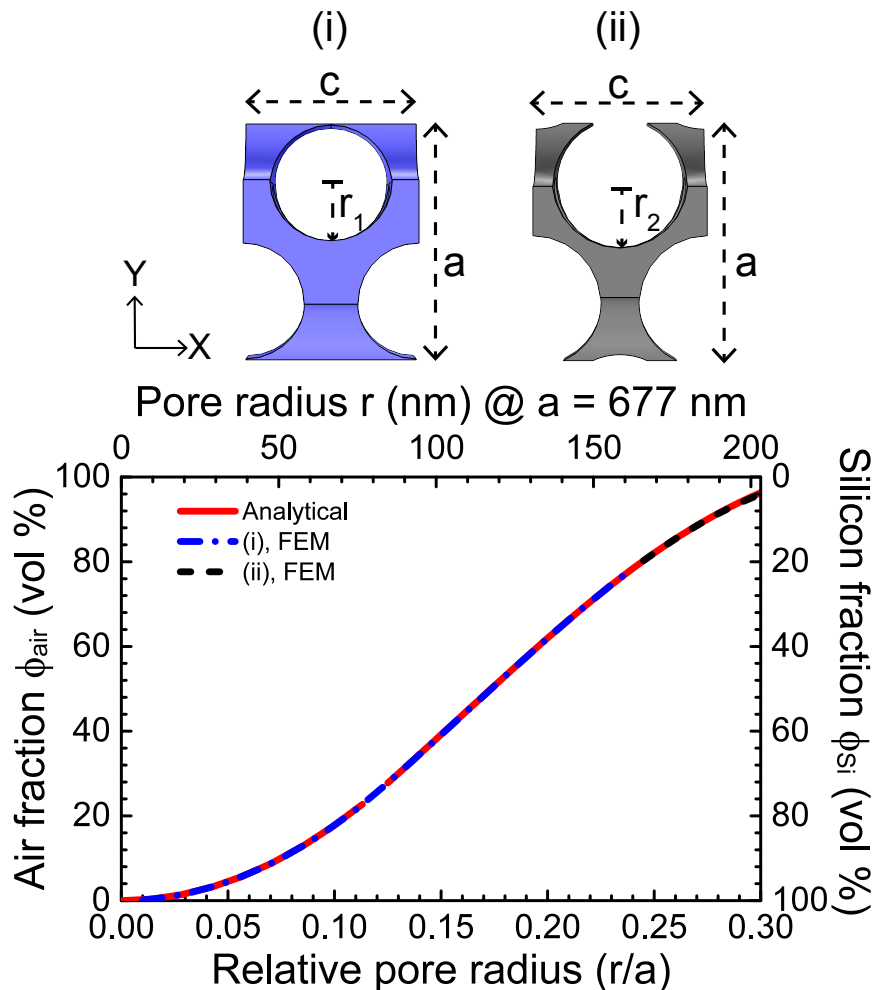


FIG. 13: Top: (i) The tetragonal primitive unit cell of the cubic inverse woodpile photonic crystal structure along the Z axis with lattice parameters  $c$  and  $a$  and the pore radius  $\frac{r_1}{a} = 0.245$ , (ii) unit cell adapted to a larger pore radius  $\frac{r_2}{a} = 0.275$ . The blue and black colors in (i) and (ii), respectively, indicate the high-index backbone of the crystal. The white color represents air. Bottom: Volume fraction of air in the 3D inverse woodpile photonic crystal versus the relative pore radius  $\frac{r}{a}$ . The blue dashed-dotted curve indicates the numerical result for a pore radius between  $\frac{r}{a} = 0$  and  $\frac{r}{a} = 0.245$  using the primitive unit cell in (i). The black dashed curve indicates the numerical result for a pore radius between  $\frac{r}{a} = 0.245$  and  $\frac{r}{a} = 0.30$  using the modified unit cell in (ii). The red solid curve represents previously unpublished analytical results by Femius Koenderink (2001).

### Appendix C: Complex and dispersive refractive index of silicon

To make our study relevant to practical devices, we employ the dispersive and complex refractive index obtained from experiments to model silicon in all thin films and in the photonic crystal backbone. Figure 15 shows the wavelength dependency of the real and imaginary parts of the refractive index of silicon in the visible regime from several sources [61, 87, 88]. Vuye *et al.* report the dielectric function of a commercially available silicon wafer using *in situ* spectroscopic ellipsometry [87]. Jellison measured the dielectric function of crystalline silicon using two-channel polarization modulation ellipsometry [88], and Green gives a tabulation of the optical properties of intrinsic silicon based on many different sources, aiming at solar cell calculations [61]. Figure 15 shows that for the real part of the refractive indices of Refs. [87], [88], and [61] are in very good mutual agreement, and are thus used in our simulations. For the imaginary part of the refractive index, we note that the results of Ref. [88] and [61] agree well with each other between  $\lambda = 500$  nm and 750 nm and differ from the ones from Ref. [87] for reasons unknown to us. All data sets agree well beyond  $\lambda = 750$  nm. Since Ref. [61] is based on many different sources of data, we have chosen to adopt it

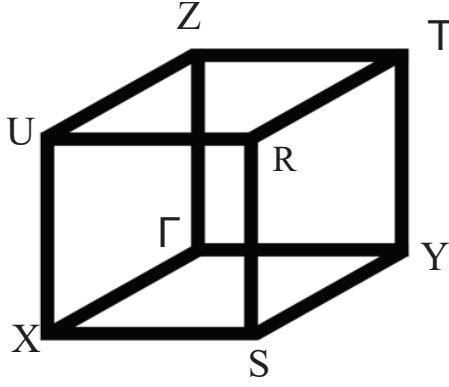


FIG. 14: First Brillouin zone of the inverse-woodpile crystal structure in the tetragonal representation showing the high-symmetry points (Roman symbols) and the origin at  $\Gamma$ .

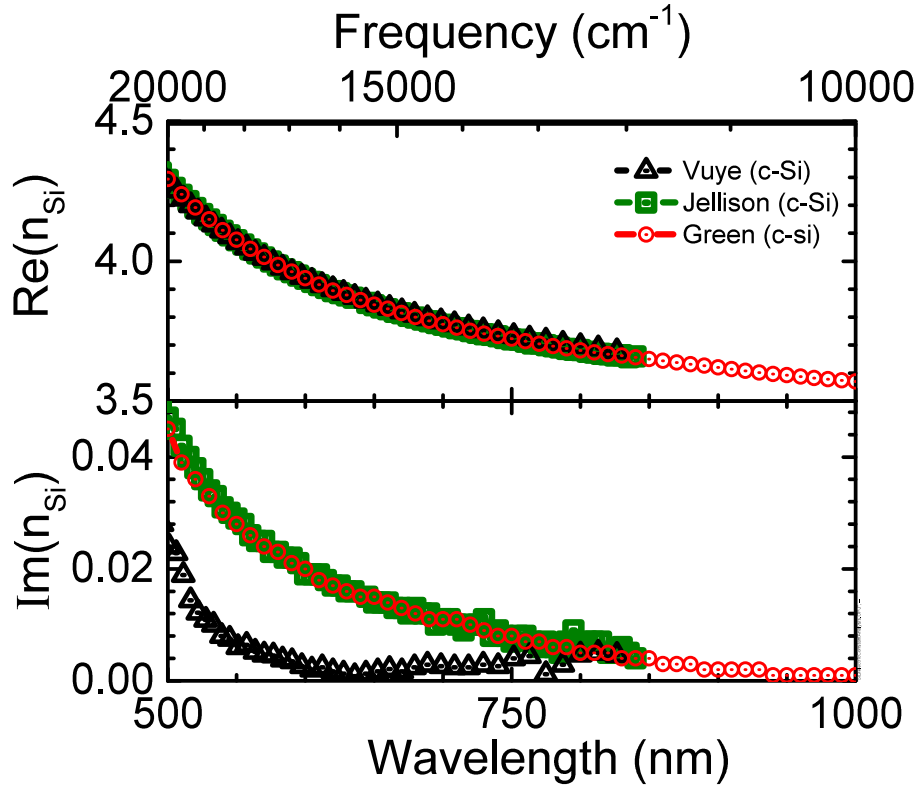


FIG. 15: Wavelength dependence of the real and imaginary parts of the refractive index of crystalline silicon (c-Si) in the visible and near infrared spectral ranges. Red circles, black triangles, and green squares are the data obtained from Ref. [61], Ref. [87], and Ref. [88], respectively. The top ordinate shows the frequency in wave numbers ( $\text{cm}^{-1}$ ).

as the imaginary refractive index of silicon in our study.

To assess the impact of adding doped layer, a doping level of  $10^{16} \text{ cm}^{-3}$  already gives substantial mobility. Fortunately, from the well-known semiconductor data collection of the Ioffe Institute ("SVM") we find that this doping level yields a very small change in optical properties ( $\text{Re}(n_{\text{Si}})$ ,  $\text{Im}(n_{\text{Si}})$ ). Hence, the variation of intrinsic absorption versus doping level is below 1% [89], and thus for practical purposes negligible.

$J_{PBG}$ (mA/cm <sup>2</sup> )	$s$ -stop band ( $\lambda_{up} = 640$ nm to $\lambda_{low} = 890$ nm)	$p$ -stop band ( $\lambda_{up} = 650$ nm to $\lambda_{low} = 870$ nm)
$L_{Si} = 80$ nm Si only	0.2244	0.1901
$L_{Si} = 80$ nm Si + perfect metal	0.1728	0.1544
$L_{Si} = 80$ nm Si + 3D photonic crystal	2.9442	2.0362
$L_{Si} = 80$ nm Si, Lambertian scattering	6.1607	5.5523

TABLE I: Photonic band gap generated current density  $J_{PBG}$  computed using Eq. D1 for different ultrathin silicon film devices: thin film only, with a perfect metal back reflector, with a 3D photonic band gap back reflector, and with Lambertian scattering.

$J_{PBG}$ (mA/cm <sup>2</sup> )	$s$ -stop band ( $\lambda_{up} = 640$ nm to $\lambda_{low} = 890$ nm)	$p$ -stop band ( $\lambda_{up} = 650$ nm to $\lambda_{low} = 870$ nm)
$L_{Si} = 2400$ nm Si only	4.1635	3.6452
$L_{Si} = 3600$ nm Si only	5.1025	4.7038
$L_{Si} = 2400$ nm + 1200 nm 3D photonic crystal	9.2394	8.9276
$L_{Si} = 2400$ nm, Lambertian scattering	16.2197	14.4055
$L_{Si} = 3600$ nm Si, Lambertian scattering	16.6290	14.7370

TABLE II: Photonic band gap generated current density  $J_{PBG}$  calculated using Eq. D1 at normal incidence for thin silicon films only ( $L_{Si} = 2400$  nm and  $L_{Si} = 3600$  nm), with a 3D inverse woodpile photonic crystal back reflector, and with Lambertian scattering.

#### Appendix D: Photonic band gap generated current density

In an ideal situation, where one absorbed photon generates one electron-hole pair, it is known from the solar cell literature) that the wavelength-dependent external quantum efficiency  $EQE(\lambda)$  is equal to the absorption  $A_{Si}(\lambda)$  [11, 75]. Hence, we define a current density  $J_{PBG}$  generated by incident light within the photonic band gap (PBG)

$$J_{PBG} \equiv q \int_{\lambda_{up}}^{\lambda_{low}} EQE(\lambda) P_{AM1.5}(\lambda) d\lambda, \quad (D1)$$

where  $\lambda_{low}$  is the wavelength corresponding to the lower band edge of the band gap,  $\lambda_{up}$  the wavelength corresponding to the upper band edge of the band gap. In other words, Eq. D1 is an integral of the absorption spectrum weighted with the solar spectrum of incident photons.

Tables I and II show the photonic band gap generated current density  $J_{PBG}$  for normal incidence (Eq. D1) for both the supra-wavelength  $L_{Si} = 2400$  nm thin and sub-wavelength  $L_{Si} = 80$  nm ultrathin silicon films, and with and without various back reflectors. Table I shows that the perfect metal back reflector does not increase the photonic band gap generated current density  $J_{PBG}$  for an ultrathin film thickness much less than the wavelength in the material ( $L_{Si} \ll \lambda/n$ ). This result confirms our observation in Sec. III B that a perfect metal hardly enhances absorption for films with thicknesses corresponding to a Fabry-Pérot minimum for the desired wavelengths of enhancement.

In presence of a 3D photonic band gap back reflector, the photonic band gap generated current density  $J_{PBG}$  for the  $L_{Si} = 80$  nm ultrathin film increases nearly  $13\times$  for the  $s$ -polarized stop band and  $10\times$  for the  $p$ -polarized stop band, which supports the absorption enhancements observed for 3D photonic crystal back reflector in Sec. III A. Moreover, similar to absorption enhancement results in Sec. III B the 3D photonic band gap back reflector also increases the photonic band gap generated current density  $J_{PBG}$  for a  $L_{Si} = 2400$  nm thin film by nearly  $2.21\times$  for  $s$ -stop band and  $2.45\times$  for  $p$ -stop band (Table II). Finally, our computation in Table II supports the use of a photonic crystal back reflector by increasing the photonic band gap generated current density  $J_{PBG}$  by  $1.81\times$  for  $s$ -stop band and  $1.9\times$  for  $p$ -stop band even compared to a  $L_{Si} = 3600$  nm thin film (similar to absorption discussion in Sec. III D).

On the other hand, both Table I and Table II show that the photonic band gap generated current density  $J_{PBG}$  with a photonic crystal back reflector is still nearly  $2 - 2.5\times$  lower than the one computed for Lambertian scattering. This difference is attributed to the fact that absorption due to Lambertian scattering also assumes a perfect anti-reflection front coating, unlike our present computations, see Fig 2.

---

[1] J. W. Orton, “The story of semiconductors,” (Oxford University, 2004).

- [2] D. A. B. Miller, "Device Requirements for Optical Interconnects to Silicon Chips," *Proc. IEEE* **97**, 1166 (2009).
- [3] G. T. Reed, G. Mashanovich, F. Y. Gardes, and D. J. Thomson, "Silicon optical modulators," *Nature Photon.* **4**, 518 (2010).
- [4] P. W. Coteus, J. U. Knickerbocker, C. H. Lam, and Y. A. Vlasov, "Technologies for exascale systems," *IBM J. Res. Dev.* **55**, 14 (2011).
- [5] M. K. Smit, J. J. G. M. van der Tol, and M. T. Hill, "Moore's law in photonics," *Laser Photonics Rev.* **6**, 1 (2012).
- [6] Y. A. Vlasov, "Silicon CMOS-integrated nano-photonics for computer and data communications beyond 100G," *IEEE Commun. Mag.* **50**, S67 (2012).
- [7] V. M. Delmotte, P. Zhai, A. Pirani, S. L. Connors, C. Péan, S. Berger, N. Caud, Y. Chen, L. Goldfarb, M. I. Gomis, M. Huang, K. Leitzell, E. Lonnoy, J. B. R. Matthews, T. K. Maycock, T. Waterfield, O. Yelekçi, R. Yu, and B. Zhou, "2021: *Climate Change 2021: The Physical Science Basis. Contribution of Working Group I to the Sixth Assessment Report of the Intergovernmental Panel on Climate Change*" (Cambridge University, 2021, In Press).
- [8] A. Rohatgi, E. Weber, and L. C. Kimerling, "Opportunities in silicon photovoltaics and defect control in photovoltaic materials," *J. Electron. Mater.* **22**, 65 (1993).
- [9] International Energy Agency (IEA), "Solar PV Analysis," <https://www.iea.org/reports/solar-pv> (accessed 29 Sept. 2020).
- [10] A. L. Fahrenbruch and R. H. Bube, "Fundamentals in Solar Cells" (Academic, 1983).
- [11] A. Luque and S. Hegedus, Editors, "Handbook of photovoltaic science and engineering" (John Wiley and Sons Ltd, 2011, 2nd Edition).
- [12] "Symposium: Forty years of light management," 2021 OSA Advanced Photonics Congress [https://www.osa.org/en-us/meetings/osa\\_meetings/advanced\\_photonics\\_congress/program/symposia/#Forty](https://www.osa.org/en-us/meetings/osa_meetings/advanced_photonics_congress/program/symposia/#Forty).
- [13] A. G. Aberle and P. I. Widenborg, "Crystalline Silicon Thin-Film Solar Cells via High-Temperature and Intermediate-Temperature Approaches," in Ref. [11], Chapter 11, pp. 452-486.
- [14] ASTM G173-03, "Standard tables for reference solar spectral irradiances: direct normal and hemispherical on 37 degree tilted surface," (ASTM International, West Conshohocken, Pennsylvania, 2005).
- [15] C. Herzinger, B. Johs, W. McGahan, J. Woollam, and W. Paulson, "Ellipsometric determination of optical constants for silicon and thermally grown silicon dioxide via a multi-sample, multi-wavelength, multi-angle investigation," *J. Appl. Phys.* **83**, 3323 (1998).
- [16] P. Sheng, A. N. Bloch, and R. S. Stepleman, "Wavelength-selective absorption enhancement in thin-film solar cells," *Appl. Phys. Lett.* **43**, 579 (1983).
- [17] T. Tiedje, E. Yablonovitch, G. D. Cody, and B. G. Brooks, "Limiting efficiency of silicon solar cells," *IEEE Trans. Electron Devices* **31**, 711 (1984).
- [18] A. Richter, M. Hermle, and S. W. Glunz, "Reassessment of the Limiting Efficiency for Crystalline Silicon Solar Cells," *IEEE Journal of Photovoltaics* **3**, 1184 (2013).
- [19] M. A. Green, K. Emery, Y. Hishikawa, W. Warta, and E. D. Dunlop, "Solar cell efficiency tables (Version 45)," *Prog. Photovolt.* **20**, 606 (2012).
- [20] K. Münzer, K. T. Holdermann, R. E. Schlosser, and S. Sterk, "Thin monocrystalline silicon solar cells," *IEEE Trans. Electron Devices* **46**, 2055 (1999).
- [21] A. V. Shah, H. Schade, M. Vanecek, J. Meier, E. Vallat-Sauvain, N. Wyrsh, U. Kroll, C. Droz, and J. Bailat, "Thin-film silicon solar cell technology," *Prog. Photovolt.* **12**, 113 (2004).
- [22] Z. Yu, A. Raman, and S. Fan, "Fundamental limit of nanophotonic light trapping in solar cells," *Proc. Natl. Acad. Sci. U.S.A.* **2010**, 17491 (2010).
- [23] N.-N. Feng, J. Michel, L. Zeng, J. Lie, C.-Y. Hong, L. C. Kimerling, and X. Duan, "Design of highly efficient light-trapping structures for thin-film crystalline silicon solar cells," *IEEE Trans. Electron Devices* **54**, 1926 (2007).
- [24] L. C. Andreani, A. Bozzola, P. Kowalczewski, M. Liscidini, and L. Redorici, "Silicon solar cells: toward the efficiency limits," *Adv. Phys.-X* **4**, 1548305 (2019).
- [25] R. Saive, "Light trapping in thin silicon solar cells: A review on fundamentals and technologies," *Prog. Photovolt. Res. Appl.* DOI: 10.1002/pp.3440 (2021).
- [26] E. Yablonovitch and G. Cody, "Intensity enhancement in textured optical sheets for solar cells," *IEEE Trans. Electron Devices* **29**, 300 (1982).
- [27] E. Moulin, U. W. Paetzold, H. Siekmann, J. Worbs, A. Bauer, and R. Carius, "Study of thin-film silicon solar cell back reflectors and potential of detached reflectors," *Energy Procedia* **10**, 106 (2011).
- [28] R. Brendel, M. Hirsch, R. Plieninger, and J. Werner, "Quantum efficiency analysis of thin-layer silicon solar cells with back surface fields and optical confinement," *IEEE Trans. Electron Devices* **43**, 1104 (1996).
- [29] Y. Fink, J. N. Winn, S. Fan, C. Chen, J. Michel, J. D. Joannopoulos, and E. L. Thomas, "A dielectric omnidirectional reflector," *Science* **282**, 1679-1682 (1998).
- [30] D. J. Griffiths, "Introduction to electrodynamics," (Prentice Hall, 1999).
- [31] S. John, "Electromagnetic Absorption in a Disordered Medium near a Photon Mobility Edge," *Phys. Rev. Lett.* **53**, 2169 (1984).
- [32] O. L. Muskens, J. G. Rivas, R. E. Algra, E. P. A. M. Bakkers, and A. Lagendijk, "Design of light scattering in nanowire materials for photovoltaic applications," *Nano Lett.* **8**, 2638 (2008).
- [33] W. Wang, S. Wu, K. Reinhardt, Y. Lu, and S. Chen, "Broadband light absorption enhancement in thin-film silicon solar cells," *Nano Lett.* **10**, 2012 (2010).
- [34] A. Polman and H. A. Atwater, "Photonic design principles for ultrahigh-efficiency photovoltaics," *Nat. Mater.* **11**, 174

- (2012).
- [35] M. Brongersma, Y. Cui, and S. Fan, "Light management for photovoltaics using high-index nanostructures," *Nat. Mater.* **13**, 451 (2014).
- [36] S. Nishimura, N. Abrams, B. A. Lewis, L. I. Halaoui, T. E. Mallouk, K. D. Benkstein, J. van de Lagemaat, and A. J. Frank, "Standing wave enhancement of red absorbance and photocurrent in dye-sensitized titanium dioxide photoelectrodes coupled to photonic crystals," *J. Am. Chem. Soc.* **125**, 6306 (2003).
- [37] A. Mihi and H. Miguez, "Origin of light-harvesting enhancement in colloidal-photonic-crystal-based dye-sensitized solar cells," *J. Phys. Chem. B* **109**, 15968 (2005).
- [38] S. Colodrero, A. Mihi, L. Häggman, M. Ócana, G. Boschloo, A. Hagfeldt, and H. Miguez, "Porous one-dimensional photonic crystals improve the power-conversion efficiency of dye-sensitized solar cells," *Adv. Mater.* **21**, 764 (2009).
- [39] M. S. Branham, W.-C. Hsu, S. Yerci, J. Loomis, S. V. Boriskina, "15.7% efficient 10- $\mu$ -thick crystalline silicon solar cells using periodic nanostructures," *Adv. Mater.* **27**, 2182 (2015).
- [40] W.-C. Hsu, J. K. Tong, M. S. Branham, Y. Huang, S. Yerci, S. V. Boriskina, G. Chen, "Mismatched front and back gratings for optimum light trapping in ultra-thin crystalline silicon solar cells," *Opt. Commun.* **377**, 52 (2016).
- [41] P. Bermel, C. Luo, L. Zeng, L. C. Kimerling, and J. D. Joannopoulos, "Improving thin-film crystalline silicon solar cell efficiencies with photonic crystals," *Opt. Express* **15**, 25 (2007).
- [42] P. G. O'Brien, N. P. Kherani, A. Chutinan, G. A. Ozin, S. John, and S. Zukotynski, "Silicon photovoltaics using conducting photonic crystal back-reflector," *Adv. Mater.* **20**, 1577 (2008).
- [43] B. Curtin, R. Biswas, and V. Dalal, "Photonic crystal based back reflectors for light management and enhanced absorption in amorphous silicon solar cells," *Appl. Phys. Lett.* **95**, 231102 (2009).
- [44] L. Zeng, P. Bermel, B. A. Alamariu, K. A. Broderick, J. Liu, X. Duan, J. Joannopoulos, and L. C. Kimerling, "Demonstration of enhanced absorption in thin film Si solar cells with textured photonic crystal back reflector," *Appl. Phys. Lett.* **93**, 221105 (2008).
- [45] R. Biswas, J. Bhattacharya, B. Lewis, N. Chakravarty, and V. Dalal, "Enhanced nanocrystalline silicon solar cell with a photonic crystal back-reflector," *Sol. Energy Mat. Sol. Cells* **94**, 2337 (2010).
- [46] R. B. Wehrspohn and J. Üpping, "3D photonic crystals for photon management in solar cells," *J. Opt.* **14**, 024003 (2012).
- [47] A. N. Sprafke, D. Schneevoigt, S. Seidel, S. L. Schweizer, and R. B. Wehrspohn, "Automated spray coating process for the fabrication of large-area artificial opals on textured substrates," *Opt. Express* **21**, A528-A538 (2013).
- [48] K. Ishizaki, M. D. Zoysa, Y. Tanaka, S.-W. Jeon, and S. Noda, "Progress in thin-film silicon solar cells based on photonic-crystal structure," *J. Appl. Phys.* **57**, 060101 (2018).
- [49] J. D. Joannopoulos, S. G. Johnson, J. N. Winn, and R. D. Meade, "Photonic crystals: Molding the flow of light," (Princeton University, 2008).
- [50] D. Devashish, S. B. Hasan, J. J. W. van der Vegt, and W. L. Vos, "Reflectivity calculated for a three-dimensional silicon photonic band gap crystal with finite support," *Phys. Rev. B* **95**, 155141 (2017).
- [51] S. R. Huisman, R. V. Nair, L. A. Woldering, M. D. Leistikow, A. P. Mosk, and W. L. Vos, "Signature of a three-dimensional photonic band gap observed with silicon inverse woodpile photonic crystals," *Phys. Rev. B* **83**, 205313 (2011).
- [52] M. D. Leistikow, A. P. Mosk, E. Yeganegi, S. R. Huisman, A. Lagendijk, and W. L. Vos, "Inhibited spontaneous emission of quantum dots observed in a 3D photonic band gap," *Phys. Rev. Lett.* **107**, 193903 (2011).
- [53] E. Yeganegi, A. Lagendijk, A. P. Mosk, and W. L. Vos, "Local density of optical states in the band gap of a finite one-dimensional photonic crystal," *Phys. Rev. B* **89**, 045123 (2014).
- [54] S. B. Hasan, A. P. Mosk, W. L. Vos, and A. Lagendijk, "Finite-size Scaling of the Density of States in Photonic Band Gap Crystals," *Phys. Rev. Lett.* **120**, 237402 (2018).
- [55] D. A. Grishina, C. A. M. Hartevelde, A. Pacureanu, D. Devashish, A. Lagendijk, P. Cloetens, and W. L. Vos, "X-ray Imaging of Functional Three-Dimensional Nanostructures on Massive Substrates," *ACS Nano* **13**, 13932 (2019).
- [56] M. Adhikary, R. Uppu, C. A. M. Hartevelde, D. A. Grishina, and W. L. Vos, "Experimental probe of a complete 3D photonic band gap," *Opt. Express* **28**, 2684 (2020).
- [57] T. Tajiri, S. Takahashi, C. A. M. Hartevelde, Y. Arakawa, S. Iwamoto, and W. L. Vos, "Reflectivity of three-dimensional GaAs photonic band-gap crystals of finite thickness," *Phys. Rev. B* **101**, 235303 (2020).
- [58] C. P. Mavidis, A. C. Tasolamprou, S. B. Hasan, T. Koschny, E. N. Economou, M. Kafesaki, C. M. Soukoulis, and W. L. Vos, "Local density of optical states in the three-dimensional band gap of a finite photonic crystal," *Phys. Rev. B* **101**, 235309 (2020).
- [59] D. Devashish, O. S. Ojambati, S. B. Hasan, J. J. W. van der Vegt, and W. L. Vos, "Three-dimensional photonic band gap cavity with finite support: Enhanced energy density and optical absorption," *Phys. Rev. B* **99**, 075112 (2019).
- [60] S. A. Hack, J. J. W. van der Vegt, and W. L. Vos, "Cartesian light: Unconventional propagation of light in a three-dimensional superlattice of coupled cavities within a three-dimensional photonic band gap," *Phys. Rev. B* **99**, 115308 (2019).
- [61] M. A. Green, "Self-consistent optical parameters of intrinsic silicon at 300K including temperature coefficient," *Sol. Energy Mat. Sol. Cells* **92**, 1305 (2008).
- [62] K. M. Ho, C. T. Chan, C. M. Soukoulis, R. Biswas, and M. Sigalas, "Photonic band gaps in three dimensions: new layer-by-layer periodic structures," *Solid State Commun.* **89**, 413 (1994).
- [63] R. Hillebrand, S. Senz, W. Hergert, and U. Gösele, "Macroporous-silicon-based three-dimensional photonic crystal with a large complete band gap," *J. Appl. Phys.* **94**, 2758 (2003).
- [64] L. A. Woldering, A. P. Mosk, R. W. Tjerkstra, and W. L. Vos, "The influence of fabrication deviations on the photonic

- band gap of three-dimensional inverse woodpile nanostructures,” J. Appl. Phys. **105**, 093108 (2009).
- [65] J. M. van den Broek, L. A. Woldering, R. W. Tjerkstra, F. B. Segerink, I. D. Setija, and W. L. Vos, “Inverse-woodpile photonic band gap crystals with a cubic diamond-like structure made from single-crystalline silicon,” Adv. Funct. Mater. **22**, 25 (2012).
- [66] “COMSOL Multiphysics® v. 5.2. www.comsol.com, COMSOL AB, Stockholm, Sweden”.
- [67] J. M. Jin, “*The finite element method in electromagnetics*” (Wiley-IEEE, 2000).
- [68] Since the air layer and the thin silicon film are homogeneous media, an upper limit  $\Delta l \leq \frac{\lambda_0}{8}$  is imposed on the edge length  $\Delta l$  of any tetrahedron in these layers, with  $\lambda_0$  the shortest wavelength of the incident plane waves in vacuum. Since an inverse woodpile crystal contains many sharp and curved interfaces between the high-index backbone and the low-index medium, an upper limit  $\Delta l \leq \frac{\lambda_0}{8 \cdot \max(n_{Si})}$  is imposed on the edge length  $\Delta l$  of any tetrahedron inside the photonic crystal (as well as a sub-wavelength thin silicon film  $L_{Si} = 80$  nm), where  $\max(n_{Si})$  is the maximum silicon refractive index in the relevant spectral range.
- [69] “Serendipity” is a high performance computing cluster whose main features are 16 Dell Power edge R430 servers with each 2x Intel Xeon E5-2698 processors at 2.2GHz, with in total 640 cores and about 3.6 terabyte memory, connected through Infiniband. The head node is a Dell Power Edge R730.
- [70] R. Uppu, M. Adhikary, C. A. M. Harteveld, and W. L. Vos, “Spatially shaping waves to penetrate deep inside a forbidden gap,” Phys. Rev. Lett. **126**, 177402 (2021).
- [71] R. W. Tjerkstra, L. A. Woldering, J. M. van den Broek, F. Roozeboom, I. D. Setija, and W. L. Vos, “Method to pattern etch masks in two inclined planes for three-dimensional nano- and microfabrication,” J. Vac. Sci. Technol. B **29**, 061604 (2011).
- [72] D. A. Grishina, C. A. M. Harteveld, L. A. Woldering, and W. L. Vos, “Method for making a single-step etch mask for 3D monolithic nanostructures,” Nanotechnology **26**, 505302 (2015).
- [73] E. Yablonovitch, “Statistical ray optics,” J. Opt. Soc. Am. **72**, 899 (1982).
- [74] M. A. Green, “Lambertian Light Trapping in Textured Solar Cells and Light-Emitting Diodes: Analytical Solutions,” Prog. Photovolt: Res. Appl. **10** 235 (2002).
- [75] I. Massiot, A. Cattoni, and S. Collin, “Progress and prospects for ultrathin solar cells,” Nat. Energy **5**, 959 (2020).
- [76] W. L. Vos and L. A. Woldering, Edited by M. Ghulinyan and L. Pavesi, “*Light Localisation and Lasing: Random and Pseudorandom Photonic Structures*” (Cambridge University, 2015), Chap. 8, pp. 180-214, also available from <http://arxiv.org/abs/1504.06803>.
- [77] W. L. Vos, H. M. van Driel, M. Megens, A. F. Koenderink, and A. Imhof, “Experimental probes of the optical properties of photonic crystals,” in Proceedings of the NATO ASI Photonic Crystals and Light Localization in the 21st Century, edited by C. M. Soukoulis (Kluwer, Dordrecht, 2001), pp. 181-198.
- [78] W. L. Vos, R. Sprik, A. van Blaaderen, A. Imhof, A. Lagendijk, and G. H. Wegdam, “Strong effects of photonic band structures on the diffraction of colloidal crystals,” Phys. Rev. B **53**, 24 (1996).
- [79] K. Busch, N. Vats, S. John, and B. C. Sanders, “Radiating dipoles in photonic crystals,” Phys. Rev. E **62**, 4251 (2000).
- [80] S. Fan and J. D. Joannopoulos, “Analysis of guided resonances in photonic crystal slab,” Phys. Rev. B. **65**, 235112 (2002).
- [81] P. Berini, “Long-range surface plasmon polaritons,” Adv. Opt. Photon. **1**, 484 (2009).
- [82] There is an important difference with a LRSPP, namely that here the field is maximal at the center of the thin silicon film, whereas LRSPP fields are minimal at the center of a thin metal film.
- [83] K. Ishizaki and S. Noda, “Manipulation of photons at the surface of three-dimensional photonic crystals,” Nature (London) **46**, 367 (2009).
- [84] A. Yariv and P. Yeh, “*Optical waves in crystals: propagation and control of laser radiation*” (Wiley, 1980), Chapter 6, pp. 155-219.
- [85] Z. Yu and S. Fan, “Angular constraint on light-trapping absorption enhancement in solar cells,” Appl. Phys. Lett. **98**, 011106 (2011).
- [86] S. Takahashi, M. Okano, M. Imada, s. Noda, “Three-dimensional photonic crystals based on double-angled etching and wafer-fusion techniques” Appl. Phys. Lett. **89**, 123106 (2006).
- [87] G. Vuye, S. Fisson, V. Nguyen Van, Y. Wang, J. Rivory, and F. Abelés, “Temperature dependence of the dielectric function of silicon using *in situ* spectroscopic ellipsometry,” Thin Solid Films **233**, 166 (1993).
- [88] G. E. Jellison Jr., “Optical functions of silicon determined by two-channel polarization modulation ellipsometry,” Opt. Mater. **1**, 41 (1992).
- [89] A. A. Wolfson, and V. K. Subashiev, “Intrinsic absorption edge at different doping levels,” Fiz. Tekh. Poluprovodn. **1** 397 (1967) (in Russian).

# Enhanced absorption in thin silicon films by 3D photonic band gap back reflectors for photovoltaics

DEVASHISH SHARMA,<sup>1,2,4</sup> SHAKEEB BIN HASAN,<sup>1,4</sup> REBECCA SAIVE,<sup>3</sup> JAAP J. W. VAN DER VEGT,<sup>2</sup> AND WILLEM L. VOS<sup>1,\*</sup>

<sup>1</sup> *Complex Photonic Systems (COPS), MESA+ Institute for Nanotechnology, University of Twente, P.O. Box 217, 7500 AE Enschede, The Netherlands*

<sup>2</sup> *Mathematics of Computational Science (MACS), MESA+ Institute for Nanotechnology, University of Twente, P.O. Box 217, 7500 AE, Enschede, The Netherlands*

<sup>3</sup> *Inorganic Materials Science (IMS), MESA+ Institute for Nanotechnology, University of Twente, P.O. Box 217, 7500 AE, Enschede, The Netherlands*

<sup>4</sup> *Present address: ASML Netherlands B.V., 5504 DR Veldhoven, The Netherlands*

\* *w.l.vos@utwente.nl, URL: [www.photonicbandgaps.com](http://www.photonicbandgaps.com)*

**Abstract:** Since thin silicon film solar cells have limited optical absorption, we explore the effect of a nanostructured back reflector to recycle the unabsorbed light. As a back reflector, we investigate a three-dimensional (3D) photonic band gap crystal made from silicon that is readily integrated with the thin silicon films. We numerically obtain the optical properties by solving the 3D time-harmonic Maxwell equations using the finite-element method, and model silicon with experimentally determined optical constants. The absorption enhancement [spectra and the short circuit current density](#) are obtained by weighting the absorption spectra with the AM 1.5 standard solar spectrum, as is relevant for photovoltaics. We study thin films in two different regimes, much thicker ( $L_{Si} = 2400$  nm) or much thinner ( $L_{Si} = 80$  nm) than the wavelength of light. At  $L_{Si} = 2400$  nm, the 3D photonic band gap crystal enhances the spectrally averaged ( $\lambda = 680$  nm to 880 nm) silicon absorption by  $2.22\times$  (*s-pol.*) to  $2.45\times$  (*p-pol.*), which exceeds the enhancement of a perfect metal back reflector ( $1.47$  to  $1.56\times$ ). The absorption is considerably enhanced by the (i) broadband angle and polarization-independent reflectivity in the 3D photonic band gap, and (ii) the excitation of many guided modes in the film by the crystal's surface diffraction leading to greatly enhanced path lengths. At  $L_{Si} = 80$  nm, the photonic crystal back reflector yields a striking average absorption enhancement of  $9.15\times$ , much more than  $0.83\times$  for a perfect metal. This enhancement is due to a remarkable guided mode that is confined within the *combined* thickness of the ultrathin film and the photonic crystal's Bragg attenuation length. An important feature of the 3D photonic band gap is to have a broad bandwidth, which leads to the back reflector's Bragg attenuation length being much shorter than the silicon absorption length. Consequently, light is confined inside the thin film and the remarkable absorption enhancements are not due to the additional thickness of the photonic crystal back reflector.

© 2021 Optica Publishing Group under the terms of the [Optica Publishing Group Publishing Agreement](#)

## 1. Introduction

To address the ongoing worldwide climate crisis [1], and provide solar energy for the entire world's population, there is a pressing need to harvest the sun's energy with sustainable solar cells. These cells employ the photovoltaic effect to absorb light and convert the absorbed energy into electricity using semiconductor materials [2, 3]. Being a highly abundant and non-toxic material available in the earth's crust, silicon is an ideal choice to fabricate the many solar cells needed to provide energy to the whole world [4, 5]. While thick silicon solar cells are widely used, thin silicon solar cells are enjoying a rising popularity on account of their obvious sustainability [6], since they require less material and hence less resources and costs [7]. Moreover, they are



46 mechanically flexible so they can be deployed on many different platforms, including freely  
47 shaped ones.

48 Since crystalline silicon (c-Si) has an indirect band gap at 1.1 eV, the absorption of light is low  
49 in the near infrared range that contains 36% of all solar photons [8]. Conversely, the absorption  
50 length is long, namely  $l_a = 1$  mm just above the gap at  $\lambda = 1100$  nm (1.12 eV) and still only  
51  $l_a = 10$   $\mu\text{m}$  at  $\lambda = 800$  nm (1.55 eV) [9]. Since the thickness of thin silicon film solar cells  
52 is much less than the absorption lengths, the absorption of incident solar light is low [10–13],  
53 which adversely affects the cost and the flexibility advantages [14–17].

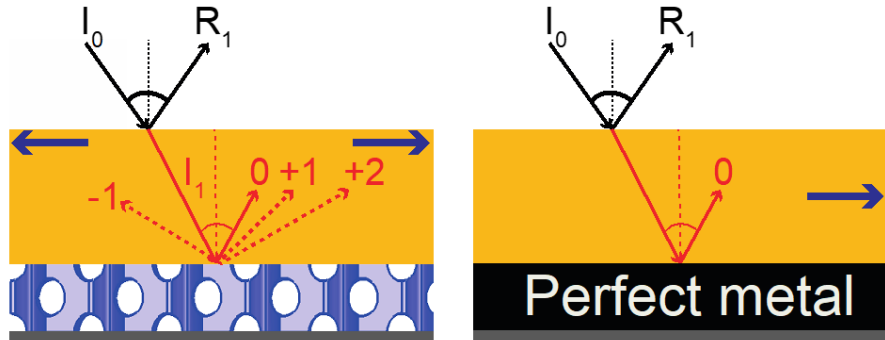


Fig. 1. Design of a thin silicon film (orange) with a 3D photonic band gap crystal (purple, left) and a perfect metal (black, right) as back reflectors. Here, 0 indicates the 0<sup>th</sup> diffraction order that corresponds to specular reflected light by the photonic crystal or the perfect metal.  $I_0$  and  $R_1$  represent the light incident and the first reflection at the front surface of the thin film, respectively.  $I_1$  represents the light refracted into the thin film medium and incident on the photonic crystal.  $-1$ ,  $1$ , and  $2$  are nonzero diffraction orders. Blue arrows represent the propagation of guided modes in the thin silicon film. For potential application in photovoltaics, thin metallic rear contacts (grey) are sketched, but are not considered in our nanophotonic simulations.

54 Efficient light trapping enhances the photovoltaic efficiency of silicon solar cells while  
55 sustaining the advantages of thin silicon film [10, 17–19]. In traditional light trapping approaches,  
56 one increases the light paths in a solar cell using random texturing [20, 21] to scatter incident  
57 light into long oblique light paths and uses a back reflector to reflect unabsorbed light back into  
58 the solar cell. In practice, perfect scattering is impossible to achieve, which limits the attainable  
59 efficiency [22]. An ideal back reflector reflects light incident from any angle, also referred to as  
60 omnidirectional reflectivity [23], and ideally for all wavelengths and all polarizations of light.  
61 As illustrated in Fig. 1(right), a perfect metal with 100% reflectivity at all wavelengths and all  
62 polarizations would thus seem to be an ideal back reflector. In practice, no metal has 100%  
63 reflectivity at all wavelengths due to Ohmic losses [24]. Moreover, light that is not reflected by a  
64 real metal gets absorbed, which produces heat and further limits the photovoltaic efficiency of a  
65 solar cell.

66 Notably, much work has been devoted to light trapping strategies based on wave optics [25–29].  
67 These strategies outperform random scattering optics approaches, typically over broad wavelength  
68 ranges, where one takes advantage of enhancements caused by constructive interference. To  
69 manipulate the interference, specially designed nano-structures are pursued, including 1D ("Bragg  
70 stack"), 2D, and 3D photonic crystals [30–42].

71 In this paper, we focus on photonic crystal back reflectors with a *complete 3D photonic band*  
72 *gap* [43, 44], a frequency range for which the propagation of light is rigorously forbidden for all  
73 incident angles and all polarizations simultaneously, as recently demonstrated in experiments  
74 and calculations [45–52]. To illustrate this concept, Fig. 1 shows a schematic design of a thin

75 silicon film (orange) with a 3D photonic band gap crystal back reflector (purple). Incident light  
76 with intensity  $I_0$  is Fresnel diffracted to intensity  $I_1$  within the thin film. When the incident light  
77  $I_1$  has a frequency in the photonic band gap, it is reflected by the photonic crystal [43] back  
78 into the film. The specular reflected beam corresponds to the 0<sup>th</sup> diffraction order. Figure 1  
79 illustrates non-zeroth order diffraction modes, *e.g.*,  $-1$ ,  $1$ , and  $2$ , that are generated at the periodic  
80 interface between the thin film and the photonic crystal. These diffraction modes couple light  
81 into guided modes that are confined inside the thin silicon film via total internal reflection.  
82 Consequently, guided photons obtain a long path length inside the thin film and have thus an  
83 enhanced probability for absorption. Hence, different from a perfect metal, a 3D photonic crystal  
84 enhances the absorption of a thin silicon film by (i) profiting from perfect reflectivity inside the  
85 band gap for all incident angles and polarizations, and (ii) by generating guided modes [36, 39].  
86 Apart from photovoltaics, an enhanced absorption in thin and ultrathin silicon films also has  
87 applications in notably compact on-chip sensors, diodes and avalanche photodiodes, and in CCDs,  
88 all of which have vast societal impact [53–58].

89 Recently, we reported a numerical study on the enhanced energy density and optical absorption  
90 for realistic and finite 3D silicon photonic band gap crystals with an embedded resonant  
91 cavity [59, 60]. The absorption was found to be substantially enhanced, but only within the tiny  
92 cavity volume, as opposed to the present case where the absorption occurs throughout the whole  
93 film volume, which avoids local heating and non-linear or many-body effects that adversely  
94 affect the photovoltaic efficiency [3]. While a structure with a 3D photonic band gap is from  
95 the outset relevant as an omnidirectional, broadband, and polarization-robust back reflector for  
96 ultrathin silicon films (including solar cells), they have been hardly studied before. Therefore, we  
97 investigate nanostructured back reflectors with a 3D photonic band gap that is tailored to have  
98 a broad photonic band gap in the visible regime. Using numerical finite-element solutions of  
99 the 3D time-harmonic Maxwell equations, we calculate the absorption of light in a thin silicon  
100 film with a 3D inverse woodpile photonic crystal as a back reflector. To make our calculations  
101 relevant to experimental studies, we employ a dispersive and complex refractive index obtained  
102 from experiments [61] and compare the photonic crystal back reflector to a perfect metallic back  
103 reflector. We verify that the absorption is not enhanced by the extra material volume. Ultimately,  
104 we aim to understand the physics behind large enhancements by identifying the relevant physical  
105 mechanisms compared to a standard back reflector.

## 106 2. Methods

### 107 2.1. Structure

108 For the photonic band gap back reflector we have chosen the cubic inverse woodpile crystal  
109 structure [62], on account of its broad band gap that is robust to disorder [63, 64], and since this  
110 structure is readily fabricated from silicon [65], and thus a suitable candidate for integration  
111 with thin silicon film solar cells. The crystal structure is shown in Fig. 2(a) and consists of  
112 two arrays of identical nanopores with radius  $r$  running in two orthogonal directions X and  
113 Z. Each nanopore array has a centered-rectangular lattice with lattice parameters  $c$  and  $a$ , see  
114 also Appendix A. For a ratio  $\frac{a}{c} = \sqrt{2}$ , the diamond-like structure has cubic symmetry. Cubic  
115 inverse woodpile photonic crystals have a broad maximum band gap width  $\Delta\omega/\omega_c = 25.3\%$   
116 relative to the central band gap frequency  $\omega_c$  for pores with a relative radius  $\frac{r}{a} = 0.245$  [63, 64].  
117 Our prior results reveal that a reflectivity in excess of  $R > 99\%$  and a transmission  $T < 1\%$   
118 occur **already** for a thin inverse woodpile photonic crystal with a thickness of a few unit cells  
119 ( $L_{3DPC} \geq 3c$ ) [44, 51]. Therefore, we choose here a cubic inverse-woodpile crystal with an  
120 optimal pore radius  $\frac{r}{a} = 0.245$  and with a thickness  $L_{3DPC} = 4c = 1200$  nm as a back reflector  
121 for the calculation of the absorption of light by the thin silicon film.

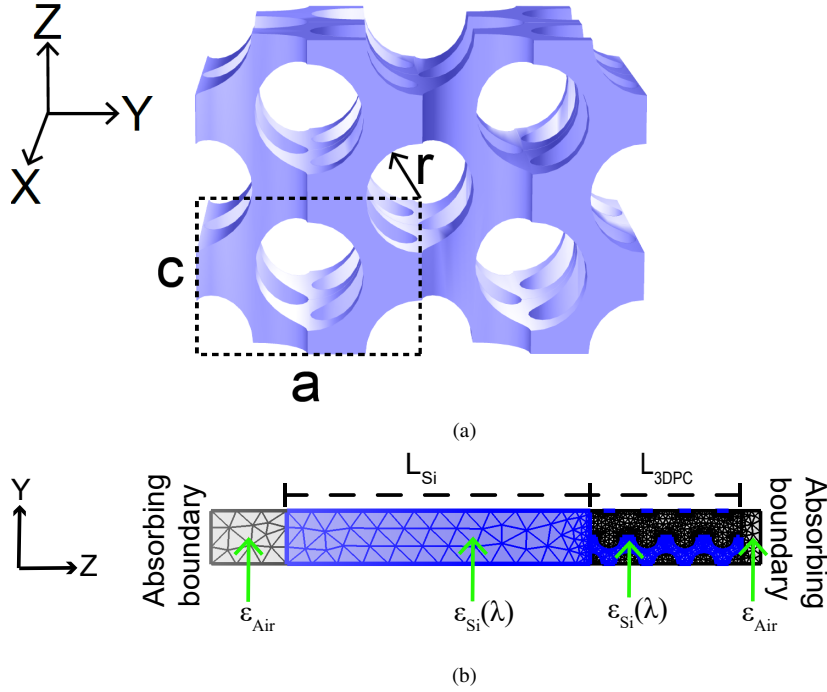


Fig. 2. (a) Schematic of the 3D inverse woodpile photonic crystal structure with the XYZ coordinate axes. We show a  $2 \times 2 \times 2$  supercell, with two arrays of identical nanorods with radius  $r$  parallel to the X and Z axes. The lattice parameters of the tetragonal unit cell are  $c$  and  $a$ , in a ratio  $\frac{a}{c} = \sqrt{2}$  for cubic symmetry. The blue color represents the high-index material with a dielectric function similar to silicon. (b) Computational cell bounded by absorbing boundaries at  $-Z$  and  $+Z$ , and by periodic boundary conditions at  $\pm X$  and  $\pm Y$ . The thin silicon film with thickness  $L_{Si} = 2400$  nm is the absorbing layer and a 3D inverse woodpile photonic crystal with thickness  $L_{3DPC} = 4c = 1200$  nm is the back reflector.

123 To calculate the optical absorption in a thin silicon film, we employ the commercial COMSOL  
 124 Multiphysics finite-element (FEM) software to solve the time-harmonic Maxwell equations [66].  
 125 Figure 2 (b) illustrates the computational cell viewed in the YZ plane. The incident fields start  
 126 from a plane at the left that is separated from the silicon layer by an air layer. Since the plane also  
 127 absorbs the reflected waves [67], it represents a boundary condition rather than a true current  
 128 source. The incident plane waves have either  $s$  polarization (electric field normal to the plane of  
 129 incidence) or  $p$  polarization (magnetic field normal to the plane of incidence), and have an angle  
 130 of incidence between  $\theta = 0^\circ$  and  $80^\circ$ . We employ Bloch-Floquet periodic boundaries in the  $\pm X$   
 131 and the  $\pm Y$  directions to describe the infinitely extended thin silicon film [43]. To describe a  
 132 thin film with finite support, absorbing boundaries are employed in the  $-Z$  and  $+Z$  directions.  
 133 We calculate reflectivity and transmission of the thin film at the absorbing boundaries in the  $-Z$   
 134 and  $+Z$  directions, respectively. The light with a given wavelength  $\lambda$  incident at an angle  $\theta$  with  
 135 respect to the surface normal is either reflected or transmitted, or absorbed by the thin film [24].  
 136 To calculate the absorption  $A_{Si}(\lambda, \theta)$  of a thin silicon film, we employ the relation

$$A_{Si}(\lambda, \theta) = 1 - R_{Si}(\lambda, \theta) - T_{Si}(\lambda, \theta), \quad (1)$$

137 with  $R_{Si}(\lambda, \theta)$  the reflectivity and  $T_{Si}(\lambda, \theta)$  the transmission spectra that are normalized to the  
 138 incident light intensity  $I_0$ .

139 To gauge the performance of a 3D photonic band gap back reflector, we define the wavelength  
 140 and angle-dependent absorption enhancement  $\eta_{abs}(\lambda, \theta)$  of the thin silicon film in Fig. 2 as

$$\eta_{abs}(\lambda, \theta) \equiv \frac{\int_{\lambda-\Delta\lambda}^{\lambda+\Delta\lambda} P_{AM1.5}(\lambda) A_{(Si+3DPC)}(\lambda, \theta) d\lambda}{\int_{\lambda-\Delta\lambda}^{\lambda+\Delta\lambda} P_{AM1.5}(\lambda) A_{Si}(\lambda, \theta) d\lambda}, \quad (2)$$

141 where the absorption is weighted with the solar spectrum using the air mass coefficient  
 142  $P_{AM1.5}(\lambda)$  [8]. In Eq. 2,  $A_{(Si+3DPC)}$  represents the absorption in a thin silicon film with a  
 143 3D photonic crystal back reflector and  $A_{Si}$  the absorption in a thin silicon film with the same  
 144 thickness, yet no back reflector. Using Eq. 2, the enhancement is averaged over a bandwidth  
 145 ( $2\Delta\lambda$ ) at every discrete wavelength  $\lambda$ .

146 At normal incidence ( $\theta = 0^\circ$ ) the absorption enhancement  $\eta'_{abs}(\lambda)$  is deduced from Eq. 2 to

$$\eta'_{abs}(\lambda) \equiv \frac{\int_{\lambda-\Delta\lambda}^{\lambda+\Delta\lambda} P_{AM1.5}(\lambda) A_{(Si+3DPC)}(\lambda) d\lambda}{\int_{\lambda-\Delta\lambda}^{\lambda+\Delta\lambda} P_{AM1.5}(\lambda) A_{Si}(\lambda) d\lambda}. \quad (3)$$

147 To calculate the angle-averaged absorption enhancement  $\eta''_{abs}(\lambda)$ , the enhancement  $\eta_{abs}(\lambda, \theta)$   
 148 (Eq. 2) is averaged over  $n$  incident angles  $\theta_i$  to

$$\eta''_{abs}(\lambda) \equiv \frac{1}{n} \sum_{i=1}^{i=n} \eta_{abs}(\lambda, \theta_i). \quad (4)$$

149 Figure 2 (b) illustrates the finite element mesh of tetrahedra that are used to subdivide the  
 150 3D computational cell into elements [68]. Since the computations are intensive due to a finite  
 151 element mesh of 167000 tetrahedra, we performed the calculations on the powerful ‘‘Serendipity’’  
 152 cluster [69] at MACS in the MESA+ Institute (see also Ref. [59]).

153 To enhance the weak absorption of silicon above the electronic band gap at wavelengths in the  
 154 range  $600 \text{ nm} < \lambda < 1100 \text{ nm}$ , we tailor the lattice parameters of the inverse woodpile photonic  
 155 crystal to  $a = 425 \text{ nm}$  and  $c = 300 \text{ nm}$  such that the band gap is in the visible range. The chosen  
 156 lattice parameters are 37% smaller than the ones usually taken for photonic band gap physics in  
 157 the telecom range [44–46, 48–52, 70]. The nanopore radii are taken to be  $\frac{r}{a} = 0.245$ , i.e.,  $r = 104$   
 158 nm in order for the broadest possible band gap [63, 64]. The required dimensions are well within  
 159 the feasible range of nanofabrication parameters [65, 71, 72].

160 To benchmark our proposition of using a 3D inverse woodpile photonic crystal as a back  
 161 reflector, we compare the absorption spectra to spectra for the same thin silicon layer with a  
 162 perfect and omnidirectional metallic back reflector. Therefore, in our simulations we replace the  
 163 photonic crystal and the air layer on the right in Fig. 2 (b) with a homogeneous metallic plane  
 164 with a large and purely imaginary refractive index  $n'' = -i \cdot 10^{20}$ .

165 For reference, we also show results for ideal Lambertian scattering, also known as Yablonovitch  
 166 or  $4n^2$  limit [73], with the understanding that in the present case we do not consider a scattering  
 167 front (or back) surface, in order to keep the calculations and interpretation of our photonic band  
 168 gap back reflector tractable. In the Lambertian case, the absorption  $A_{Si}^L(\lambda)$  of a thin silicon film  
 169 with thickness  $L_{Si}$  and refractive index  $n_{Si}(\lambda) = \text{Re}(n_{Si}(\lambda)) + \text{Im}(n_{Si}(\lambda))$  is equal to

$$A_{Si}^L(\lambda) = \frac{\alpha(\lambda) L_{Si}}{\alpha(\lambda) L_{Si} + \frac{1}{F(\lambda)}}, \quad (5)$$

170 where  $\alpha(\lambda)$  is the absorption coefficient that is equal to  $\alpha(\lambda) = \frac{4\pi \text{Im}(n_{Si}(\lambda))}{\lambda}$ , and  $F(\lambda)$  the  
 171 optical path length enhancement factor equal to  $F(\lambda) = 4 \text{Re}(n_{Si}(\lambda))^2$  [74].

172 **3. Results and discussion**

173 In the first two subsections, we show the main results, namely the absorption enhancements for  
 174 silicon films thicker and thinner than the wavelength. In the subsequent subsections, we discuss  
 175 detailed physical backgrounds, including film thickness, angular acceptance, and absence of  
 176 photonic crystal backbone contributions to the overall absorption.

177 **3.1. Supra-wavelength silicon film**

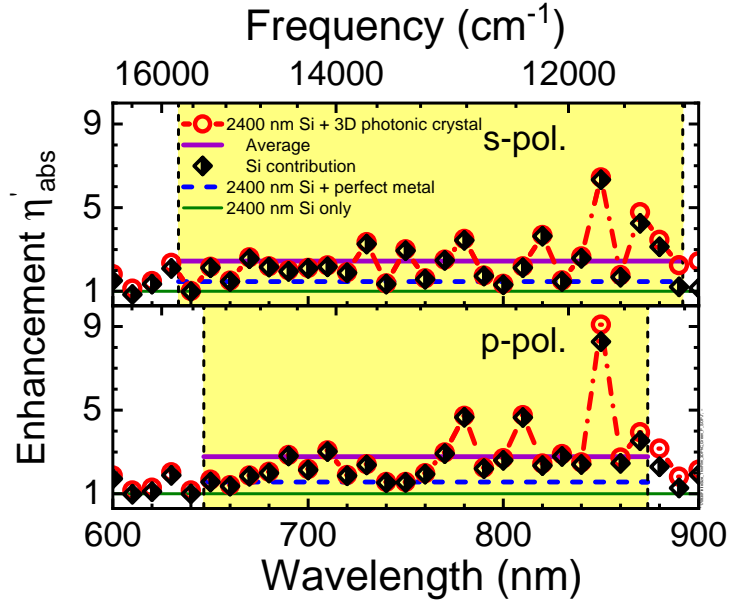


Fig. 3. Normal incidence absorption enhancement spectra  $\eta'_{abs}(\lambda)$  for a thin silicon film ( $L_{Si} = 2400$  nm) with several back reflectors computed using Eq. 3 with a bandwidth  $2\Delta\lambda = 10$  nm at each wavelength bin  $\lambda$ . The top panel is for  $s$ -polarized light and the bottom panel for  $p$ -polarized light. Red connected circles are data for a thin film with the 3D photonic crystal back reflector, the purple horizontal line is the average enhancement (using Eq. 3 with a bandwidth  $2\Delta\lambda$  equal to the  $s$ - and  $p$ -stop bands, respectively), the black diamonds are for the thin film part only, and the blue short-dashed line is for the thin film with a perfect metal back reflector. The vertical dashed lines show the edges of the  $s$ - and  $p$ -stop bands, with the stop bands shown as yellow bars.

178 Figure 3 shows the normal incidence absorption enhancement  $\eta'_{abs}(\lambda)$  (Eq. 3) of a supra-  
 179 wavelength  $L_{Si} = 2400$  nm thin silicon film for both the perfect metal and the 3D photonic  
 180 crystal back reflectors. For the 3D inverse woodpile back reflector, the absorption enhancement  
 181 varies between  $\eta'_{abs} = 1\times$  and  $9\times$  inside the stop bands between  $\lambda = 640$  nm and 900 nm. The  
 182 wavelength-averaged absorption enhancement is about  $\langle\eta'_{abs}\rangle = 2.22\times$  for the  $s$ -stop band and  
 183  $\langle\eta'_{abs}\rangle = 2.45\times$  for the  $p$ -stop band. In comparison, for a perfect metal back reflector the  
 184 wavelength-averaged absorption enhancement is about  $\langle\eta'_{abs}\rangle = 1.47\times$  for the  $s$ -stop band and  
 185  $\langle\eta'_{abs}\rangle = 1.56\times$  for the  $p$ -stop band. Since a perfect metal back reflector has 100% specular  
 186 reflectivity only in the specular  $0^{\text{th}}$  diffraction order, the absorption enhancement  $\eta'_{abs}$  is always  
 187 less than two:  $\langle\eta'_{abs}\rangle \leq 2$ . In contrast, a photonic band gap crystal back reflector also has

188 non-zero order diffraction modes, see Fig. 1, that scatter light into guided modes where light  
 189 is confined inside the thin silicon film via total internal reflection. Since the effective optical  
 190 path length travelled by a photon in a guided mode is longer than the path length travelled with  
 191 only the 0<sup>th</sup> order diffraction mode, a photonic crystal back reflector yields a greater absorption  
 192 enhancement  $\langle \eta'_{abs} \rangle \geq 2$  for the diffracted wavelengths, as is apparent in Fig. 3. This observation  
 193 is a first support of the notion that a 3D photonic band gap back reflector enhances the absorption  
 194 of a thin silicon film by (i) behaving as a perfect reflector with nearly 100% reflectivity for both  
 195 polarizations, and (ii) exciting guided modes within the thin film.

196 Since the high-index backbone of the 3D inverse woodpile photonic crystal consists of silicon,  
 197 one might surmise that the absorption is enhanced by the addition of the photonic crystal's  
 198 silicon backbone to the thin silicon film. To test this hypothesis, we calculate the absorption  
 199 enhancement within the thickness  $L_{Si}$  of the thin silicon film part (see Fig. 2 (b)) using the  
 200 volume integral of the total power dissipation density from Ref. [66]. Figure 3 shows that the  
 201 absorption enhancement spectra for the thin film volume agree very well with the spectra of the  
 202 complete device (both thin film and photonic crystal) in the stop bands between  $\lambda = 640$  nm and  
 203 900 nm. Therefore, the high-index backbone of the 3D photonic crystal contributes *negligibly* to  
 204 the absorption inside the stop bands, even in the visible regime. Apparently, light that travels  
 205 from the thin film into the photonic crystal is reflected back into the thin film, even before it is  
 206 absorbed in the photonic crystal. To bolster this conclusion, we start with the notion that the  
 207 typical length scale for reflection by a photonic crystal is the Bragg attenuation length  $\ell_{Br}$  [75]  
 208 that qualitatively equals the ratio of the central stop band wavelength and the photonic interaction  
 209 strength  $S$  times  $\pi$ :  $\ell_{Br} = \lambda_c / (\pi S)$  [76, 77], where the strength  $S$  is gauged by the ratio of the  
 210 dominant stop band width and the central wavelength ( $S = \Delta\lambda / \lambda_c$ ). From the stop band between  
 211  $\lambda = 640$  nm and 900 nm ( $S = 260/770 = 0.34$ ) we arrive at  $\ell_{Br} = 770 / (\pi \cdot 0.34) = 725$  nm,  
 212 which is much less than the absorption length of silicon:  $\ell_{Br} \ll l_a$ . Thus, the broad bandwidth  
 213 of the back reflector's 3D photonic band gap is an important feature to enhance the absorption  
 214 inside the thin silicon film itself, as the broad bandwidth corresponds to a short Bragg length.

### 215 3.2. Sub-wavelength silicon film

216 Figure 4 shows the normal incidence absorption enhancement  $\eta'_{abs}(\lambda)$  (Eq. 3) of a  $L_{Si} = 80$   
 217 nm ultrathin silicon film, whose thickness is much less than the wavelength in the material  
 218 ( $L_{Si} \ll \lambda/n$ ), hence no guided modes are sustained in the film itself. Since the thickness is also  
 219 much less than the silicon absorption length  $L_{Si} \ll l_a = 1000$  nm between  $\lambda = 600$  nm and  
 220 900 nm [61], the absorption  $A_{Si}$  of the ultrathin film itself is low, namely about 4.5% at the blue  
 221 edge of the photonic stop bands) and 0.2% at the red edge of the stop band, see Fig. 5. These  
 222 results agree with a Fabry-Pérot analysis of the ultrathin film, which reveals a broad first order  
 223 resonance near  $\lambda = 570$  nm that explains the increased absorption towards the short wavelengths.

224 For the perfect metal back reflector in Fig. 4, the absorption is reduced ( $\eta'_{abs}(\lambda) < 1$ ) at  
 225 wavelengths  $\lambda < 730$  nm and enhanced ( $\eta'_{abs}(\lambda) > 1$ ) at longer wavelengths. This result is  
 226 understood from the Fabry-Pérot behavior of the ultrathin film in presence of the perfect metal,  
 227 that induces an additional  $\pi$  phase shift (due to the exit surface reflectivity) to the roundtrip phase.  
 228 Consequently, a first order resonance appears near  $\lambda = 1140$  nm, and the next anti-resonance  
 229 near  $\lambda = 600$  nm. Therefore, the absorption is enhanced towards  $\lambda = 1140$  nm and reduced  
 230 towards  $\lambda = 600$  nm, in agreement with the results in Fig. 4. The corresponding wavelength-  
 231 averaged absorption enhancements are  $\langle \eta'_{abs} \rangle = 0.8\times$  for *s*-polarized and  $\langle \eta'_{abs} \rangle = 0.85\times$  for  
 232 the *p*-polarized stop band. In other words, a perfect metal back reflector hardly enhances the  
 233 absorption for ultrathin films with the thickness corresponding to a Fabry-Pérot minimum for the  
 234 desired wavelengths of absorption enhancement.

235 In presence of a photonic band gap back reflector, the wavelength-averaged absorption  
 236 enhancement is surprisingly larger, see Fig. 4. The strong increase is clearly illustrated by

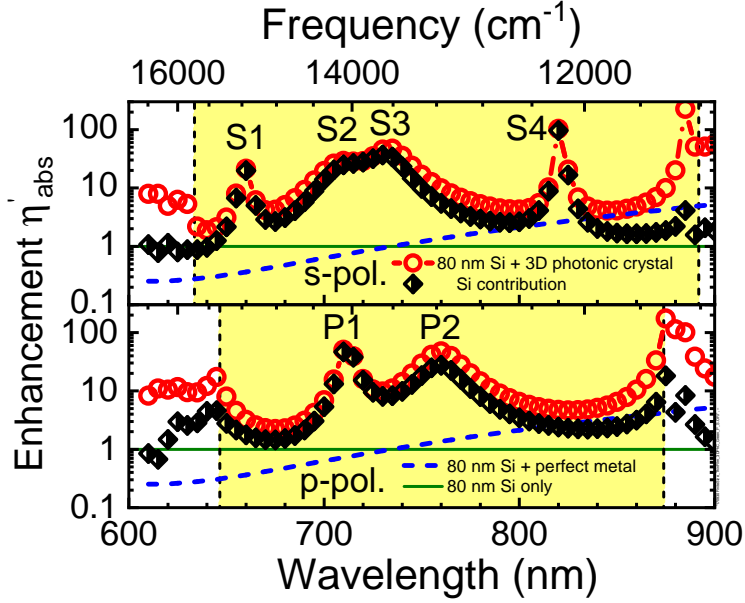


Fig. 4. Absorption enhancement spectra  $\eta'_{abs}(\lambda)$  for a sub-wavelength ultrathin silicon layer ( $L_{Si} = 80$  nm), taken as ratio of absorption  $A$  with a back reflector and absorption  $A_{Si}$  without back reflector, all at normal incidence computed using Eq. 3. Top panel:  $s$ -polarized, bottom panel:  $p$ -polarized light, with  $s$ - and  $p$ -stop bands shown as yellow highlighted regions. Red connected circles pertain to the ultrathin film with a 3D photonic crystal back reflector and the black diamonds are for the silicon part only. The blue dashed curves pertain to the ultrathin film with a perfect metal back reflector and the green lines are the reference level of the ultrathin film without a back reflector.

237 the use of a logarithmic scale. We see several peaks between  $\lambda = 600$  nm and 900 nm in  
 238 Fig. 4, four absorption resonances (S1, S2, S3, and S4) inside the  $s$ -polarized stop band and  
 239 two absorption resonances (P1 and P2) inside the  $p$ -polarized stop band with enhancements  
 240 as high as  $\eta'_{abs} = 100\times$  for both polarizations. The wavelength-averaged enhancements are  
 241  $\langle \eta'_{abs} \rangle = 13.5\times$  for the  $s$ -polarized stop band and  $\langle \eta'_{abs} \rangle = 11.4\times$  for the  $p$ -polarized stop band.  
 242 Since the thickness of the ultrathin silicon  $L_{Si} = 80$  nm does not sustain guided modes at the  
 243 wavelengths within these stop bands, the enhanced absorption peaks must be induced by the  
 244 presence of the photonic crystal back reflector, which has an effective refractive index smaller  
 245 than that of silicon (see Appendix A), and hence leads to no phase shift like the metallic back  
 246 reflector.

247 Considering that this ultrathin silicon layer is much thinner than the one in Sec. 3.1, there is a  
 248 likelihood that the absorption is enhanced by the extra silicon volume from the photonic crystal's  
 249 backbone, whose thickness is much greater than the film thickness, namely  $L_{3DPC} = 1200$  nm  
 250 versus  $L_{Si} = 80$  nm. To test this hypothesis, we calculated the absorption within the volume of  
 251 the ultrathin silicon film part only ( $L_{Si} = 80$  nm), using the power per unit volume formula of  
 252 Ref. [66], as shown in Fig. 5 (from which Fig. 4 is deduced) with various back reflectors for  $s$  and  
 253  $p$  polarizations. The enhanced absorption at all six resonances S1-S4, and P1-P2 occur in the  
 254 ultrathin film volume only. The wavelength-averaged absorption enhancement within the ultrathin  
 255 film part is  $\langle \eta'_{abs} \rangle = 10.46\times$  averaged over the  $s$ -polarized stop band and  $\langle \eta'_{abs} \rangle = 7.84\times$  for the  
 256  $p$ -polarized stop band, which are nearly the same as in the full device. Therefore, we conclude  
 257 that the absorption in the photonic crystal hardly contributes to the enhanced absorption and

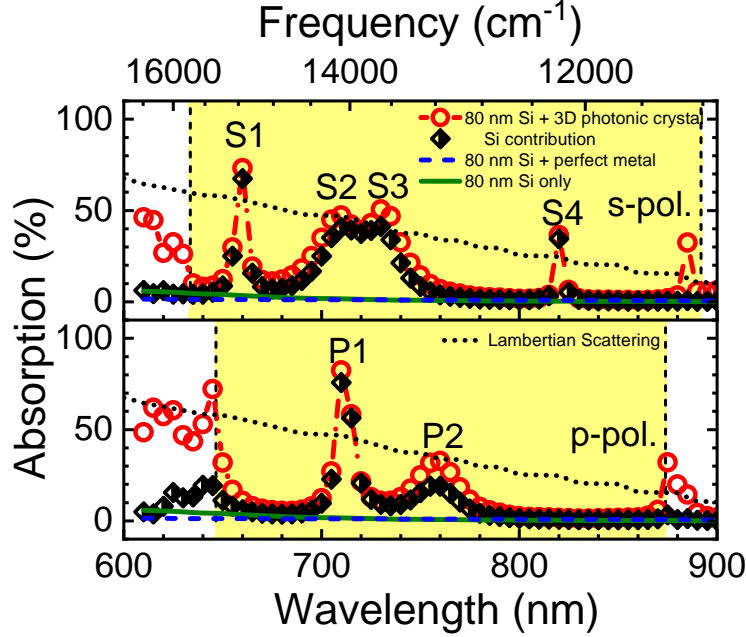


Fig. 5. Absolute absorption spectra (in %) for a sub-wavelength ultrathin silicon layer ( $L_{Si} = 80$  nm) at normal incidence. Top panel:  $s$ -polarized, bottom panel:  $p$ -polarized light, with  $s$ - and  $p$ -stop bands shown as yellow highlighted regions. Red connected circles pertain to the ultrathin film with a 3D photonic crystal back reflector, whereas the black diamonds show the contribution of the ultrathin film only. Green solid curves pertain to an ultrathin film without a back reflector, and blue dashed curves to an ultrathin film with a perfect metal back reflector. Black dotted curves represent absorption  $A_{Si}^L(\lambda)$  with Lambertian scattering, from Eq. 5.

258 does not induce the presence of the absorption peaks. Figure 4 reveals that the absorption within  
 259 the ultrathin film and the one within the whole device (both ultrathin film and photonic crystal)  
 260 match very well near the center of the  $s$ - and  $p$ -stop bands and differ at the edges. The reason  
 261 is that the Bragg attenuation length  $\ell_{Br}$  is smallest near the center of the stop band, while it  
 262 increases toward the band edges where it leads to more absorption in the crystal before the light  
 263 is reflected within a Bragg length.

264 For reference, Fig. 5 also shows the absorption limit due to Lambertian scattering (Eq. 5) for  
 265 the  $L_{Si} = 80$  nm ultrathin film. We note that in between the resonances, the absorption with the  
 266 3D photonic band gap back reflector is below the Lambertian limit. In contrast, at all six  $s$ -  
 267 and  $p$ -polarized resonances (S1-S4 and P1-P2) the 3D photonic band gap back reflector results  
 268 exceed the Lambertian absorption, with the footnote that our calculation invokes a flat top surface  
 269 and no optimized scattering surface. In the modern view, an absorption beyond Lambertian  
 270 limit occurs if the local density of states (LDOS) inside the absorbing layer exceeds the LDOS  
 271 outside [19]. In one view point, the combination of ultrathin film with photonic back reflector  
 272 leads to new resonances (S1-S4 and P1-P2, see below) that have a higher LDOS than the vacuum  
 273 before the absorbing layer (above in Fig. 1). Alternatively, since a photonic band gap blocks all  
 274 incident radiation and inhibits the LDOS, a photonic band gap back reflector may be viewed as a  
 275 vacuum below the absorbing film that has a much lower LDOS than the one in the film itself.

276 To investigate the physics behind these intriguing peaks, we discuss the electric field distributions  
 277 for the exemplary resonances S3 and P1. The incident light with wavevector in the Z-direction



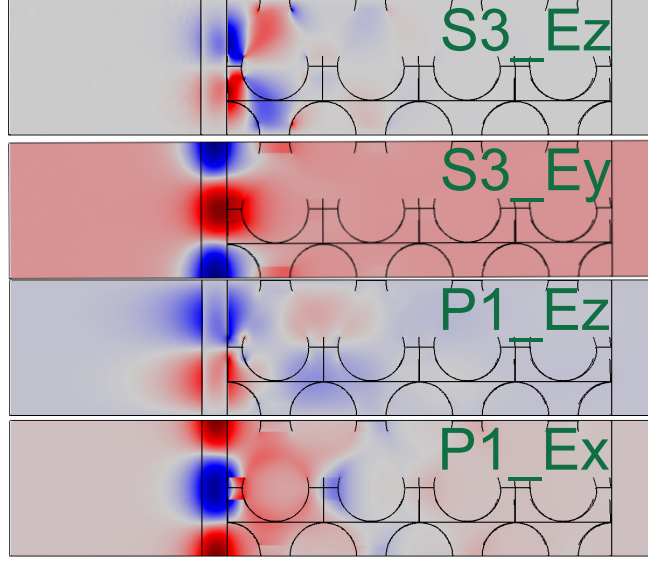


Fig. 6. Distribution of the electric field components for waves propagating in the sub-wavelength ultrathin film ( $L_{Si} = 80$  nm) with a 3D photonic band gap back reflector. S3 and P1 are absorption resonances from Fig. 4, and we show field components that are not present in the incident waves. Red and blue denote the maxima and the minima of the electric field components, respectively.

278 has either  $s$  polarization ( $\mathbf{E}$ -field in the  $X$ -direction) or  $p$  polarization ( $\mathbf{E}$ -field in the  $Y$ -direction).  
 279 To filter the scattered electric fields that are guided in the plane of the ultrathin layer from  
 280 possibly overwhelming incident fields, we plot in Fig. 6 the field components that are *absent*  
 281 in the incident light. Thus, we plot the  $E_z$  and  $E_y$  field components of the S3 resonance that is  
 282 excited by  $s$ -polarized light ( $\mathbf{E}_{in,X}$ ), and the  $E_z$  and  $E_x$  components of the P1 resonance that is  
 283 excited by  $p$ -polarized light ( $\mathbf{E}_{in,Y}$ ).

284 First, we discuss the S3  $E_y$  and P1  $E_x$  field components that are transverse to the incident  
 285 direction, and perpendicular to the incident polarization. Both components are maximal inside  
 286 the ultrathin silicon film, as expected for guided waves. The field distributions show periodic  
 287 variations in the plane of the ultrathin film that are also characteristic of guided modes [29, 78].  
 288 The periods match with the crystal's lattice parameter, which suggests that the fields are part of a  
 289 Bloch mode. The fields extend into the photonic crystal by about one unit cell, in agreement with  
 290 a Bragg attenuation length of about  $\ell_{Br} = 0.6c = 180$  nm at the  $p$ -stop band center that was  
 291 computed in Ref. [44].

292 For the other two field components S3  $E_z$  and P1  $E_z$ , the maximum fields are located at the  
 293 air-silicon and at the silicon-photonic crystal interfaces, and the amplitudes decay away from the  
 294 interfaces. The components show less conventional guiding behavior: the S3  $E_z$  component  
 295 is maximal just *inside* the photonic crystal (by about a quarter unit cell), and has a nodal plane  
 296 parallel to the ultrathin film. The P1  $E_z$  component has maxima on either side of the ultrathin  
 297 silicon film, somewhat like the field pattern of a long-range surface plasmon polariton (LRSPP)  
 298 on a thin metal film [79, 80]. This field extends about  $\Delta Z = 1$  unit cell into the crystal. These field  
 299 distributions are the plausible signature of the confinement of a surface mode [43, 81]. Hence, the  
 300 device can be viewed as an ultrathin absorbing dielectric film on top of a photonic crystal, which  
 301 thus acts as a surface defect on the crystal and sustains a guided surface state. Consequently,  
 302 the remarkable peaks observed in Fig. 4 correspond to guided modes confined in an ultrathin  
 303 layer consisting of two separate contributions: (i) a non-zero thickness layer due to the Bragg

304 attenuation length of the crystal's band gap, and (ii) a deeply sub-wavelength ultrathin silicon  
 305 film.

306 **3.3. Wavelength-resolved transmission and absorption**

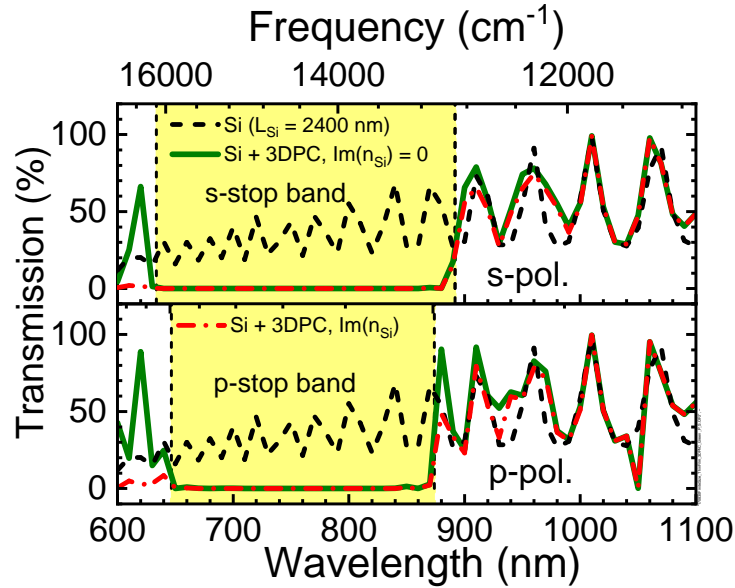


Fig. 7. Transmission spectra calculated for a thin silicon film ( $L_{Si} = 2400$  nm) at normal incidence. Top panel:  $s$  polarization, bottom panel:  $p$  polarization. Black dashed curves are the transmission spectra for a thin film. Green solid curves are results for the thin film with a 3D inverse woodpile photonic crystal back reflector, with dispersion but no silicon absorption ( $\text{Im}(n_{Si}) = 0$ ). Red dashed-dotted curves are results for the thin film with a 3D inverse woodpile photonic crystal back reflector, including silicon absorption ( $\text{Im}(n_{Si}) \neq 0$ ). The vertical dashed lines are the edges of the  $s$ - and  $p$ -stop bands that are shown as yellow bars.

307 To analyze the physics behind the results in Sections 3.1 and 3.2, we break the problem down  
 308 into several steps. Firstly, we briefly recapitulate the known situation of a thin silicon film only.  
 309 Secondly, we study the thin film with a photonic crystal back reflector, where we only consider  
 310 dispersion, but no absorption. This fictitious situation allows a comparison to the dispersion-free  
 311 results that pertain to frequencies below the silicon band gap, see Ref. [44]. Thirdly, we study the  
 312 complete device structure with the full silicon dispersion and absorption taken from Ref. [61].

313 Figure 7 reveals oscillations between  $\lambda = 600$  nm and  $\lambda = 1100$  nm for both polarizations  
 314 in the transmission spectra for the thin silicon film ( $L_{Si} = 2400$  nm). These oscillations are  
 315 Fabry-Pérot fringes [82] resulting from multiple reflections of the waves inside the film at the  
 316 front and back surfaces of the thin silicon film.

317 In Fig. 7, we observe nearly 0% transmission between  $\lambda = 600$  nm and  $\lambda = 900$  nm for a thin  
 318 film with a photonic crystal back reflector, both with and without silicon absorption. These deep  
 319 transmission troughs are photonic stop bands between  $\lambda = 647$  nm to 874 nm for  $p$  polarization  
 320 and  $\lambda = 634$  nm to 892 nm for  $s$  polarization. These gaps were previously identified to be the  
 321 dominant stop gaps in the  $\Gamma - X$  and  $\Gamma - Z$  high-symmetry directions (see Appendix B) that  
 322 encompass the 3D photonic band gap [44]. From the good agreement of the stop bands, both  
 323 with and without silicon absorption, we deduce that an inverse woodpile photonic crystal behaves

324 as a perfect reflector in the visible range, even in presence of substantial absorption. This result  
 325 further supports the above observation that the absorption length of silicon is much longer than  
 326 the Bragg attenuation length of the 3D inverse woodpile photonic crystal  $l_a \gg \ell_{Br}$ . Hence,  
 327 waves incident on the photonic crystal are reflected before being absorbed by the high-index  
 328 backbone of the photonic crystal. Thus, the Fabry-Pérot fringes in transmission between  $\lambda = 600$   
 329 nm and  $\lambda = 860$  are completely suppressed by strong and broadband reflection of the 3D photonic  
 330 crystal back reflector [44].

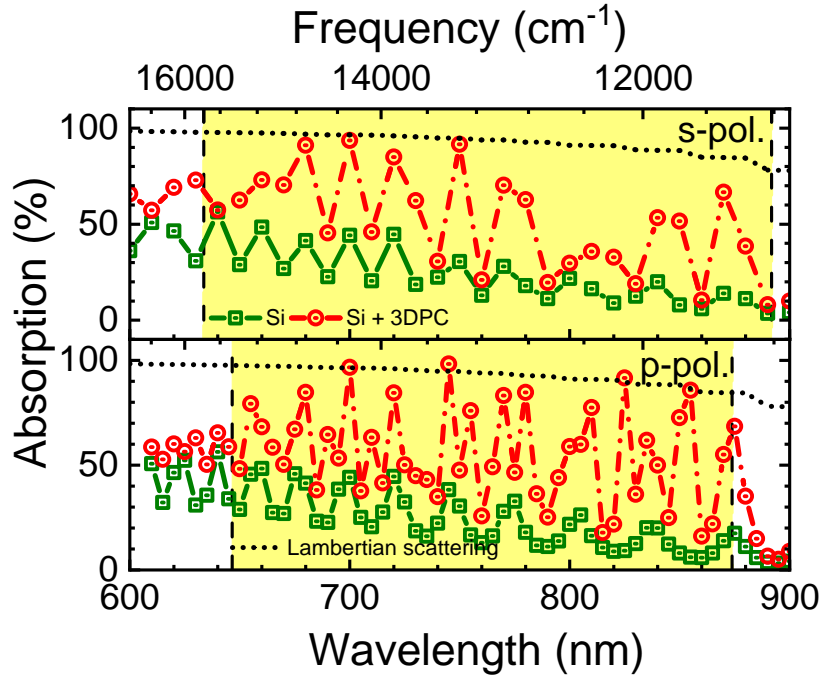


Fig. 8. Absolute absorption (in %) by a thin silicon film ( $L_{Si} = 2400$  nm) in the stop band of a 3D inverse woodpile photonic crystal. Top panel:  $s$ -polarized, bottom panel:  $p$ -polarized light. Green solid curves are absorption spectra for a thin silicon film. Red dashed-dotted curves are absorption spectra for a thin silicon film with a 3D inverse woodpile photonic crystal back reflector. The vertical dashed lines are the edges of the  $s$ - and  $p$ -stop bands. The stop bandwidths are shown as the yellow bar. Black dotted curves represent absorption  $A_{Si}^L(\lambda)$  with Lambertian scattering, from Eq. 5.

331 Furthermore, oscillations below  $\lambda = 600$  nm are present in the transmission spectra for the thin  
 332 silicon film with a photonic crystal back reflector without absorption, but not in the system with  
 333 absorption. Since the transmission spectra with realistic absorption show nearly 0% transmission  
 334 below  $\lambda = 600$  nm, where silicon is strongly absorbing, all light is absorbed and the Fabry-Pérot  
 335 fringes are suppressed.

336 Figure 8 shows the absorption spectra for a thin silicon film without and with a 3D photonic  
 337 crystal back reflector. We consider the dispersive and complex refractive index for the silicon  
 338 and the high-index backbone of the photonic crystal. Fabry-Pérot fringes appear below  $\lambda = 900$   
 339 nm, corresponding to standing waves in the thin silicon film. Since the imaginary part of the  
 340 silicon refractive index increases with decreasing wavelength (see Fig. 15), the absorption in  
 341 silicon also increases with decreasing wavelength.

342 Between  $\lambda = 600$  nm and  $\lambda = 900$  nm in the top and bottom panels of Fig. 8, there are more

343 Fabry-Pérot fringes. The fringes have a greater amplitude for a thin silicon film with photonic  
 344 crystal back reflector, compared to a standalone thin silicon film. To interpret the increased  
 345 number of fringes, we consider diffraction from the photonic crystal surface. In Fig. 1, light  
 346 first travels through silicon before reaching the photonic crystal surface. Therefore, the incident  
 347 wavelength reduces to  $\lambda/n_{Si}$  inside the silicon layer. In the entire stop bands (both  $s$  and  $p$ ) the  
 348 wavelength  $\lambda/n_{Si}(\lambda)$  between  $\lambda = 600$  nm and  $\lambda = 900$  nm is smaller than the lattice parameter  
 349  $c = 300$  nm of the 3D inverse woodpile photonic crystal (along the  $\Gamma Z$  direction). In addition,  
 350 a 3D inverse woodpile photonic crystal introduces a periodic refractive index contrast at the  
 351 interface with a thin silicon film. Hence, nonzero diffraction modes [39,43] are generated at the  
 352 photonic crystal-thin silicon film interface at specific wavelengths inside the stop bands, resulting  
 353 in additional reflected waves that are then absorbed in the film.

354 Between  $\lambda = 600$  nm and 900 nm, the silicon thickness  $L_{Si} = 2400$  nm is larger than half the  
 355 wavelength  $\lambda/n_{Si}$  in the absorbing layer. This is the condition for a photonic crystal-thin silicon  
 356 film interface to couple the reflected waves into the guided modes [24,36] that propagate inside  
 357 the silicon. Hence, the physical mechanism responsible for the additional number of fringes is  
 358 the occurrence of non-zero diffraction modes coupled into guided modes due to the photonic  
 359 crystal back reflector. The absorption in guided modes can sometimes approach 100% [36], *e.g.*,  
 360 at  $\lambda = 700$  nm and 720 nm in Fig. 8 (bottom). We note that the perfect reflectivity of a 3D inverse  
 361 woodpile photonic crystal extends over the entire stop bands, whereas nonzero order diffraction  
 362 modes and guided modes are limited to specific wavelengths. This is in contrast to Section 3.2,  
 363 where we studied a reduced thickness such that no guided modes are allowed.

364 For reference, Fig. 8 also shows the absorption limit due to Lambertian scattering (Eq. 5).  
 365 In most of the spectral range, the absorption with the 3D photonic band gap back reflector is  
 366 below the Lambertian limit. At several resonances, the photonic band gap back reflector results  
 367 match or even slightly exceed the Lambertian limit, again with the footnote that our calculation  
 368 invokes a flat top surface and no optimized scattering surface. The fact that at this thickness the  
 369 results exceed the Lambertian limit less than in the earlier ultrathin case makes intuitive sense;  
 370 if we consider the silicon film as a Fabry-Pérot resonator, and we consider a certain constant  
 371 wavelength, then a thicker resonator corresponds to a greater reduced frequency ( $L_{Si}/\lambda$ ) and  
 372 will show less LDOS modulation than a thin low ( $L_{Si}/\lambda$ ) resonator. Therefore [19], the thick  
 373 resonator is less likely to reveal beyond-Lambertian absorption, in agreement with our results.

### 374 3.4. Negligible absorption inside the photonic crystal backbone

375 Since we propose the back reflector to be a photonic crystal that is also made of silicon, one  
 376 might rightfully hypothesize that the mere presence of extra material in the photonic crystal  
 377 simply increases the total length of silicon, which thus *sneakily* enhances the absorption. To  
 378 evaluate this hypothesis, we compute and compare the absorption for three different devices. We  
 379 first study a thin silicon film of thickness  $L_{Si} = 2400$  nm without back reflector, neither perfect  
 380 metal nor photonic band gap (device #1). Secondly, we consider a silicon film ( $L_{Si} = 2400$  nm)  
 381 with a photonic crystal back reflector with a thickness  $L_{Si} = 1200$  nm; this device #2 has a total  
 382 thickness of 3600 nm. Thirdly, we study a structure with the same total thickness as the second  
 383 one, namely a silicon layer with a thickness  $L_{Si} = 3600$  nm, but without back reflector (device  
 384 #3).

385 To investigate the effect of the band gap on the absorption in the thin film, we zoom in on the  
 386 absorption spectra inside the stop bands in Fig. 9. We observe that the absorption spectra are  
 387 closely the same for both thin films (devices #1 and #3), including the Fabry-Pérot fringes. Since  
 388 film #3 is considerably thicker than #1, the similarity strongly suggests that the silicon absorption  
 389 within the stop band wavelength range is saturated for the thinner layer.

390 In contrast, device #2 with a photonic crystal back reflector reveals significantly higher  
 391 absorption, including a larger amplitude of the Fabry-Pérot fringes than the films #1 and #3.

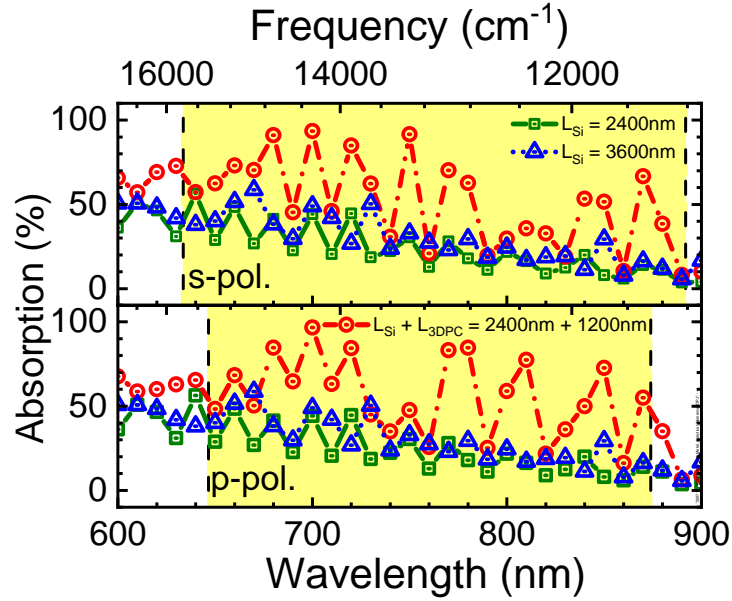


Fig. 9. Verification of the absence of absorption inside the photonic crystal backbone. Top panel:  $s$ -polarized, bottom panel:  $p$ -polarized light, with  $s$ - and  $p$ -stop bands shown as yellow highlighted regions. Green solid curves pertain to a thin film only with the silicon thickness  $L_{Si} = 2400$  nm. Red dashed-dotted curves pertain to a thin silicon film (thickness  $L_{Si} = 2400$  nm) with a 3D photonic crystal back reflector (thickness  $L_{3DPC} = 1200$  nm). Blue dotted curves pertain to a thin film only with the same overall thickness  $L_{Si} = 3600$  nm.

392 Since the total thickness of device #2 is the same as for film #3, we conclude that the enhanced  
 393 absorption of the film with the photonic band gap back reflector is *not* caused by the additional  
 394 thickness of the back reflector itself, hence the *sneaky* effect does not exist. The conclusion  
 395 that the back reflector does not absorb is also reasonable, since we have seen above that the  
 396 absorption of the light mostly occurs within the films themselves. Using Eq. 2, we find that the  
 397 wavelength-averaged absorption enhancement due to a photonic crystal back reflector is nearly  
 398  $\langle \eta'_{abs} \rangle = 1.8\times$  for the  $s$ -stop band and nearly  $\langle \eta'_{abs} \rangle = 1.9\times$  for the  $p$ -stop band compared to a  
 399 thin film with thickness  $L_{Si} = 3600$  nm.

#### 400 4. Practical considerations for devices

##### 401 4.1. Angular acceptance

402 In order to optimize the absorption of a thin silicon film for photovoltaic device applications,  
 403 we first investigate the impact of a 3D photonic crystal back reflector on the angular acceptance.  
 404 Figures 10 (a, b) show transmission maps versus angle of incidence and wavelength. The angle  
 405 of incidence is varied up to  $\theta = 80^\circ$  off the normal. For both polarizations *simultaneously* we  
 406 observe a broad angle-independent stop band that is characterized by near 0% transmission. The  
 407 broad stop band extends all the way from  $\lambda = 680$  nm to  $\lambda = 880$  nm. This shows that the Bragg  
 408 attenuation length for the 3D inverse woodpile photonic crystal is smaller than the absorption  
 409 length of silicon for all incident angles for the omnidirectional stop band. Thus, a 3D photonic  
 410 band gap crystal acts as a perfect reflector in the omnidirectional stop band for all incident angles  
 411 and for all polarizations, even with full absorption in the refractive index - in other words, an

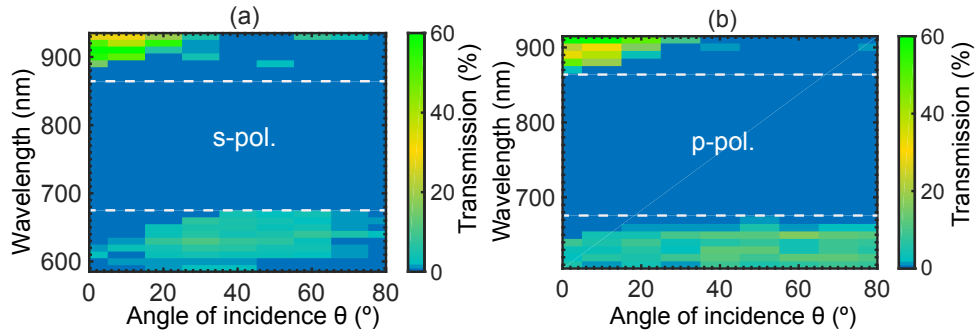


Fig. 10. Angle- and wavelength-resolved transmission spectra calculated for a thin silicon film ( $L_{Si} = 2400$  nm) with a 3D inverse woodpile photonic crystal back reflector for (a)  $s$  polarization and (b)  $p$  polarization. The dark blue color represents nearly 0% transmission that occurs in the stop band at all incident angles. The white dashed box indicates an angle- and polarization-independent range with nearly 0% transmission.

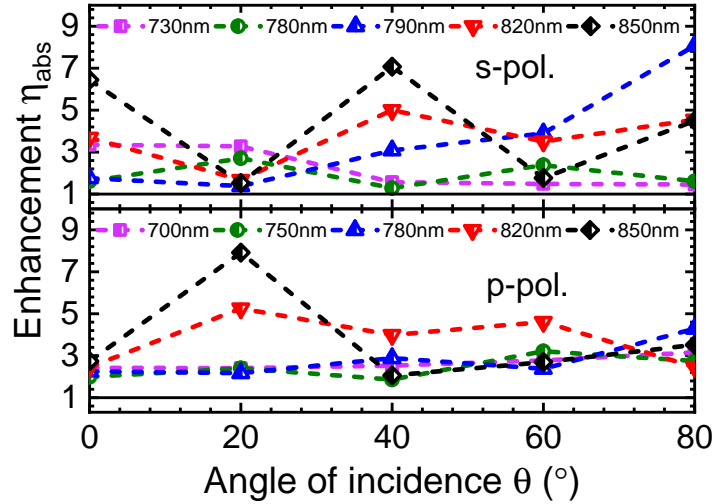


Fig. 11. Absorption enhancement  $\eta_{abs}(\lambda, \theta)$  versus incidence angle  $\theta$  off the surface normal to characterize the angular acceptance of a thin silicon film ( $L_{Si} = 2400$  nm) with a 3D inverse woodpile back reflector, for 5 wavelengths throughout the band gap (850 nm, 820 nm, 790 nm, 760 nm, and 730 nm) with connected symbols and colors as shown in the legend. The top panel is for  $s$ -polarized light, and the bottom panel for  $p$ -polarized light.

412 *omnidirectional* stop band.

413 Figure 11 shows the absorption enhancement  $\eta_{abs}(\lambda, \theta)$  versus incident angle for five repre-  
 414 sentative wavelengths throughout the band gap of a 3D inverse woodpile back reflector. For all  
 415 incident angles up to  $80^\circ$ , we observe that the absorption enhancement stays above 1, which  
 416 corresponds a standalone thin film. Furthermore, at certain incident angles, the absorption  
 417 enhancement is as high as 7 or 9. For both polarizations, Fig. 11 also reveals oscillatory absorption  
 418 enhancement with increasing incident angles, which are signature of the Fabry-Pérot fringes [82].  
 419 Hence, a 3D inverse woodpile crystal widens the angular acceptance of a thin silicon film by

420 creating an omnidirectional absorption enhancement regime for photovoltaics.  
 421 To calculate the angle-averaged and wavelength-averaged absorption enhancement  $\langle \eta''_{abs} \rangle$  in the  
 422 *omnidirectional stop band*, we employ Eq. 4. Consequently, the angle- and wavelength-averaged  
 423 absorption enhancement for *s* polarization is  $\langle \eta''_{abs} \rangle = 2.11\times$  and for *p* polarization is  $\langle \eta''_{abs} \rangle$   
 424  $= 2.68\times$ , which exceeds the maximum absorption enhancement feasible for a perfect metallic  
 425 reflector. These enhancements are possible only if a photonic crystal back reflector generates  
 426 non-zeroth order diffraction modes at certain discrete wavelengths for all incident angles [83].  
 427 Once these non-zero diffraction modes couple into guided modes and are confined inside the thin  
 428 film via total internal reflection, the effective optical path length travelled is longer than the one  
 429 travelled by a zero order diffraction mode. Therefore, a 3D inverse woodpile crystal enhances the  
 430 absorption of a thin silicon film for all incident angles and polarizations by (i) revealing perfect  
 431 reflectivity inside the omnidirectional stop band and (ii) generating guided modes for specific  
 432 wavelengths.

#### 433 4.2. Optimal thickness of the absorbing thin film

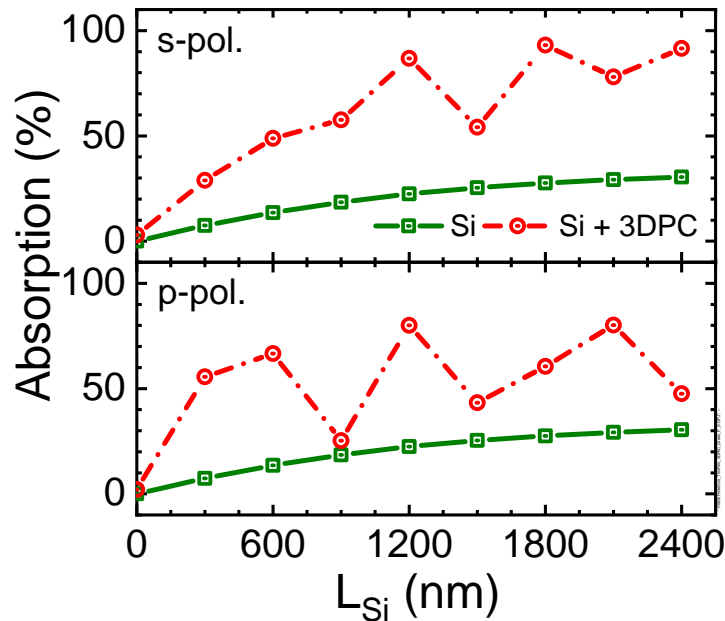


Fig. 12. Absorption versus thickness  $L_{Si}$  of a thin silicon film in presence (connected red circles) of a 3D photonic crystal back reflector, and without back reflector (green squares). The data pertain to a wavelength  $\lambda = 760$  nm, the 3D photonic band gap center of the back reflector. Top panel: *s*-polarized, bottom panel: *p*-polarized light.

434 To investigate the effect of the thickness  $L_{Si}$  of the thin silicon film on its absorption, we plot  
 435 in Fig. 12 the absorption for light at normal incidence for film thicknesses between  $L_{Si} = 300$   
 436 nm and  $L_{Si} = 2400$  nm in presence of a 3D inverse woodpile photonic crystal back reflector  
 437 with a constant thickness  $L_{3DPC} = 1200$  nm. While the absorption for a thin film shows a  
 438 monotonic increase with increasing silicon thickness for both polarizations, Fig. 12 reveals that  
 439 the absorption for a thin film with a photonic crystal back reflector is always higher than the  
 440 corresponding standalone thin film. Furthermore, absorption spectra of a thin film with a photonic  
 441 crystal back reflector reveals oscillations with increasing film thicknesses for both polarizations,

442 showing saturation towards higher wavelength. We surmise that in order to maximize absorption  
443 enhancement for a given wavelength, the thickness of a thin silicon film had better be chosen to  
444 the maxima of the oscillations in Fig. 12. Therefore based on this normal incidence analysis,  
445 when designing a device the thickness of the silicon film had better be tweaked from  $L_{Si} = 2400$   
446 nm to one of the fringe maxima in Fig. 12, such as  $L_{Si} = 1200$  nm or the range 1800 – 2100 nm.

#### 447 4.3. Other experimental considerations

448 To enhance the absorption of light over an even broader wavelength range than reported here, it  
449 is relevant to consider different orientations of the 3D photonic crystal back reflector. In case of  
450 both direct and inverse woodpile structures, it is interesting to consider light incident in the  $\Gamma Y$   
451 direction, since the  $\Gamma Y$  stop gap with a relative bandwidth 39.1 % (see Fig. 2 of Ref. [44]) is about  
452  $1.3\times$  broader than the  $\Gamma Z$  or  $\Gamma X$  stop gaps whose relative bandwidth is 30.4 % [44, 45, 63, 64].

453 To improve the likelihood that photonic band gap back reflectors gain real traction, it is  
454 obviously relevant to consider strategies whereby such a back reflector can be realized over  
455 as large as possible (X,Y) areas. In the current nanofabrication of silicon inverse woodpiles,  
456 an important limitation is the depth of the nanopores that are fabricated by deep reactive-ion  
457 etching [49, 65], which limits the X- or Z-extent of the nanostructures, whereas the Y-extent  
458 has no fundamental limit. Therefore, with the design shown in Fig. 2, the back reflector would  
459 have sufficient Z-extent (thickness) and a large Y-extent, but limited X-extent, and thus limited  
460 area. A remedy consists of etching the nanopores at  $45^\circ$  to the back surface, as demonstrated  
461 by Takahashi *et al.* [84]. Then, the areal (X,Y)-extent of the photonic crystal equals the areal  
462 extent of the pore array, which can be defined by standard optical lithography or by self-assembly.  
463 In such a design, light at normal incidence to the thin silicon film arrives at  $45^\circ$  with respect to  
464 the inverse woodpile structure, parallel to the  $\Gamma U$  high-symmetry direction. The stop gap for  
465 this high-symmetry direction has properties that are fairly similar to the  $\Gamma Z$  or  $\Gamma X$  stop gaps  
466 considered here [44, 45, 63, 64]. Therefore, the present analysis also pertains to this design.

467 Having a 3D silicon photonic crystal as a back reflector provides an all-silicon integration  
468 with the absorbing thin silicon film. Moreover, this approach makes the solar cell lighter, since  
469 the 3D inverse woodpile photonic crystal structure is highly porous, consisting of nearly 80%  
470 volume fraction air (see Appendix A). Simultaneously, our design remarkably enhances the  
471 overall absorption in comparison to a standalone thin silicon film with the same overall thickness,  
472 as illustrated by our results.

473 If one wishes to shift the absorption enhancements discussed here to shorter wavelengths, it  
474 is relevant to consider replacing silicon by wider band gap semiconductors such as GaAs, GaP,  
475 or GaN. In such a case, an important practical consideration is whether to realize the photonic  
476 band gap back reflector from the same semiconductor for convenient integration, or whether  
477 to perform heterogeneous integration of silicon photonic band gap crystals, since the latter are  
478 readily realizable, see Refs. [49, 65, 71, 72].

479 Since GaAs has a similar real refractive index as silicon, many of the results presented here can  
480 be exploited to make predictions for GaAs absorption in presence of a photonic band gap back  
481 reflector. For the other semiconductors, this calls for additional detailed calculations, since most  
482 semiconductors have different (complex) refractive indices than silicon, with different dispersion.  
483 Nevertheless, the computational concepts and strategies presented in our study remain relevant to  
484 address the pertinent questions.

485 As mentioned earlier, for the sake of physical understanding our computations pertain to a flat  
486 top surface of the thin silicon film without anti-reflection coating. On the other hand, it is well  
487 known that a substantial improvement in light harvesting is obtained by applying anti-reflection  
488 coatings and by tailoring the shape of top surface, for instance, a random Lambertian-like surface.  
489 Therefore, a logical research step is to combine a photonic band gap back reflector with suitable  
490 top-surface engineering, even though it is likely that this situation substantially complicates both



491 the numerical setup and the numerical convergence.

## 492 **5. Conclusion**

493 We investigated a thin 3D photonic band gap crystal as a back reflector in the visible regime,  
494 which reflects light within the band gap for all directions and for all polarizations. The absorption  
495 spectra of a thin silicon film with a 3D inverse woodpile photonic crystal back reflector were  
496 calculated using finite-element computations of the 3D time-harmonic Maxwell equations. We  
497 tailored the finite-sized inverse woodpile crystal design to have a broad photonic band gap in  
498 the visible range and have used the refractive index of the real silicon, including dispersion and  
499 absorption, in order to make our calculations relevant to experiments. From the comparison of the  
500 photonic crystal back reflector to a perfect metallic back reflector, we infer that a photonic crystal  
501 back reflector increases the number of Fabry-Pérot fringes for a thin silicon film. Therefore, we  
502 observe that a 3D inverse woodpile photonic crystal enhances the absorption of a thin silicon film  
503 by (i) behaving as a perfect reflector, exhibiting nearly 100% reflectivity in the stop bands, as well  
504 as (ii) generating guided modes at many discrete wavelengths. Our absorption results show nearly  
505  $2.39\times$  enhanced wavelength-, angle-, polarization-averaged absorption between  $\lambda = 680$  nm and  
506  $\lambda = 880$  nm compared to a 2400 nm thin silicon film. We find that the absorption enhancement  
507 is enhanced by positioning an inverse woodpile back reflector at the back end of a thin silicon  
508 film, which will keep the length of the solar cell unchanged as well as make the solar cell lighter.  
509 In order to maximize the efficiency for a given wavelength, we show that the thickness of a thin  
510 silicon film had better be chosen to the maxima of the Fabry-Pérot fringes. For a sub-wavelength  
511 ultrathin 80 nm absorbing layer with a photonic crystal back reflector, we identify and demonstrate  
512 two physical mechanisms causing the giant average absorption enhancement of  $9.15\times$ : (i) guided  
513 modes due to the Bragg attenuation length and (ii) confinement due to a surface defect.

## 514 **6. Funding**

515 This research is supported by the Shell-NWO/FOM programme "Computational Sciences for  
516 Energy Research" (CSER), NWO-FOM program nr. 138 "Stirring of light!," NWO-TTW  
517 Perspectief program P15-36 "Free-form scattering optics" (FFSO), NWO ENW-GROOT program  
518 (OCENW.GROOT.2019.071) "Self-assembled icosahedral photonic quasicrystals with a band  
519 gap for visible light", the "Descartes-Huygens" prize of the French Academy of Sciences (with  
520 support from JMG), and the MESA<sup>+</sup> Institute section Applied Nanophotonics (ANP).

## 521 **7. Acknowledgments**

522 It is a great pleasure to thank Bill Barnes (Exeter and Twente), Ad Lagendijk, Allard Mosk  
523 (Utrecht University), Oluwafemi Ojambati, Pepijn Pinkse, and Ravitej Uppu (now at University  
524 of Iowa) for stimulating discussions, Diana Grishina for logistic support, and Femius Koenderink  
525 (now at AMOLF, Amsterdam) for the analytical expression of the volume fraction in the early  
526 days, when we had just started developing silicon inverse woodpile photonic band gap crystals.

## 527 **8. Disclosures**

528 The authors declare no conflicts of interest.

## 529 **9. Data availability**

530 Data underlying the results presented in this paper are not publicly available at this time but may  
531 be obtained from the authors upon reasonable request.

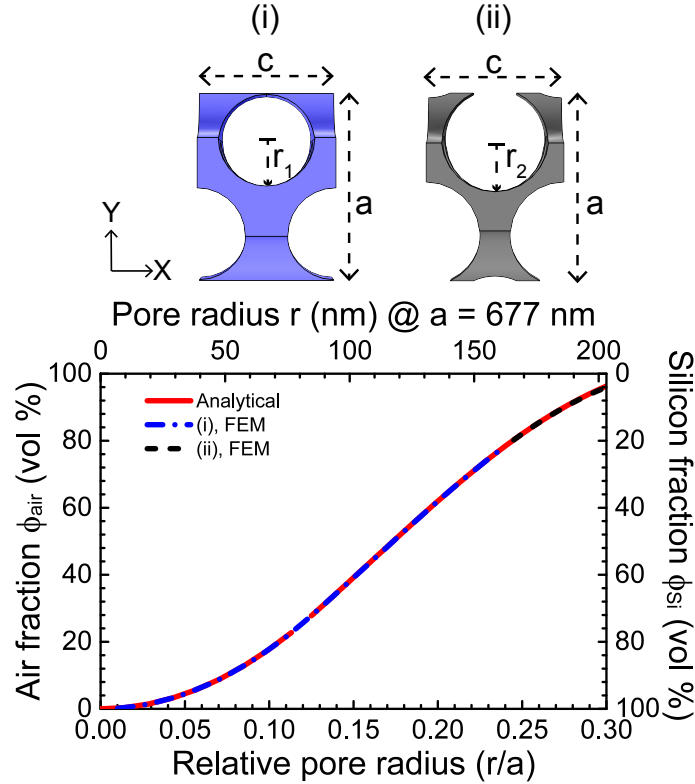


Fig. 13. Top: (i) The tetragonal primitive unit cell of the cubic inverse woodpile photonic crystal structure along the Z axis with lattice parameters  $c$  and  $a$  and the pore radius  $\frac{r_1}{a} = 0.245$ , (ii) unit cell adapted to a larger pore radius  $\frac{r_2}{a} = 0.275$ . The blue and black colors in (i) and (ii), respectively, indicate the high-index backbone of the crystal. The white color represents air. Bottom: Volume fraction of air in the 3D inverse woodpile photonic crystal versus the relative pore radius  $\frac{r}{a}$ . The blue dashed-dotted curve indicates the numerical result for a pore radius between  $\frac{r}{a} = 0$  and  $\frac{r}{a} = 0.245$  using the primitive unit cell in (i). The black dashed curve indicates the numerical result for a pore radius between  $\frac{r}{a} = 0.245$  and  $\frac{r}{a} = 0.30$  using the modified unit cell in (ii). The red solid curve represents previously unpublished analytical results by Femius Koenderink (2001).

## 532 A. Primitive unit cell of the 3D inverse woodpile photonic crystal structure

533 For a cubic inverse woodpile with lattice parameters  $c$  and  $a$ , Fig. 13 (i) shows the tetragonal  
 534 primitive unit cell for reduced nanopore radii  $\frac{r_1}{a} = 0.245$ . This unit cell is periodic in all three  
 535 directions X, Y, Z. If the air volume fraction is further increased by increasing the nanopore radii,  
 536 Fig. 13 (ii) reveals remarkable crescent-like shapes appearing at the front and the back interfaces  
 537 in the XY view of the unit cell, here for reduced pore radii  $\frac{r_1}{a} = 0.275$ . Once the pore radii  
 538 exceed  $\frac{r}{a} \geq 0.245$ , the adjacent pores intersect with each other and hence these crescent-like  
 539 shapes occur as they preserve the periodicity of the unit cell.

540 Figure 13 (bottom) shows the calculated volume fraction of air and silicon in the inverse  
 541 woodpile crystal structure versus the reduced nanopore radius  $\frac{r}{a}$  by employing a volume  
 542 integration routine of the finite element method [66]. To preserve periodicity of the numerically  
 543 approximated unit cell, we consider the primitive unit cell in (i) for a pore radius between  $\frac{r}{a} = 0$   
 544 and  $\frac{r}{a} = 0.245$  and the modified unit cell in (ii) for a pore radius between  $\frac{r}{a} = 0.245$  and  $\frac{r}{a} = 0.30$ .

545 Our numerical calculation agrees to great precision (within about  $10^{-6}\%$ ) with the analytical  
 546 results for all pore radii. Since an inverse woodpile crystal consists of nearly 80% air by volume  
 547 fraction at the optimal pore radius  $\frac{r}{a} = 0.245$ , it is a very lightweight component for photovoltaic  
 548 applications, in comparison to bulk silicon with the same thickness.

## 549 B. Brillouin zone of the 3D inverse woodpile photonic crystal structure

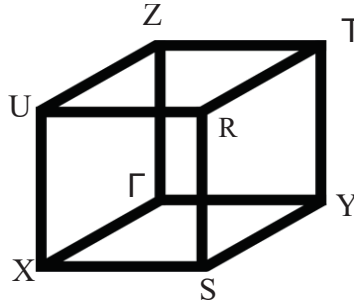


Fig. 14. First Brillouin zone of the inverse-woodpile crystal structure in the tetragonal representation showing the high-symmetry points (Roman symbols) and the origin at  $\Gamma$ .

550 Figure 14 shows the first Brillouin zone of the inverse-woodpile crystal structure in the  
 551 representation with a tetragonal unit cell, with real space lattice parameters  $(a, c, a)$ , and  
 552 reciprocal space lattice parameters  $(2\pi/a, 2\pi/c, 2\pi/a)$ . Eight high symmetry points are shown,  
 553 where  $\Gamma$  corresponds to coordinates  $(0,0,0)$ , X to  $(1/2, 0, 0)$ , Y to  $(0, 1/2, 0)$ , and Z to  $(0, 0, 1/2)$ .  
 554 The X and Z directions correspond to the directions parallel to the two sets of nanopores in the  
 555 crystal structure, that turn out to be symmetry equivalent, see Refs. [44, 45].

## 556 C. Complex and dispersive refractive index of silicon

557 To make our study relevant to practical devices, we employ the dispersive and complex refractive  
 558 index obtained from experiments to model silicon in all thin films and in the photonic crystal  
 559 backbone. Figure 15 shows the wavelength dependency of the real and imaginary parts of the  
 560 refractive index of silicon in the visible regime from several sources [61, 85, 86]. Vuye  
 561 *et al.* report the dielectric function of a commercially available silicon wafer using *in situ*  
 562 spectroscopic ellipsometry [85]. Jellison measured the dielectric function of crystalline silicon  
 563 using two-channel polarization modulation ellipsometry [86], and Green gives a tabulation of  
 564 the optical properties of intrinsic silicon based on many different sources, aiming at solar cell  
 565 calculations [61]. Figure 15 shows that for the real part of the refractive indices of Refs. [85], [86],  
 566 and [61] are in very good mutual agreement, and are thus used in our simulations. For the  
 567 imaginary part of the refractive index, we note that the results of Ref. [86] and [61] agree well  
 568 with each other between  $\lambda = 500$  nm and 750 nm and differ from the ones from Ref. [85] for  
 569 reasons unknown to us. All data sets agree well beyond  $\lambda = 750$  nm. Since Ref. [61] is based on  
 570 many different sources of data, we have chosen to adopt it as the imaginary refractive index of  
 571 silicon in our study.

572 To assess the impact of adding doped layer, a doping level of  $10^{16}$   $\text{cm}^{-3}$  already gives substantial  
 573 mobility. Fortunately, from the well-known semiconductor data collection of the Ioffe Institute  
 574 ("SVM") we find that this doping level yields a very small change in optical properties ( $\text{Re}(n_{Si})$ ,  
 575  $\text{Im}(n_{Si})$ ). Hence, the variation of intrinsic absorption versus doping level is below 1% [87], and  
 576 thus for practical purposes negligible.

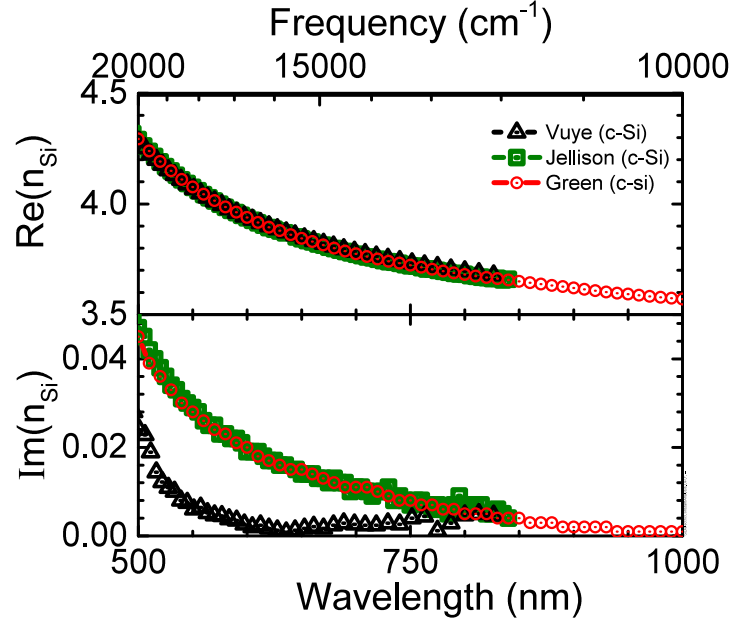


Fig. 15. Wavelength dependence of the real and imaginary parts of the refractive index of crystalline silicon (c-Si) in the visible and near infrared spectral ranges. Red circles, black triangles, and green squares are the data obtained from Ref. [61], Ref. [85], and Ref. [86], respectively. The top ordinate shows the frequency in wave numbers ( $\text{cm}^{-1}$ ).

$J_{SC}$ ( $\text{mA}/\text{cm}^2$ )	$s$ -stop band (640 nm - 890 nm)	$p$ -stop band (650 nm - 870 nm)
$L_{Si} = 80 \text{ nm Si only}$	0.2244	0.1901
$L_{Si} = 80 \text{ nm Si + perfect metal}$	0.1728	0.1544
$L_{Si} = 80 \text{ nm Si + 3D photonic crystal}$	2.9442	2.0362
$L_{Si} = 80 \text{ nm Si, Lambertian scattering}$	6.1607	5.5523

Table 1. Short circuit current density  $J_{SC}$  computed using Eq. 6 for different ultrathin silicon films: thin film only, with a perfect metal back reflector, with a 3D photonic band gap back reflector, and with Lambertian scattering.

#### 577 D. Short circuit current densities

578 In an idealized situation with perfect collection of photogenerated carriers at normal incidence,  
 579 where one absorbed photon generates one electron-hole pair, it is known that the wavelength-  
 580 dependent external quantum efficiency  $EQE(\lambda)$  is equal to the absorption  $A_{Si}(\lambda)$  [3, 74]. Hence,  
 581 the short circuit current density  $J_{SC}$  is equal to

$$J_{SC} = q \int_{\lambda-\Delta\lambda}^{\lambda+\Delta\lambda} EQE(\lambda) P_{AM1.5}(\lambda) d\lambda, \quad (6)$$

582 in other words, to the integral of the absorption spectrum weighted with the solar spectrum.

$J_{SC}$ (mA/cm <sup>2</sup> )	<i>s</i> -stop band (640 nm - 890 nm)	<i>p</i> -stop band (650 nm - 870 nm)
$L_{Si} = 2400$ nm Si only	4.1635	3.6452
$L_{Si} = 3600$ nm Si only	5.1025	4.7038
$L_{Si} = 2400$ nm + 1200 nm 3D photonic crystal	9.2394	8.9276
$L_{Si} = 2400$ nm, Lambertian scattering	16.2197	14.4055
$L_{Si} = 3600$ nm Si, Lambertian scattering	16.6290	14.7370

Table 2. Short circuit current density  $J_{SC}$  calculated using Eq. 6 at normal incidence for thin silicon films only ( $L_{Si} = 2400$  nm and  $L_{Si} = 3600$  nm), with a 3D inverse woodpile photonic crystal back reflector, and with Lambertian scattering.

583 Tables 1 and 2 show the short circuit current density  $J_{SC}$  for normal incidence (Eq. 6) for both  
584 the supra-wavelength  $L_{Si} = 2400$  nm thin and sub-wavelength  $L_{Si} = 80$  nm ultrathin silicon  
585 films, and with and without various back reflectors. Table 1 shows that the perfect metal back  
586 reflector does not increase the short circuit current density for an ultrathin film thickness much  
587 less than the wavelength in the material ( $L_{Si} \ll \lambda/n$ ). This result confirms our observation in  
588 Sec. 3.2 that a perfect metal hardly enhances absorption for films with thicknesses corresponding  
589 to a Fabry-Pérot minimum for the desired wavelengths of enhancement.

590 In presence of a 3D photonic band gap back reflector, the short circuit current density  $J_{SC}$   
591 for the  $L_{Si} = 80$  nm ultrathin film increases nearly 13× for the *s*-polarized stop band and 10×  
592 for the *p*-polarized stop band, which supports the absorption enhancements observed for 3D  
593 photonic crystal back reflector in Sec. 3.1. Moreover, similar to absorption enhancement results  
594 in Sec. 3.2 the 3D photonic band gap back reflector also increases the short circuit current density  
595 for a  $L_{Si} = 2400$  nm thin film by nearly 2.21× for *s*-stop band and 2.45× for *p*-stop band  
596 (Table 2). Finally, our computation in Table 2 supports the use of a photonic crystal back reflector  
597 by increasing the short circuit current density by 1.81× for *s*-stop band and 1.9× for *p*-stop  
598 band even compared to a  $L_{Si} = 3600$  nm thin film (similar to absorption discussion in Sec. 3.4).

599 On the other hand, both Table 1 and Table 2 show that the short circuit current density with a  
600 photonic crystal back reflector is still nearly 2 – 2.5× lower than the one computed for Lambertian  
601 scattering. This difference is attributed to the fact that absorption due to Lambertian scattering  
602 also assumes a perfect anti-reflection front coating, unlike our present computations, see Fig 2.

## 603 References

- 604 1. V. M.-Delmotte, P. Zhai, A. Pirani, S. L. Connors, C. Péan, S. Berger, N. Caud, Y. Chen, L. Goldfarb, M. I. Gomis,  
605 M. Huang, K. Leitzell, E. Lonnoy, J. B. R. Matthews, T. K. Maycock, T. Waterfield, O. Yelekçi, R. Yu, and B. Zhou,  
606 “2021: Climate Change 2021: The Physical Science Basis. Contribution of Working Group I to the Sixth Assessment  
607 Report of the Intergovernmental Panel on Climate Change ” (Cambridge University, 2021, In Press).
- 608 2. A. L. Fahrenbruch and R. H. Bube, “Fundamentals in Solar Cells” (Academic, 1983).
- 609 3. A. Luque and S. Hegedus, Editors, “Handbook of photovoltaic science and engineering” (John Wiley and Sons Ltd,  
610 2011, 2nd Edition).
- 611 4. A. Rohatgi, E. Weber, and L. C. Kimerling, “Opportunities in silicon photovoltaics and defect control in photovoltaic  
612 materials,” J. Electron. Mater. **22**, 65 (1993).
- 613 5. International Energy Agency (IEA), “Solar PV Analysis,” <https://www.iea.org/reports/solar-pv>  
614 (accessed 29 Sept. 2020).
- 615 6. “Symposium: Forty years of light management,” 2021 OSA Advanced Photonics Congress  
616 [https://www.osa.org/en-us/meetings/osa\\_meetings/advanced\\_photonics\\_congress/  
617 program/symposia/#Forty](https://www.osa.org/en-us/meetings/osa_meetings/advanced_photonics_congress/program/symposia/#Forty).

- 618 7. A. G. Aberle and P. I. Widenborg, "Crystalline Silicon Thin-Film Solar Cells via High-Temperature and Intermediate-  
619 Temperature Approaches," in Ref. [3], Chapter 11, pp. 452-486.
- 620 8. ASTM G173-03, "Standard tables for reference solar spectral irradiances: direct normal and hemispherical on 37  
621 degree tilted surface," (ASTM International, West Conshohocken, Pennsylvania, 2005).
- 622 9. C. Herzinger, B. Johs, W. McGahan, J. Woollam, and W. Paulson, "Ellipsometric determination of optical constants  
623 for silicon and thermally grown silicon dioxide via a multi-sample, multi-wavelength, multi-angle investigation," *J.*  
624 *Appl. Phys.* **83**, 3323 (1998).
- 625 10. P. Sheng, A. N. Bloch, and R. S. Stepleman, "Wavelength-selective absorption enhancement in thin-film solar cells,"  
626 *Appl. Phys. Lett.* **43**, 579 (1983).
- 627 11. T. Tiedje, E. Yablonovitch, G. D. Cody, and B. G. Brooks, "Limiting efficiency of silicon solar cells," *IEEE Trans.*  
628 *Electron Devices* **31**, 711 (1984).
- 629 12. A. Richter, M. Hermle, and S. W. Glunz, "Reassessment of the Limiting Efficiency for Crystalline Silicon Solar  
630 Cells," *IEEE Journal of Photovoltaics* **3**, 1184 (2013).
- 631 13. M. A. Green, K. Emery, Y. Hishikawa, W. Warta, and E. D. Dunlop, "Solar cell efficiency tables (Version 45)," *Prog.*  
632 *Photovolt.* **20**, 606 (2012).
- 633 14. K. Münzer, K. T. Holdermann, R. E. Schlosser, and S. Sterk, "Thin monocrystalline silicon solar cells," *IEEE Trans.*  
634 *Electron Devices* **46**, 2055 (1999).
- 635 15. A. V. Shah, H. Schade, M. Vanecek, J. Meier, E. Vallat-Sauvain, N. Wyrsh, U. Kroll, C. Droz, and J. Bailat,  
636 "Thin-film silicon solar cell technology," *Prog. Photovolt.* **12**, 113 (2004).
- 637 16. Z. Yu, A. Raman, and S. Fan, "Fundamental limit of nanophotonic light trapping in solar cells," *Proc. Natl. Acad. Sci.*  
638 *U.S.A.* **2010**, 17491 (2010).
- 639 17. N.-N. Feng, J. Michel, L. Zeng, J. Lie, C.-Y. Hong, L. C. Kimerling, and X. Duan, "Design of highly efficient  
640 light-trapping structures for thin-film crystalline silicon solar cells," *IEEE Trans. Electron Devices* **54**, 1926 (2007).
- 641 18. L. C. Andreani, A. Bozzola, P. Kowalczewski, M. Liscidini, and L. Redorici, "Silicon solar cells: toward the efficiency  
642 limits," *Adv. Phys.-X* **4**, 1548305 (2019).
- 643 19. R. Saive, "Light trapping in thin silicon solar cells: A review on fundamentals and technologies," *Prog. Photovolt.*  
644 *Res. Appl.* DOI: 10.1002/pip.3440 (2021).
- 645 20. E. Yablonovitch and G. Cody, "Intensity enhancement in textured optical sheets for solar cells," *IEEE Trans. Electron*  
646 *Devices* **29**, 300 (1982).
- 647 21. E. Moulin, U. W. Paetzold, H. Siekmann, J. Worbs, A. Bauer, and R. Carius, "Study of thin-film silicon solar cell  
648 back reflectors and potential of detached reflectors," *Energy Procedia* **10**, 106 (2011).
- 649 22. R. Brendel, M. Hirsch, R. Plüeninger, and J. Werner, "Quantum efficiency analysis of thin-layer silicon solar cells with  
650 back surface fields and optical confinement," *IEEE Trans. Electron Devices* **43**, 1104 (1996).
- 651 23. Y. Fink, J. N. Winn, S. Fan, C. Chen, J. Michel, J. D. Joannopoulos, and E. L. Thomas, "A dielectric omnidirectional  
652 reflector," *Science* **282**, 1679-1682 (1998).
- 653 24. D. J. Griffiths, "Introduction to electrodynamics," (Prentice Hall, 1999).
- 654 25. S. John, "Electromagnetic Absorption in a Disordered Medium near a Photon Mobility Edge," *Phys. Rev. Lett.* **53**,  
655 2169 (1984).
- 656 26. O. L. Muskens, J. G. Rivas, R. E. Algra, E. P. A. M. Bakkers, and A. Lagendijk, "Design of light scattering in  
657 nanowire materials for photovoltaic applications," *Nano Lett.* **8**, 2638 (2008).
- 658 27. W. Wang, S. Wu, K. Reinhardt, Y. Lu, and S. Chen, "Broadband light absorption enhancement in thin-film silicon  
659 solar cells," *Nano Lett.* **10**, 2012 (2010).
- 660 28. A. Polman and H. A. Atwater, "Photonic design principles for ultrahigh-efficiency photovoltaics," *Nat. Mater.* **11**,  
661 174 (2012).
- 662 29. M. Brongersma, Y. Cui, and S. Fan, "Light management for photovoltaics using high-index nanostructures," *Nat.*  
663 *Mater.* **13**, 451 (2014).
- 664 30. S. Nishimura, N. Abrams, B. A. Lewis, L. I. Halaoui, T. E. Mallouk, K. D. Benkstein, J. van de Lagemaat, and  
665 A. J. Frank, "Standing wave enhancement of red absorbance and photocurrent in dye-sensitized titanium dioxide  
666 photoelectrodes coupled to photonic crystals," *J. Am. Chem. Soc.* **125**, 6306 (2003).
- 667 31. A. Mihi and H. Miguez, "Origin of light-harvesting enhancement in colloidal-photonic-crystal-based dye-sensitized  
668 solar cells," *J. Phys. Chem. B* **109**, 15968 (2005).
- 669 32. S. Colodrero, A. Mihi, L. Häggman, M. Ócana, G. Boschloo, A. Hagfeldt, and H. Miguez, "Porous one-dimensional  
670 photonic crystals improve the power-conversion efficiency of dye-sensitized solar cells," *Adv. Mater.* **21**, 764 (2009).
- 671 33. M. S. Branham, W.-C. Hsu, S. Yerci, J. Loomis, S. V. Boriskina, "15.7% efficient 10- $\mu$ -thick crystalline silicon solar  
672 cells using periodic nanostructures," *Adv. Mater.* **27**, 2182 (2015).
- 673 34. W.-C. Hsu, J. K. Tong, M. S. Branham, Y. Huang, S. Yerci, S. V. Boriskina, G. Chen, "Mismatched front and back  
674 gratings for optimum light trapping in ultra-thin crystalline silicon solar cells," *Opt. Commun.* **377**, 52 (2016).
- 675 35. P. Bermel, C. Luo, L. Zeng, L. C. Kimerling, and J. D. Joannopoulos, "Improving thin-film crystalline silicon solar  
676 cell efficiencies with photonic crystals," *Opt. Express* **15**, 25 (2007).
- 677 36. P. G. O'Brien, N. P. Kherani, A. Chutinan, G. A. Ozin, S. John, and S. Zukotynski, "Silicon photovoltaics using  
678 conducting photonic crystal back-reflector," *Adv. Mater.* **20**, 1577 (2008).
- 679 37. B. Curtin, R. Biswas, and V. Dalal, "Photonic crystal based back reflectors for light management and enhanced  
680 absorption in amorphous silicon solar cells," *Appl. Phys. Lett.* **95**, 231102 (2009).

- 681 38. L. Zeng, P. Bermel, B. A. Alamariu, K. A. Broderick, J. Liu, X. Duan, J. Joannopoulos, and L. C. Kimerling,  
682 "Demonstration of enhanced absorption in thin film Si solar cells with textured photonic crystal back reflector," Appl.  
683 Phys. Lett. **93**, 221105 (2008).
- 684 39. R. Biswas, J. Bhattacharya, B. Lewis, N. Chakravarty, and V. Dalal, "Enhanced nanocrystalline silicon solar cell with  
685 a photonic crystal back-reflector," Sol. Energy Mat. Sol. Cells **94**, 2337 (2010).
- 686 40. R. B. Wehrspohn and J. Üpping, "3D photonic crystals for photon management in solar cells," J. Opt. **14**, 024003  
687 (2012).
- 688 41. A. N. Sprafke, D. Schneevoigt, S. Seidel, S. L. Schweizer, and R. B. Wehrspohn, "Automated spray coating process  
689 for the fabrication of large-area artificial opals on textured substrates," Opt. Express **21**, A528-A538 (2013)
- 690 42. K. Ishizaki, M. D. Zoysa, Y. Tanaka, S.-W. Jeon, and S. Noda, "Progress in thin-film silicon solar cells based on  
691 photonic-crystal structure," J. Appl. Phys. **57**, 060101 (2018).
- 692 43. J. D. Joannopoulos, S. G. Johnson, J. N. Winn, and R. D. Meade, "Photonic crystals: Molding the flow of light,"  
693 (Princeton University, 2008).
- 694 44. D. Devashish, S. B. Hasan, J. J. W. van der Vegt, and W. L. Vos, "Reflectivity calculated for a three-dimensional  
695 silicon photonic band gap crystal with finite support," Phys. Rev. B **95**, 155141 (2017).
- 696 45. S. R. Huisman, R. V. Nair, L. A. Woldering, M. D. Leistikow, A. P. Mosk, and W. L. Vos, "Signature of a  
697 three-dimensional photonic band gap observed with silicon inverse woodpile photonic crystals," Phys. Rev. B **83**,  
698 205313 (2011).
- 699 46. M. D. Leistikow, A. P. Mosk, E. Yeganegi, S. R. Huisman, A. Lagendijk, and W. L. Vos, "Inhibited spontaneous  
700 emission of quantum dots observed in a 3D photonic band gap," Phys. Rev. Lett. **107**, 193903 (2011).
- 701 47. E. Yeganegi, A. Lagendijk, A. P. Mosk, and W. L. Vos, "Local density of optical states in the band gap of a finite  
702 one-dimensional photonic crystal," Phys. Rev. B **89**, 045123 (2014).
- 703 48. S. B. Hasan, A. P. Mosk, W. L. Vos, and A. Lagendijk, "Finite-size Scaling of the Density of States in Photonic Band  
704 Gap Crystals," Phys. Rev. Lett. **120**, 237402 (2018).
- 705 49. D. A. Grishina, C. A. M. Hartevelde, A. Pacureanu, D. Devashish, A. Lagendijk, P. Cloetens, and W. L. Vos, "X-ray  
706 Imaging of Functional Three-Dimensional Nanostructures on Massive Substrates," ACS Nano **13**, 13932 (2019).
- 707 50. M. Adhikary, R. Uppu, C. A. M. Hartevelde, D. A. Grishina, and W. L. Vos, "Experimental probe of a complete 3D  
708 photonic band gap," Opt. Express **28**, 2684 (2020).
- 709 51. T. Tajiri, S. Takahashi, C. A. M. Hartevelde, Y. Arakawa, S. Iwamoto, and W. L. Vos, "Reflectivity of three-dimensional  
710 GaAs photonic band-gap crystals of finite thickness," Phys. Rev. B **101**, 235303 (2020).
- 711 52. C. P. Mavidis, A. C. Tasolamprou, S. B. Hasan, T. Koschny, E. N. Economou, M. Kafesaki, C. M. Soukoulis, and W.  
712 L. Vos, "Local density of optical states in the three-dimensional band gap of a finite photonic crystal," Phys. Rev. B  
713 **101**, 235309 (2020).
- 714 53. J. Orton, "The story of semiconductors," (Oxford University, 2004).
- 715 54. D. A. B. Miller, "Device Requirements for Optical Interconnects to Silicon Chips," Proc. IEEE **97**, 1166 (2009).
- 716 55. G. T. Reed, G. Mashanovich, F. Y. Gardes, and D. J. Thomson, "Silicon optical modulators," Nature Photon. **4**, 518  
717 (2010).
- 718 56. P. W. Coteus, J. U. Knickerbocker, C. H. Lam, and Y. A. Vlasov, "Technologies for exascale systems," IBM J. Res.  
719 Dev. **55**, 14 (2011).
- 720 57. M. K. Smit, J. J. G. M. van der Tol, and M. T. Hill, "Moore's law in photonics," Laser Photonics Rev. **6**, 1 (2012).
- 721 58. Y. A. Vlasov, "Silicon CMOS-integrated nano-photonics for computer and data communications beyond 100G,"  
722 IEEE Commun. Mag. **50**, S67 (2012).
- 723 59. D. Devashish, O. S. Ojambati, S. B. Hasan, J. J. W. van der Vegt, and W. L. Vos, "Three-dimensional photonic band  
724 gap cavity with finite support: Enhanced energy density and optical absorption," Phys. Rev. B **99**, 075112 (2019).
- 725 60. S. A. Hack, J. J. W. van der Vegt, and W. L. Vos, "Cartesian light: Unconventional propagation of light in a  
726 three-dimensional superlattice of coupled cavities within a three-dimensional photonic band gap," Phys. Rev. B **99**,  
727 115308 (2019).
- 728 61. M. A. Green, "Self-consistent optical parameters of intrinsic silicon at 300K including temperature coefficient," Sol.  
729 Energy Mat. Sol. Cells **92**, 1305 (2008).
- 730 62. K. M. Ho, C. T. Chan, C. M. Soukoulis, R. Biswas, and M. Sigalas, "Photonic band gaps in three dimensions: new  
731 layer-by-layer periodic structures," Solid State Commun. **89**, 413 (1994).
- 732 63. R. Hillebrand, S. Senz, W. Hergert, and U. Gösele, "Macroporous-silicon-based three-dimensional photonic crystal  
733 with a large complete band gap," J. Appl. Phys. **94**, 2758 (2003).
- 734 64. L. A. Woldering, A. P. Mosk, R. W. Tjerkstra, and W. L. Vos, "The influence of fabrication deviations on the photonic  
735 band gap of three-dimensional inverse woodpile nanostructures," J. Appl. Phys. **105**, 093108 (2009).
- 736 65. J. M. van den Broek, L. A. Woldering, R. W. Tjerkstra, F. B. Segerink, I. D. Setija, and W. L. Vos, "Inverse-woodpile  
737 photonic band gap crystals with a cubic diamond-like structure made from single-crystalline silicon," Adv. Funct.  
738 Mater. **22**, 25 (2012).
- 739 66. "COMSOL Multiphysics® v. 5.2. www.comsol.com, COMSOL AB, Stockholm, Sweden".
- 740 67. J.M. Jin, "The finite element method in electromagnetics" (Wiley-IEEE, 2000).
- 741 68. Since the air layer and the thin silicon film are homogeneous media, an upper limit  $\Delta l \leq \frac{\lambda_0}{8}$  is imposed on the edge  
742 length  $\Delta l$  of any tetrahedron in these layers, with  $\lambda_0$  the shortest wavelength of the incident plane waves in vacuum.  
743 Since an inverse woodpile crystal contains many sharp and curved interfaces between the high-index backbone and

- 744 the low-index medium, an upper limit  $\Delta l \leq \frac{\lambda_0}{8 \cdot \max(n_{Si})}$  is imposed on the edge length  $\Delta l$  of any tetrahedron inside  
745 the photonic crystal (as well as a sub-wavelength thin silicon film  $L_{Si} = 80$  nm), where  $\max(n_{Si})$  is the maximum  
746 silicon refractive index in the relevant spectral range.
- 747 69. "Serendipity" is a high performance computing cluster whose main features are 16 Dell Power edge R430 servers  
748 with each 2x Intel Xeon E5-2698 processors at 2.2GHz, with in total 640 cores and about 3.6 terabyte memory,  
749 connected through Infiniband. The head node is a Dell Power Edge R730.
- 750 70. R. Uppu, M. Adhikary, C. A. M. Hartevelde, and W. L. Vos, "Spatially shaping waves to penetrate deep inside a  
751 forbidden gap," *Phys. Rev. Lett.* **126**, 177402 (2021).
- 752 71. R. W. Tjerkstra, L. A. Woldering, J. M. van den Broek, F. Roozeboom, I. D. Setija, and W. L. Vos, "Method to pattern  
753 etch masks in two inclined planes for three-dimensional nano- and microfabrication," *J. Vac. Sci. Technol. B* **29**,  
754 061604 (2011).
- 755 72. D. A. Grishina, C. A. M. Hartevelde, L. A. Woldering, and W. L. Vos, "Method for making a single-step etch mask for  
756 3D monolithic nanostructures," *Nanotechnology* **26**, 505302 (2015).
- 757 73. E. Yablonovitch, "Statistical ray optics," *J. Opt. Soc. Am.* **72**, 899 (1982).
- 758 74. I. Massiot, A. Cattoni, and S. Collin, "Progress and prospects for ultrathin solar cells," *Nat. Energy* **5**, 959 (2020).
- 759 75. W. L. Vos and L. A. Woldering, Edited by M. Ghulinyan and L. Pavesi, "*Light Localisation and Lasing: Random  
760 and Pseudorandom Photonic Structures*" (Cambridge University, 2015), Chap. 8, pp. 180-214, also available from  
761 <http://arxiv.org/abs/1504.06803>.
- 762 76. W. L. Vos, H. M. van Driel, M. Megens, A. F. Koenderink, and A. Imhof, "Experimental probes of the optical  
763 properties of photonic crystals," in *Proceedings of the NATO ASI Photonic Crystals and Light Localization in the  
764 21st Century*, edited by C. M. Soukoulis (Kluwer, Dordrecht, 2001), pp. 181-198.
- 765 77. W. L. Vos, R. Sprik, A. van Blaaderen, A. Imhof, A. Lagendijk, and G. H. Wegdam, "Strong effects of photonic band  
766 structures on the diffraction of colloidal crystals," *Phys. Rev. B* **53**, 24 (1996).
- 767 78. S. Fan and J. D. Joannopoulos, "Analysis of guided resonances in photonic crystal slab," *Phys. Rev. B.* **65**, 235112  
768 (2002).
- 769 79. P. Berini, "Long-range surface plasmon polaritons," *Adv. Opt. Photon.* **1**, 484 (2009).
- 770 80. There is an important difference with a LRSPP, namely that here the field is maximal at the center of the thin silicon  
771 film, whereas LRSPP fields are minimal at the center of a thin metal film.
- 772 81. K. Ishizaki and S. Noda, "Manipulation of photons at the surface of three-dimensional photonic crystals," *Nature*  
773 (London) **46**, 367 (2009).
- 774 82. A. Yariv and P. Yeh, "*Optical waves in crystals: propagation and control of laser radiation*" (Wiley, 1980), Chapter  
775 6, pp. 155-219.
- 776 83. Z. Yu and S. Fan, "Angular constraint on light-trapping absorption enhancement in solar cells," *Appl. Phys. Lett.* **98**,  
777 011106 (2011).
- 778 84. S. Takahashi, M. Okano, M. Imada, s. Noda, "Three-dimensional photonic crystals based on double-angled etching  
779 and wafer-fusion techniques" *Appl. Phys. Lett.* **89**, 123106 (2006).
- 780 85. G. Vuye, S. Fisson, V. Nguyen Van, Y. Wang, J. Rivory, and F. Abelés, "Temperature dependence of the dielectric  
781 function of silicon using *in situ* spectroscopic ellipsometry," *Thin Solid Films* **233**, 166 (1993).
- 782 86. G. E. Jellison Jr., "Optical functions of silicon determined by two-channel polarization modulation ellipsometry,"  
783 *Opt. Mater.* **1**, 41 (1992).
- 784 87. A. A. Wolfson, and V. K. Subashiev, "Intrinsic absorption edge at different doping levels," *Fiz. Tekh. Poluprovodn.* **1**  
785 397 (1967) (in Russian).